UNIVERSITA' DEGLI STUDI DI MILANO &
UNIVERSITA' CATTOLICA DEL SACRO CUORE

Dipartimento di Matematica e Fisica

Corso di Dottorato di Ricerca in Fisica, Astrofisica e Fisica Applicata

Ciclo XXVIII

NON-EQUILIBRIUM STUDY OF CORRELATED HONEYCOMB IRIDATES WITH STRONG SPIN-ORBIT COUPLING.

Settore Scientifico Disciplinare FIS/03

Tesi di Dottorato di:

Nicola Nembrini

Supervisore:

Professor Claudio GIANNETTI

Coordinatore:

Professor Marco BERSANELLI

Anno Accademico 2014/2015

NON-EQUILIBRIUM STUDY OF CORRELATED HONEYCOMB IRIDATES WITH STRONG SPIN-ORBIT COUPLING.

PhD. Thesis - Physics, Astrophysics and Applied Physics PhD School - Milano

Printing, February 2016, Milano, Italy

Contents

List of Figures

List of Tables

Dedicated to my parents

Introduction

Transition-metal oxides are one of the most studied class of materials, as a consequence of their rich and exotic physical properties, mainly determined by the strong electronic correlations of the metal d electrons.

The strong Coulomb repulsion U between two electrons occupying the same metal orbitals [Mott, 1990] is responsible for several phenomena such as correlated metallic states, unconventional superconductivity, local moment formation and magnetism [Imada et al., 1998]. Descending the periodic table of elements from $3d$ to $4d$ and $5d$ series, the d orbitals become more extended tending to reduce the electronic repulsion U and thus quenching the correlation effects. On the other hand, a new interaction gets progressively more relevant: the spin-orbit coupling. The spin-orbit coupling (SOC) is an relativistic effect that links the orbital and spin angular momenta of an electron and it is usually considered a small perturbation in the discussion of the electronic properties in solids. However, the strength of SOC increases proportionally to Z^4 (Z is the atomic number)up to the point of having important effects in atoms with high atomic numbers [Hasan and Kane, 2010], [Qi and Zhang, 2011]. Therefore in such materials there are several competing energy scales to consider: the atomic on-site Hubbard interaction U, Hund's coupling J_H, the SOC interaction λ, the crystal field and the electron kinetic energy related to the hopping integral t.

A schematic "phase diagram" in terms of the relative strength of the interaction U/t and the $\lambda\ /t$ [Pesin and Balents, 2010] is reported 1. In this diagram the weak and strong correlation regions and the weak and strong SOC regimes are compared. Conventional transition metal materials reside on the left hand side of the diagram, where SOC is weak, and a conventional metal-insulator transition may occur when U is comparable to the bandwidth. Upon increasing SOC, when $U/t \ll 1$, a metallic or semi-conducting state at small U may be converted to a semi-metal. When both SOC and U are strong, they tend to cooperate in generating insulating states. The narrow bands generated by SOC are more susceptible to Mott local-

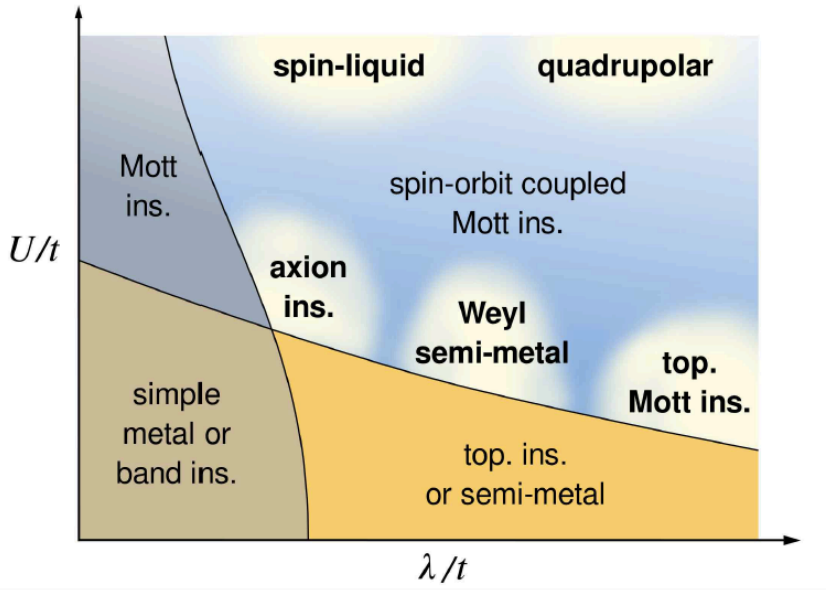

Figure 1: Schematic phase diagram for electronic material as a function of the electronic correlation U/t and the SOC λ/t, where t is the hopping amplitude. In the bottom-left corner reside simple metals or band insulators. In the top-left corner where the effect of electronic correlation dominates, lie Mott insulators. In the strong SOC regime (bottom-right corner) we find topological insulators. At the center of the phase diagram where electronic correlations and SOC cooperate, reside $5d$ TMOs like iridate [Witczak-Krempa et al., 2013].

ization by U, which implies that the horizontal boundary in figure 1 shifts downward with increasing SOC. Including correlations first, the U tends to localize electrons, diminishing their kinetic energy. Consequently the on-site SOC is relatively enhanced. There is an intermediate regime in which insulating states are obtained only from the combined influence of SOC and correlations. These may be considered spin-orbit assisted Mott insulators. A large number of materials are characterized by this interesting correlated SOC regime. The most prolific are iridates, weakly conducting or insulating oxides containing iridium, primarily in the Ir^{4+} oxidation state. These include a Ruddlesdon-Popper sequence of pseudo-cubic and planar perovskites [Kim et al., 2008] [Fujiyama et al., 2012] [King et al., 2013], hexagonal insulators $(Na/Li)_2IrO_3$ [Gretarsson et al., 2013] [Singh., 2010] [Alpichshev et al., 2015] [Comin et al., 2012], a large family of pyrochlores, $R_2Ir_2O_7$ [Yanagishima and Maeno, 2001] [Qi et al., 2012], and some spinel-related structures [Okamoto et al., 2007] [Kuriyama et al., 2010].

In this work I will focus on the family of hexagonal insulators and in particular, on Na_2IrO_3, that presents an insulating gap of $\sim$ 340 meV [Comin et al., 2012] which is already open at room temperature and does not show any significant temperature dependence. Furthermore, this system is subjected to an antiferromagnetic transition, characterized by a zig-zag pattern, at $T_N \sim 15$ K. There are two types of approaches that may be used to describe the physics of these particular systems: the quasimolecular orbitals approach with

small spin-orbit coupling and itinerant regime [Mazin et al., 2012] versus the J_{eff} picture, with large spin-orbit coupling and localized regime [Chaloupka et al., 2010], [Chaloupka et al., 2013] [Jackeli and Khaliullin, 2009]. The most relevant energy scales of the J_{eff} picture are the spin-orbit coupling λ and the Coulomb repulsion U. The Ir 5*d* t_{2g} orbitals are written in terms of relativistic orbitals ($J_{eff} = 1/2$ and $J_{eff} = 3/2$) and the combination of Kitaev-Heisemberg terms [Chaloupka et al., 2010] leads to a various magnetic ground states, including the zigzag antiferromagnetic order. On the other hand, first-principles calculations suggest considerable delocalization of electrons over individual Ir hexagons, thus allowing to build quasi-molecular orbitals (QMOs). Sodium iridates are still the subject of intense research to clarify the hierarchy of the J_{eff} and QMO pictures in determining the insulating state [Foyevtsova et al., 2013] ,[Mazin et al., 2012].

Here we tackle the physics of sodium iridates by adopting a non-equilibrium viewpoint based on the use of ultrafast light pulses combined in the so-called pump-probe experimental configuration. The aim is to perturb the antiferromagnetic state of the system via the excitation with a pump pulse and to observe the ultrafast recovery of the ground state by means of a second delayed probe pulse. Specifically, we will measure the dynamics of the pump-induced reflectivity variation in the zigzag antiferromagnetic and normal states as a function of the probe energy and as a function of time delay between the pump and the probe pulses. In this work we will start from the reflectivity variation measurements on Na_2IrO_3 performed by single-colour (1.55 eV) pump-probe experiments. As a second step, we will present broadband pump-probe measurements in the $1.4 - 2.2$ energy range, that matches with the energy region of specific QMOs. Thanks to these techniques we will be able to investigate:

- the timescale of the relaxation processes dynamics in the zigzag antiferromagnetic and in the nonmagnetic phases;
- the modification of the optical properties during the processes in the in zigzag antiferromagnetic and in the nonmagnetic phases;

The most striking observation is that when the sample is cooled down and the zigzag phase is approached, the pump induces a narrow variation of the reflectivity of the system at about 1.7 eV. This variation can be exactly reproduced by assuming a small redshift of a narrow band at about 1.7 eV. Both the amplitude of the redshift and the timescale necessary to achieve the maximum variation tend to diverge as T_N is approached. The timescale of this variation increases from about 2 ps at 50 K to 8 ps at 12 K. These results are in agreement with single-colour measurements already reported in the

literature [Alpichshev et al., 2015],[Hinton et al., 2015], where the change of dynamics observed at T_N are interpreted as a confinement-deconfinement transition, providing evidence of spin-liquid-type physics in Na_2IrO_3, and therefore the evidence of J_{eff} model. On the other hand, the broadband technique used in this work allows accessing the variation of the optical conductivity over a broad energy range. Our results evidence that the narrow reflectivity variation at 1.7 eV is compatible with the modification of a specific QMO, in agreement with ab-initio density-functional-theory calculations [Foyevtsova et al., 2013]. These results demonstrate that the validity of the J_{eff} and QMOs concepts strongly depends on the energy scale considered: while the low-energy magnetic dynamics is well described within a picture of localized moments, the QMOs becomes well defined objects at binding energies larger than ≈ 1 eV.

1 Theoretical Background

1.1 Tight-binding and the electronic properties of solids

One of the earliest ways to classify the solid states of matter was *Metal* and *Insulator*, based upon the conduction properties of electrons. The first rigorous theory was derived by Paul Drude to explain metals: the free electron theory. This theory successfully explained the electrical properties of many metals but partially failed to explain many thermodynamic properties. Sommerfeld rederived Drude theory including the Pauli exclusion principle. Metals were assumed as non interacting Fermi gases which successfully explained many thermodynamic properties of metals where Drude models failed [Ashcroft and Mermin, 2005]. As a first step, the interaction of the electrons with the lattice formed by the ions can be treated as the problem of free-electron wavefunctions interacting with a periodic potential. The solution of this problem is based on the celebrated Bloch theorem, which states that the electronic wavefunction will assume the form:

$$\Psi_k(\mathbf{r}) = u(\mathbf{r})e^{i\mathbf{k}\cdot\mathbf{r}} \tag{1.1}$$

where $u(\mathbf{r}+\mathbf{R}) = u(\mathbf{r})$ maintains the lattice symmetry upon translation of a Bravais vector $\mathbf{R}$. Therefore, the determination of the energy levels (bands) in a solid relies on the solution of an eigenvalue problem in which the appropriate interaction term between the electrons and the lattice is considered. In this framework, the equilibrium separation of the atoms in lattice are the position at which the total energy of the system is minimum. One of the simplest way from which one can approach the calculation of the energy bands in solids is the *tight-binding approximation*, or LCAO (linear combination of atomic orbitals). In order to illustrate the basic principles of LCAO, let us consider a periodic one-dimensional sequence of N equal atoms, like in figure 1.1.

In the case of negligible interaction among atoms, the same atomic orbitals centered in the different lattice sites would have the same energy; in the presence of interaction this N fold degeneracy is removed and evolves into an energy band [Kittel, 2005]. Each of these

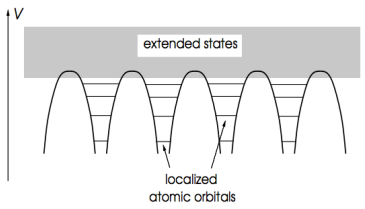

Figure 1.1: Atoms arranged in a regular lattice give rise to a periodic potential. Electron states of low energy can be considered as localized at the atom sites. The higher energy states, however, extend further and can delocalize to form itinerant electron states which form bands.

atoms contributes with a local orbital ϕ_a of energy E_a. We can use as basis set the N orbital functions $\phi_a(x - t_n)$ centered in the N atomic sites t_n to obtain the crystal wavefunctions. If we only consider the hopping between the nearest neighbour sites, we have that the diagonal matrix elements of H are all equal and the same happens with the hopping integrals between the nearest neighbour orbitals, usually indicated as t. We have:

$$E_0 = \langle \phi_a(x - x_i)|H|\phi_a(x - x_i)\rangle \tag{1.2}$$

$$t = \langle \phi_a(x - x_i)|H|\phi_a(x - x_{i\pm1})\rangle \tag{1.3}$$

In the tight-binding model, it is assumed that the ionic potentials are strong. Therefore when an electron is captured by ion during its motion through the lattice, the electron remains there for a long time before leaking to the next ion. The tight-binding (TB) model is suite to description of low-lying narrow bands for which the shell radius is much smaller than the lattice constant and so the atomic orbital is modified slightly by the other atoms in the solid. In order to calculate the energy bands and hopping integrals of 1.1, it is necessary to start from a suitable Bloch function for the problem:

$$\Psi_k(x) = \frac{1}{\sqrt{N}} \sum_{j=1}^{N} e^{ikX_j} \phi_v(x - X_j) \tag{1.4}$$

where the summation extends over all the atoms in the lattice. The function $\phi_v(x - X_j)$ is the atomic orbital centered around the j^{th} atom; it decay rapidly away from this point. The energy of the electron described by $\Psi_k(x)$ is given by

$$E(k) = \langle \Psi_k|H|\Psi_k\rangle \tag{1.5}$$

where H is the Hamiltonian of the electron using 1.4 and 1.5, we obtain:

$$E(k) = \frac{1}{N} \sum_{j,j'} e^{ikX_j} \phi_v(X_j - X_{j'}) \langle \psi_v(x - X_{j'})|H|\psi_v(x - X_j)\rangle \tag{1.6}$$

$$E(k) = \langle \psi_v(x)|H|\psi_v(x)\rangle + \sum_{j} e^{ikX_j} \langle \psi_v(x)|H|\psi_v(x - X_j)\rangle \tag{1.7}$$

The first term gives the energy of the electron would have if it were indeed entirely localized around the atom j=0, while the second includes the effects of the electron tunneling to the various other atoms. It is this term which is responsible for the band structure.

The expression for the Hamiltonian reads:

$$H = -\frac{\hbar^2}{2m} \frac{d^2}{dx^2} + V(x) \tag{1.8}$$

where $V(x)$ is the crystal potential that we can split it in to a sum of atomic potential $V_a(x)$ due to the atom at the origin and the potential due to all the other atoms $V'(x)$

$$V(s) = V_a(x) + V'(x) \tag{1.9}$$

$$\begin{aligned}\langle\psi_v(x)|H|\psi_v(x)\rangle =&\langle\psi_v(x)|[-\frac{\hbar^2}{2m}\frac{d^2}{dx^2} + V_a(x)]|\psi_v(x-X_j)\rangle \\ &+ \langle\psi_v(x)|V'(x)|\psi_v(x)\rangle\end{aligned} \tag{1.10}$$

The first term on the right is the atomic energy E_v while the second term is an integral denoted by the constant $-\beta$, that is a small quantity

$$\beta = -\int \phi_v^*(x)V'(x)\phi_v(x)dx \tag{1.11}$$

Let us now turn to the summation in 1.6. The term involving interaction with a nearest neighbour at $X_j = a$

$$\begin{aligned}\langle\psi_v(x)|H|\psi_v(x-a)\rangle =&\langle\psi_v(x)| - \frac{\hbar^2}{2m}\frac{d^2}{dx^2} + V_a(x-a)|\psi_v(x-a)\rangle \\ &+ \langle\psi_v(x)|V'(x-a)|\psi_v(x-a)\rangle\end{aligned} \tag{1.12}$$

The first term is a negligible quantity since the two functions $\phi_v(x)$ and $\phi_v(x-a)$ do not overlap. The second term is a constant which we shall call *hopping term* $-t$ that is a overlap integral

$$\gamma = -\int \phi_v^*(x)V'(x-a)\phi_v(x-a)dx \tag{1.13}$$

Substituting the result into 1.6 and restricting the sum to nearest neighbours only, one finds:

$$E(k) = E_v - \beta - 2\gamma cos(ka) \tag{1.14}$$

Equation 1.14 may be rewritten as

$$E(k) = E_0 + 4\gamma \sin^2\left(\frac{ka}{2}\right) \tag{1.15}$$

where $E_0 = E_v - \beta - 2\gamma$.

In figure 1.2 the energy $E(k)$ is plotted versus k. The original atomic level E_v has broadened into an energy band. The bottom of the band, located at $K = 0$, is equal to E_0 and its width is equal to $4t$. The bandwidth, $4t$, is proportional to the overlap integral that in TB model is supposed to be small.

In this treatment of TB model, we have seen how an atomic level *broadens* into a band as a result of the interaction between the electrons and the atoms in a periodic and perfect crystal. The states of

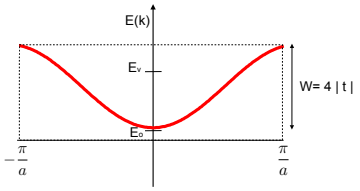

Figure 1.2: Energy band $E(k) = E_0 + 2t\cos(ka)$ for a tight-binding model with a single orbital per site and nearest neighbour interactions.

the band can be filled with electrons following the Pauli exclusion principle and up to the level determined by the total electronic density. Furthermore, the electronic properties of conventional materials can be satisfactorily explained within the "independent-electron" approximation. In this picture, the eigenstates are independent of the filling level of the bands. Each wavefunction can be treated as that of an independent electron moving in an effective "mean-field" determined by all other electrons.

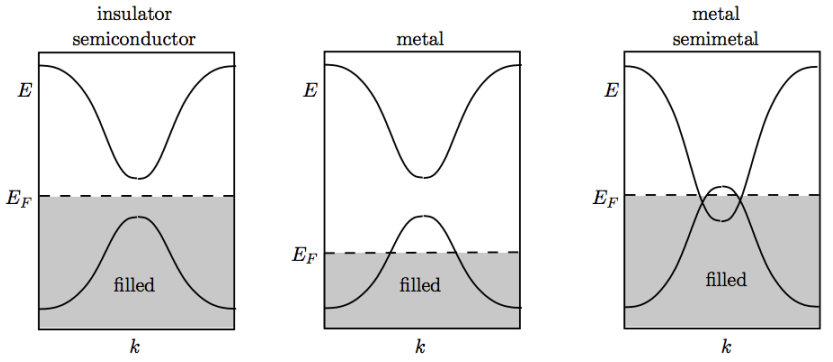

Figure 1.3: Material classes according to band filling: left panel: insulator or semiconductor (partially filled bands with the Fermi level in band gap); center panel: metal (Fermi level inside band); right panel: metal or semi-metal (Fermi level inside two overlapping bands).

As shown in figure 1.3 there are two main possible filling configurations, which give rise to dramatically different electronic properties: 1) partially-filled band; 2) completely filled band. In the following, we summarize the main configurations which can be obtained in conventional solids.

- The bands can be either completely filled or empty when the number of electrons per atom is even. Thus taking the complete set of energy bands into account, the Fermi energy lies within the energy gap separating highest filled and the lowest empty band. There is a finite energy needed to add, to remove or to excite an electron. If the band gap E_g is much smaller than the bandwidth, we call the material a *semiconductor* while for E_g of the order of the bandwidth, it is an *insulator*.

- If the number of electrons per unit cell is *odd*, the uppermost non-empty band is half filled. Then the system is a *metal*, in which electrons can move and excitations with arbitrarily small energies are possible. The electrons remain mobile down to arbitrarily low temperatures.

- In general, band structures are more complex. Different bands need not to be separated by energy gaps, but can overlap instead. In particular, this happens, when different orbitals are involved in

the structure of the bands. In these systems, bands can have any fractional filling (not just filled or half-filled). Systems, where two bands overlap at the Fermi energy but the overlap is small, are called *semi-metals*

1.2 Density Functional Theory (DFT)

As we have seen in the previous section, a crystal can be a metal semi-insulator or insulator and it exhibits a high degree of symmetry. Using this property Bravais defined classes of crystals, all differing by the symmetry of the repeating unit composing the network of atoms. Those repeating units (unit cells) are repeated uniformly in the 3-dimensional space to form the infinitely extended solid. So, it is possible to do theoretical simulations of the extended crystal lattice. The task of simulating an infinitely extended system like a crystal, often reduces to the simulation of a simple unit cell containing only a few elements.

The Density Functional Theory (DFT), proposed by Hohenberg and Kohn in 1964 [Hohenberg and Kohn, 1964], is a method used for electronic structure calculations in which the ground state energy of a electron gas in the presence of a external potential V_{ext} can be calculated exactly if its electron density n is known.

The ground state total energy E of the electron gas is given as a unique functional (function of a function) of the density:

$$E \equiv E[n(\mathbf{r})] \tag{1.16}$$

The hamiltonian $\hat{H}$ for the system of N electrons subject to an external potential is

$$\hat{H} = \hat{T} + \hat{V}_{e-e} + \sum_{i=1}^{N} V_{ext}(r_i) \tag{1.17}$$

where $\hat{T}$ is the kinetic energy operator, $\hat{V}_{e-e}$ is the electron-electron interaction operator while the external potential will be the sum of all ion-electron interactions in the solid [1]. It is then defined a functional of density F$[n]$, independent of choice of the system and external potential, such that:

[1] ion is typically taken to mean a species comprised of either a bare nucleus or a nucleus and associated core electrons.

$$F[n] = \min_{|\Psi|^2 \to n} \langle \Psi | \hat{T} + \hat{V}_{e-e} | \Psi \rangle$$

Given an external potential and a known functional $F[n]$ of the electron density, the ground state of the system is the minimum value of

$$E[n] = F[n] + \int V_{ext}(\mathbf{r}) n(\mathbf{r}) d\mathbf{r}$$

The advantage of the DFT is that one only needs the density $n(r)$, that is function of only 3 space variables, instead of the usual 3N variables associated with the many-electron wavefunction. The main important thing in DFT, is to determine the expression for the functional $F[n]$. The latter must include the kinetic energy of electrons $T_s[n]$, their classical Hartree Coulomb repulsion energy $E_H[n]$ and their exchange correlation energies $E_{xc}[n]$:

$$F[n] = T_s[n] + E_H[n] + E_{xc}[n] \tag{1.18}$$

The exact expression for the kinetic energy functional and for the exchange-correlation functional are however not known. Mainly, there are two different formulations for $E_{xc}[n]$: the Local Density Approximations (LDA) and the Generalized Gradient Approximation (GGA) [Burke and Wagner, 2013]. In the LDA formulation [Segall et al., 2002], the exchange-correlation energy per electron at a point r in space is assumed to be the exchange-correlation energy per electron in a homogeneous electron gas which has the same density as the electron gas considered at the same point in space. The LDA is clearly wrong, due to the simple fact that the electron density around an atom cannot be assumed to be homogeneous. Nevertheless the method not only has proven to be simple in formalism, but also useful and very powerful in describing many properties of many systems. Of course, the approximation shows serious breakdown when a system exhibits substantial electronic density spatial fluctuations. In the GGA approach, one tries to correct the LDA approximation by introducing a dependence on the gradient of the density, in order to take into account the possible inhomogeneity of the electron gas [Perdew et al., 1992].

1.3 *Comparison of different energy scales in TMOs*

The transition-metal oxides (TMO) are particular system that exhibit a rich variety of phenomena, such as Mott transition, high-Tc superconductivity, ferromagnetism, antiferromagnetism, low-spin/high-spin transitions, ferroelectricity, antiferroelectricity, colossal magnetoresistance [Dagotto et al., 2003], charge ordering, and bipolaron formation. The main actors in these phenomena are the d-electrons of the transition metal (TM) ions surrounded by oxygen ions. In the large majority of TMOs, the transition metal atoms are octahedrally or tetrahedrally coordinated. The presence of these oxygens lifts the fivefold degeneracy of the transition metal d-orbitals in a predictable manner, which is covered in detail in numerous texts [Tokura and Nagaosa, 2000], [Dagotto et al., 2003] and highlights that any complete description of the physics of TMOs must include hybridization

between the transition metal d-orbitals and oxygen p-orbitals. There are TMOs that are highly conductive, as in the case of ReO_3 that it can be considered as a good metal whose properties are determined from the band structure [Ishii et al., 1976]. On the other hand, there are TMOs which violate the predictions of band theory, and where fierce competition between electron localization and itinerancy dominates the physics. NiO is such an example where, having an odd number of electrons, band theory predicts a metallic state (see 1.1). In reality, NiO is an insulator, which results from on-site Coulomb repulsion (U) dominating over the ability of an electron to hop from site to site, which is directly related to the bandwidth (W). These type of materials are defined Mott-Hubbard (MH) insulators.

Furthermore there are TMOs, whose transition metals (TM) are $5d$ orbitals, that are subject to a strong spin-orbit coupling interaction, in addition to bandwidth and Coulomb repulsion. Due to their extended orbitals and large spin-orbit coupling an unusual energy hierarchy emerges, resulting in interesting electronic properties. In many cases these properties can only be understood by treating the interplay between electronic correlations, lattice structure and spin-orbit coupling on the same level.

In the next sections we discuss in detail the competing interactions to which TMOs are subjected.

1.3.1 *Crystal Field*

In the case of the free transition metal atom, the orbitals are energetically degenerate. However, the energy levels of the atom in a crystal environment will be modified by the field due to neighbouring atoms. The size and nature of the Crystal Field (CF) depends on the symmetry of the local environment that is the arrangement of the O^{2-} ions (yellow spheres in the figure 1.4) surrounding the transition metal atom (purple sphere in the figure 1.4). The most common form of the ligand geometry in d-TMOs is octahedral, where the transition metal atom is surrounded by six equidistant O^{2-} ion. The ligand O atoms have negative valence so the CF of electrons in the direction of the ligand atom is higher than in other directions due to electrostatic repulsion. Hence, under CF, $d_{3z^2-r^2}$ and $d_{x^2-y^2}$ orbitals which point towards z and x;y-axis respectively shift to higher energy by forming e_g (with orbitals strongly overlapping with the neighbouring p-orbitals of the oxygen anions) energy state and d_{xy}, d_{yz}, d_{zx} orbitals shift to lower energy by forming t_{2g} energy state (see the figure 1.4). Energy difference between the two states for typical TMOs is 2-3 eV.

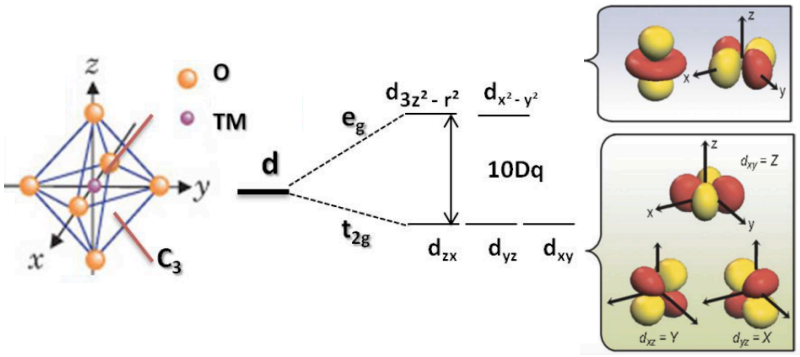

Figure 1.4: At left: undistorted octahedron and TM ion in octahedral ligand environment shown in a cubic coordinate system. C_3 is cubic 3-fold rotation axis. In center: the splitting of d-orbital by octahedral crystal field (CF). At right: the space representation of e_g and t_{2g} orbitals

1.3.2 *Hund's rule*

In the atomic shell model the possible states for an electron are determined by a set of quantum numbers n, l, m_l, m_s, which are known as principle, orbital, orbital magnetic and spin magnetic quantum number respectively. The Pauli exclusion principle states that each quantum state can be occupied by one electron. The good quantum numbers are the total orbital and total spin angular momentum for given subshell l:

$$L = \sum m_l \tag{1.19}$$

$$S = \sum m_s \tag{1.20}$$

In a typical atom, which has more than one electron, most of these fill up the lower-energy shells, producing both L and S equal to zero. However, there may be partially unfilled higher-energy shells. Thus the total electronic angular momentum of the atom $J = L + S$ will be determined by those outermost shells producing one of $(2L + 1)(2S + 1)$ possible values. These different combinations will cost different amounts of energy, because the choice of spin angular momentum affects the spatial part of the electron wave function, and the orbital momentum affects how the electron travels around the nucleus. The optimal value should allow the electrons to well avoid each other thus minimizing the Coulomb repulsion energy.

- The states are occupied to maximize S, i.e.the electrons tend to have theirs spins aligned. Electrons with parallel spins avoid each other which reduces the Coulomb repulsion. Hence the ground state of an incomplete shell in a free atom is that of a maximum spin.
- The states are occupied to maximize the value of L, which means the subshells with maximum $|l|$ are preferential.

- The total angular momentum J is obtained by combining L and S depending on the level the shell is filled:
  - less than half filled subshell, $J = |L - S|$
  - more than half full subshell, $J = |L + S|$
  - L = 0 and J = S if the subshell is exactly half-full

Hund's coupling energy is basically the energy difference between high spin state and low spin state energy saved by putting all the spins in different m_l states in parallel.

1.3.3 *Spin-orbin coupling*

Another important interaction in the TMOs is that between an electron's spin magnetic dipole moment and the internal magnetic field. It is called spin-orbit coupling (SOC). SOC is a relativistic effect, which provides an interaction between the orbital angular momentum (L) and electron spin in atoms. Usually it is considered a small perturbation in the calculation of the band structure of solids. However, in heavy elements it can significantly increase, since it scales as Z^4.

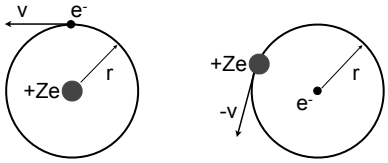

Figure 1.5: Left: An electron moves in a circular orbit, the motion as seen by the nucleus. Right: The same motion, but as seen by the electron.

In the electron's instantaneous rest frame the nucleus with a charge Ze orbiting around it (see figure 1.5) creates a magnetic field of a magnitude

$$B = \frac{\mu_0 I}{2r} \tag{1.21}$$

where $I = Ze/T$ is effective current from the charge orbiting with a period T in a hydrogen-like atom. The orbital angular momentum of the electron is $L = rmv = 2\pi mr^2/T$ (in the nucleus rest frame) and points in the same direction as B. So, using $c = 1/\sqrt{\epsilon_0 \mu_0}$ the expression 1.21 becomes

$$\mathbf{B} = \frac{1}{4\pi\epsilon_0}\frac{Ze}{mc^2 r^3}\mathbf{L} \tag{1.22}$$

Using the magnetic moment of the electron $\mathbf{m} = -(e/m)\mathbf{S}$ and the expression for magnetic field, one obtains the expression for spin-orbit interaction

$$\hat{H}_{SO} = \left(\frac{Ze^2}{8\pi\epsilon_0}\right)\frac{1}{m^2c^2r^3}\mathbf{S}\cdot\mathbf{L} \tag{1.23}$$

that simplify it

$$\hat{H}_{SO} = \lambda \mathbf{S}\cdot\mathbf{L} \tag{1.24}$$

The value of spin-orbit interaction λ is proportional to Z^4_{eff} (the effective atomic number), so it plays a fundamental role in the properties of transition metal oxides. For example, the case for the $3d$ TM

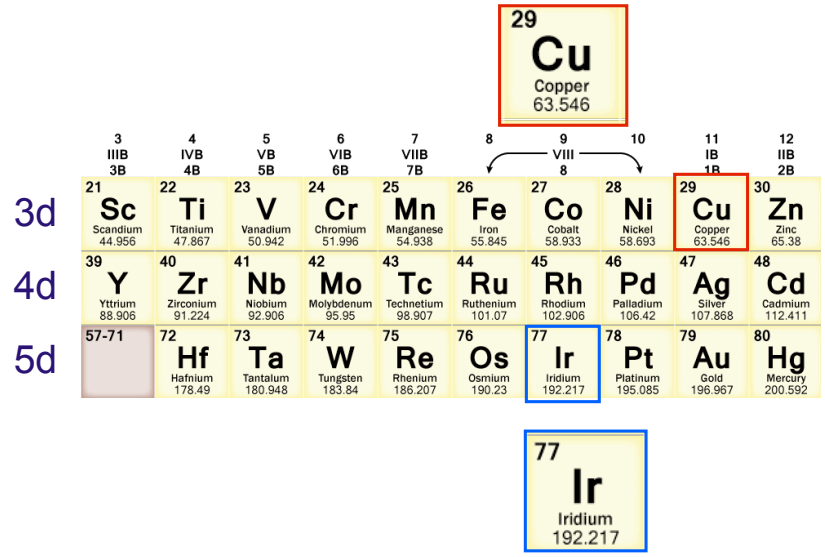

Figure 1.6: Comparison between the atomic weight of $3d$ TM atom and $5d$ TM atom.

elements such as Cu which has atomic number Z=29 and $\lambda \sim 0.01$ eV, while the iridium has Z =77 and $\lambda \sim 0.5$ eV [Andlauer et al., 1976], [Blazey and Levy, 1986]. Therefore For $5d$ elements λ becomes an important energy scale, having value 0.4-0.5 eV, whereas it is only 0.05 eV for $3d$ elements. Moreover, it is found that in Iridium λ is higher than its neighbours (e.g. Rhenium) in the same period [Clancy et al., 2012].

1.3.4 *Coulomb interaction*

Two electrons in the same orbital will face some Coulomb repulsion which will restrict the hopping of electrons to the next site. This interaction localizes the electron in a single site and turns some partially filled valence band metal into insulator, restricting electron hopping. The Hubbard model is the first model which explains the electron motion in a lattice considering electron correlation [Hubbard, 1964] and is believed to capture the main part of the physics of the strongly correlated materials. To give a better way to compare the tight-binding model with the Hubbard model it is useful to rewrite the tight-binding wave function of one electron bounded to site i in a second quantization 3D picture

$$\phi_a(\mathbf{r} - \mathbf{R}_i)\chi(\sigma) = c^\dagger_{j\sigma}|0\rangle \tag{1.25}$$

where $\chi(\sigma)$ is the the spinor function, $c^\dagger_{j\sigma}$ is the creation operator that creates one electron with spin σ on the site i. At this point the tight-binding hamiltonian can be rewrite in the following way:

$$H = -t \sum_{<j,i,\sigma>\sigma} c^{\dagger}_{i\sigma} c_{j\sigma} \qquad t_{ii} = 0 \qquad t_{ij} = t_{ji}$$

The hopping hamiltonian is the sum over all hopping processes: $c_{i\sigma}$ destroys an electron on lattice site j and $c^{\dagger}_{i\sigma}$ creates the electron on site i. By introducing the electron-electron interaction, the most important interaction is between two electrons on the same site that have experience of a strong Coulomb repulsions between each other. Because of the Pauli exclusion principle there can maximally be only two electrons per site with opposite spins. The correlation energy between two electrons on the same site is given by:

$$U = \int dr_1 dr_2 |\phi_a(r_1)|^2 \frac{e^2}{|r_1 - r_2|} |\phi_a(\mathbf{r}_2)|^2 \tag{1.26}$$

and this energy can emerges only when a single site is doubly occupied. So we can define the interaction hamiltonian as the sum over all the doubly occupied sites:

$$H_U = U \sum_i \hat{n}_{i\uparrow} \hat{n}_{i\downarrow} \tag{1.27}$$

where $n_{i\sigma}$=$c^{\dagger}_{i\sigma}$ $c_{i\sigma}$ is the electron number operator for spin σ on the site i. $n_{i\sigma}$ can assume just the values 0 or 1.

The one band Hubbard hamiltonian is the sum of the two terms:

$$H = -t \sum_{<j,i>\sigma} (c^{\dagger}_{i\sigma} c_{j\sigma} + c^{\dagger}_{i\sigma} c_{j\sigma}) + U \sum_i \hat{n}_{i\uparrow} \hat{n}_{i\downarrow} \tag{1.28}$$

Now if both U and t have finite value, in the U < t limit free electron hopping will prefer a metallic state but in the U > t limit electrons will be forced to localize in a single site and electric charge can not flow through lattice hence it will give rise to a insulating state. This is the first model to explain an insulating state of a material where tight-binding model failed.

1.4 Conclusion

In the TMOs, TM ion contributes either 3d or 4d or 5d orbital. The Hubbard model well describes those elements characterized by localized outer orbitals as 3d and 4d because their energy bands are narrow ($\sim$ 3 eV) in comparison with the strong Coulomb repulsion between electrons which is of the order of $\sim 8 - 10$ eV [Antonides et al., 1977]. If we go down in the periodic table in figure 1.8, H_{SO} can not be treated as perturbation.

For 5d elements λ becomes an important energy scale, having value $0.4 - 0.5$ eV, whereas it is only 0.05 eV for 3d elements. Hund's

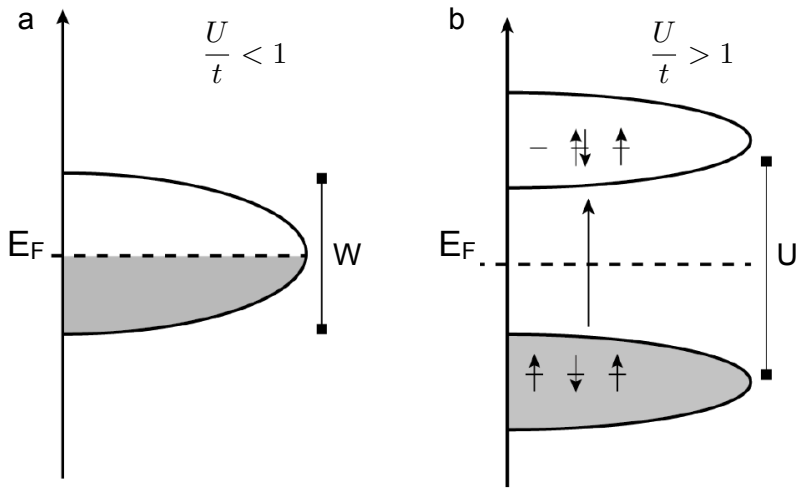

Figure 1.7: In the half-filling case, when the electronic correlations are weak (**a**) the system is a metal with half-filled band. When the correlations are strong (**b**) an energy gap U is present due to the energy cost in creating a doubled occupation.

coupling J_H has much higher value in $3d$ compared to $5d$ and it decreases with the increase of bandwidth. In $3d$ materials like manganites it plays a crucial role to achieve high spin state, it is order of crystal field splitting of e_g and t_{2g}.[Salamon, 2001], [Tokura, 1999].

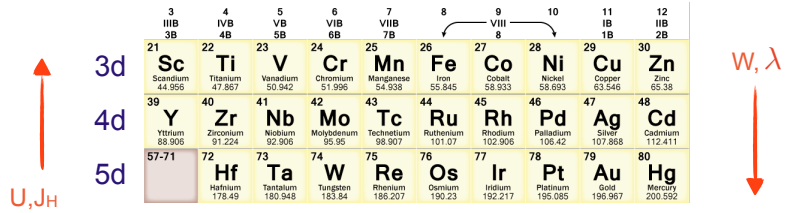

Figure 1.8: Variation of different energy scales Bandwidth (W), Coulomb repulsion (U), Hund's coupling (J_H), Spin-orbit coupling (λ) along $3d$ to $5d$ in the periodic table.

In conclusion, we have seen that the interplay between these three energy scales W,U, and SO and the strength of one on the others needs a variety of different models to well describe the several experimental evidences. The following table can help to summarize the concepts:

Relative Energies	**Elements**	**Theory**	**Absolute Energies**
$SO, U \ll W$	Delocalized orbitals s and p	Band Theory	$W \sim 0.35$ eV
$SO, W \ll U$	Localized $3d$ orbitals	Hubbard Model	$U \sim 8 - 10$ eV
$SO \simeq W \simeq U$	$4d$ and $5d$ orbitals	J_{eff} model	$SO \sim 0.4$ eV

2 Physical properties of Na_2IrO_3

In this chapter we describe the physical properties and underlying physics of the honeycomb lattice iridate Na_2IrO_3. After analysing the crystal structure of Na_2IrO_3, we present the transport, magnetic, and thermal properties of this system, performed by [Singh., 2010] and [Liu et al., 2011]. These studies show the insulating behaviour of Na_2IrO_3, with a gap of 340 meV, [Comin et al., 2012] and a antiferromagnetic phase transition when the system is cooled down to temperature of T_N=15K. These features indicate that bulk Na_2IrO_3 is a Mott insulator.

Finally, we discuss the electronic structure of the system in two descriptions: the strong spin-orbit coupling limit, in which Ir atoms can be described as localized magnetic moment through the J_{eff} model , and small spin-orbit coupling limit in which the electron present a itinerant behaviour and it is localized in quasi-molecular orbital structures (QMO).

2.1 Crystal structure of Na_2IrO_3

The basic structure of Na_2IrO_3 is shown in figure 2.1. As we can see in the panel **a**, the single crystal of Na_2IrO_3 is made up of layers containing only Na atoms (yellow spheres) alternating $NaIr_2O_6$ layers stacked along the c axis.

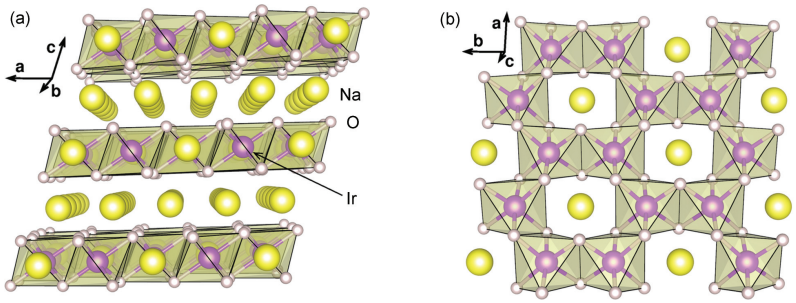

Figure 2.1: The crystallographic structure of Na_2IrO_3. The Na, Ir and O atoms are shown as yellow, purple, and grey spheres, respectively. Panel **a**: the view perpendicular to the c axis showing the layered structure with layers containing only Na atoms alternating slabs of $NaIr_2O_6$ stacked along the c axis. The IrO_6 octahedra are shown in pink with the purple Ir atoms sitting in the middle. Panel **b**: one of the $NaIr_2O_6$ slabs viewed down the c axis to highlight the honeycomb lattice of Ir atoms within the layer. The Na atoms occupy voids between the IrO_6 octahedra.

Within the $NaIr_2O_6$ layers the edge sharing IrO_6 octahedra from

honeycomb lattice and each octahedra are connencted with the three other neighbouring octahedra. From the panel **b** of the figure 2.1 we can observe the hexagonal structure made of six Ir-atoms (purple spheres). This crystal structure is obtained by a powder x-ray diffraction scans of single crystals by [Singh., 2010]. An idealized crystal structure of this kind corresponds to having all nearest neighbour Ir-Ir and Ir-O distances equal and Ir-O-Ir angles of 90° . The experimental structure of Na_2IrO_3 shows a few distortions compared to the experimental structure:

- orthorhombic distortion that introduces inequality among NN Ir-Ir distances and among NN Ir-O distances;
- IrO_6 octahedra rotations that place O atoms on the faces of a cube containing an Ir hexagon;
- trigonal distortion which is a compression of the IrO_6 octahedra in the *c*-direction that induces a departure from 90 degrees of the Ir-O-Ir angles (see figure 2.2);

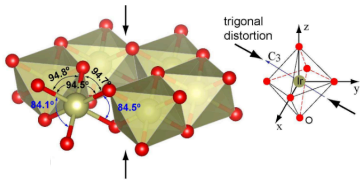

Figure 2.2: The compression of IrO_6 octahedron along the stacking leads to the decrease of O-Ir-O bond angles across the shared edges.Measurement was done by Ye et. al [Ye et al., 2012]

Na_2IrO_3 single crystals were grown by self-flux method [Singh., 2010] and preoriented by Laue diffraction, and then cleaved *in situ* at a base pressure of 5×10^{-11} mbar, exposing the (001) surface.

2.2 *Electrical resistivity*

In this section we present the transport studies performed on Na_2IrO_3 by Singh et. al [Singh., 2010].

In figure 2.3 the in-plane resistivity ρ(T) measured on Na_2IrO_3 single crystal, between T=80 and 350 K, is reported. The value $\rho(350K) \sim 21\Omega$ cm and the temperature dependence indicate that Na_2IrO_3 is an insulator. The resistivity data as a function of $(T)^{-1}$ on logarithmic plot and the resistivity data as a function of $(T)^{-1/4}$ on logarithmic plot are reported in panel **a** and in panel **b** of the figure 2.3, respectively. The experimental data follow a $\rho(T) \propto exp[(\Delta/T)^{1/4}]$ behaviour between 100 and 300 K with deviation at higher and lower T [Singh., 2010] and similar temperature dependence was observed for other systems [Cao et al., 1998].

In the section 2.1 we have seen that the crystal structure of Na_2IrO_3 is very layered structure, stacked along c-axis 2.1. But because of the monoclinic geometry of the system, there is an anisotropy in the resistivity. In fact measured the resistivity in two configuration of the Na_2IrO_3 plate: the resistivity of along the *ab* plane (R_{ab}) and the resistivity along *c*-axis (R_c) (see figure 2.4).

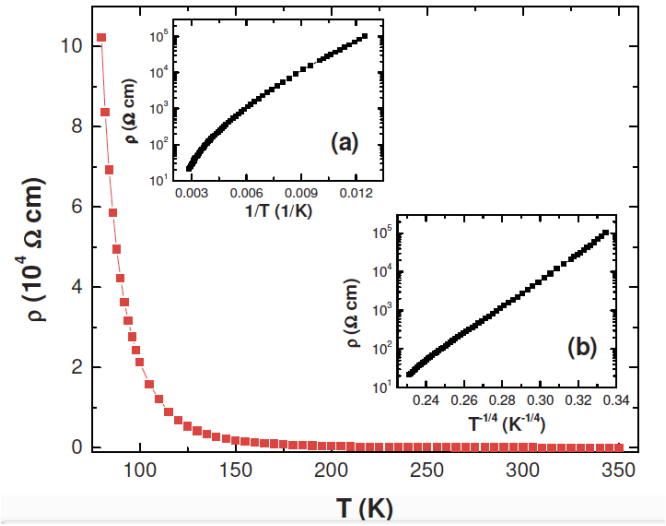

Figure 2.3: The in-plane electrical resistivity ρ versus temperatures T for a single crystal of Na_2IrO_3. The inset **a** shows the ρ versus $1/T$ data on a semi-log scale. The inset **b** shows the ρ versus $1/T^{1/4}$ data on a semi-log scale. Measurement was done by Singh et. al[Singh., 2010]

We can observe that the value of R(T)/R(350K) along c-axis is 3 order of magnitude higher than along ab-plane at 75 K.

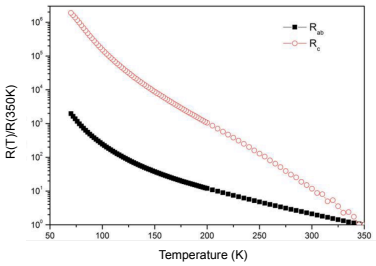

Figure 2.4: Normalized resistivity R_{ab} and R_c measured for Na_2IrO_3.Measurement was done by Singh et. al[Singh., 2010]

2.3 *Magnetic susceptibility*

Another study performed on Na_2IrO_3 by Singh et. al concerns the magnetic susceptibility (χ), i.e. how the system responding to a magnetic field.

In panel **a** of the figure 2.5, the inverse magnetic susceptibility $1/\chi = H/M$ as a function of temperature in applied magnetic field $H = 2$ T for a collection of single crystals of Na_2IrO_3 is reported [Singh., 2010]. High temperture susceptibility follows Curie-

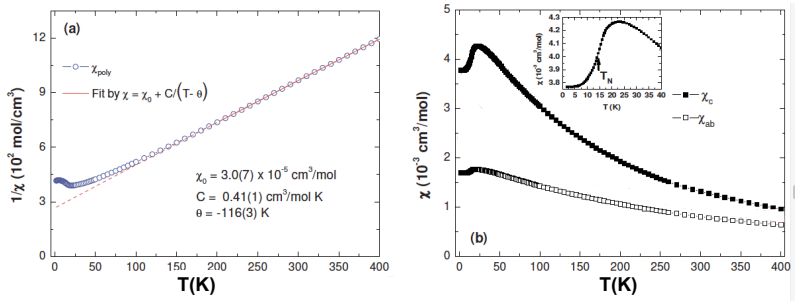

Figure 2.5: Panel **a**: Inverse magnetic susceptibility $1/\chi$ =H/M versus temperature T for a collection of randomly oriented single crystals of Na_2IrO_3 in a magnetic field H=2T. The solid curve through the data is a fit by the expression $\chi = \chi_0 + C/(T-\theta)$ and the dashed curve is an extrapolation to T=0. Panel **b**: the anisotropic magnetic susceptibilities χ_c and χ_{ab} versus T. The inset shows the χ_c (T) data at low T to highlight the broad maximum at T=23 K. The arrow indicates the onset temperature T_N=15 K for the long-ranged antiferromagnetic ordering. Measurement was done by Singh et. al[Singh., 2010]

Weiss (CW) behaviour:

$$\chi = \chi_0 + \frac{C}{T - \theta_W} \tag{2.1}$$

where C is a material-specific Curie constant and θ_W is the Curie temperature. The data in panel **a** of the figure 2.5 are fit by the formula 2.1 with χ_0, C and θ_W as fitting parameters [Singh., 2010]. By inspection of the fitting results, Singh et.al show that the Ir^{4+} moments are in an effective spin S_{eff}=1/2 state and the high negative θ_W =−116 K implies that the underlying interactions are strongly frustrated .

It was also noted that, as in the case of the resistivity, there is an anisotropy in the magnetization measurements. The anisotropic magnetic susceptibilities are shown in the panel **b** of the figure 2.5. χ_c and χ_{ab} are the magnetic susceptibilities measured with H=2 T applied along the c-axis and perpendicular to the c-axis, respectively. The data deviate from the CW behaviour below about T=100 K and pass over a broad maximum at about 23 K before dropping abruptly below T$\sim$ 15 K. The sharp drop below T_N is associated with the onset of long-ranged antiferromagnetic ordering in Na_2IrO_3 while the broad maximum above the ordering is most likely associated with short ranged order seen commonly in low-dimensional magnetic materials .

2.4 *Heat capacity of Na_2IrO_3*

Heat capacity is a useful thermodynamic tool to detect any structural and magnetic phase transition. An object's heat capacity C is defined as the ratio of the amount of heat energy transferred to an object and the resulting increase in temperature of the object,

$$C \equiv \frac{Q}{\Delta T}, \tag{2.2}$$

assuming that the temperature range is sufficiently small so that the heat capacity is constant. More generally, because heat capacity does depend upon temperature, it should be written as

$$C(T) \equiv \frac{\delta Q}{dT}, \tag{2.3}$$

The heat capacity for a solid system has three part :

- lattice heat capacity ($C_{lat} \propto T^3$);
- electronic heat capacity ($C_{el} \propto T$);
- magnetic heat capacity ($C_m \propto T^{\alpha}$)

In the panel **a** of the figure 2.6, the heat capacity divided by temperature C/T versus temperature T data for single crystals of Na_2IrO_3 in a zero magnetic filed H is reported.

The anomaly at T_N=15 K for Na_2IrO_3 confirms the bulk nature of the antiferromagnetic ordering observed in the χ data in 2.5. The

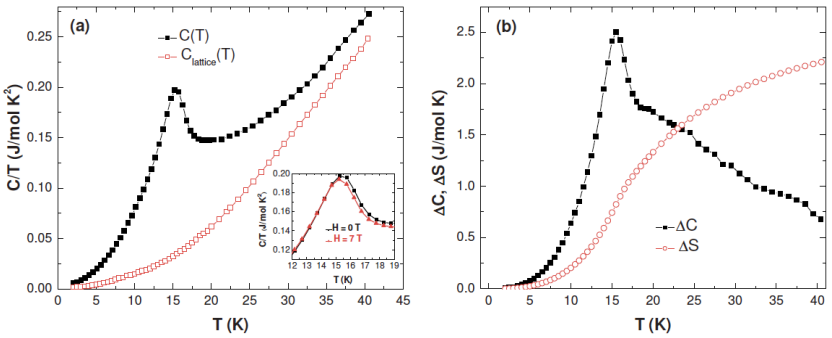

Figure 2.6: Panel **a**: The heat capacity divided by temperature C/T versus T data between T=1.8 K and 40 K for single crystals of Na_2IrO_3 and the lattice contribution $C_{lattice}$/T versus T. The inset shows the C/T versus T data in H=0 and 7 T applied magnetic field. Panel **b**: The difference heat capacity ΔC and difference entropy ΔS versus T data between T=1.8 and 40 K. Measurement was done by Singh et. al [Singh., 2010]

inset panel **a** of the figure 2.6 shows the C/T versus T data between T=12 and 19 K, measured in H=0 and H=7 T. The slight depression of T_N in an applied magnetic field indicates the antiferromagnetic nature of the ordering.

The magnetic heat capacity ($\Delta C(T)$) is obtained subtracting lattice heat capacity (C_{lat}) from the sample heat capacity (C), since that for an insulator C_{el} is zero. The panel **b** in figure 2.6 shows the $\Delta C(T)$ and the difference entropy $\Delta S(T)$ obtained by integrating the $\Delta C(T)$ /T versus T data. It indicates also a reduced ordered moment and spreading of magnetic entropy much above T_N clearly tells that the system is highly frustrated system.

2.5 *Magnetic structure of Na_2IrO_3*

Na_2IrO_3 magnetic structure was first predicted from resonant x-ray magnetic scattering (RXMS) measurement performed by Liu et. al [Liu et al., 2011] . Their results show that Na_2IrO_3 has a long-range antiferromagnetically ordered ground state below T_N and that the ordering is three dimensional. From the azimuthal dependence of the magnetic peaks, the ordered magnetic moment is determined to be mainly along the crystallographic *a* direction. Two magnetic ordering structures are found to be possible candidates: zig-zag and stripy. Combining the experimental data with a set of constrained first-principles calculations, Liu et. al propose the zig-zag phase as the most likely ground state.

These results are confirmed by inelastic neutron scattering measurements on Na_2IrO_3 performed by Choi et.al , whose they report the first observation of dispersive spin wave excitations of Ir moments [Choi et al., 2012]. The dispersion can be quantitatively accounted for by including substantial further-neighbour in-plane exchanges which in turn stabilize zig-zag order.

In figure 2.7 the different spin structures are reported: (a) Néel (b)

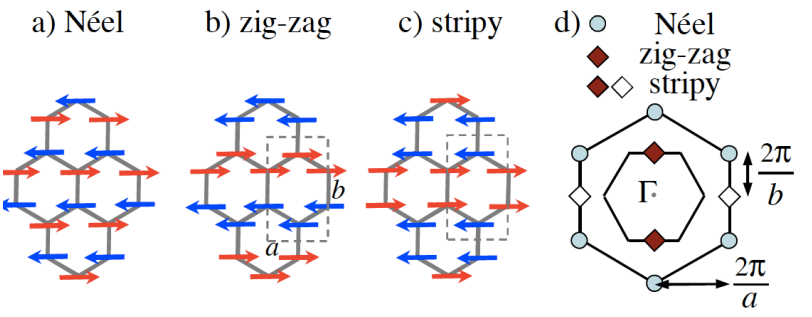

Figure 2.7: (a) Néel (b) zig-zag (c) stripy spin structure in honeycomb lattice. (d) Position of the magnetic Bragg peaks in reciprocal space for different spin-configurations. Measurement was done by Liu et.al [Choi et al., 2012]

zig-zag (c) stripy. Difference between zig-zag and stripy structure is very small: zig-zag can be depicted as antiferromagnetically coupled ferromagnetic spin chains and stripy is ferromagnetically coupled antiferromagnetic spin chains, if viewed along a-crystallographic axis of honeycomb lattice [Choi et al., 2012]. Another difference is that coupling between shortest Ir-Ir distance in Na_2IrO_3 is ferromagnetic in case of zig-zag and it is antiferromagnetic in case of stripy. From the spin density functional theory calculation [Liu et al., 2011] it was concluded that zig-zag spin-structure has lower energy so it is the true magnetic structure of Na_2IrO_3.

2.6 *Electronic structure under strong SOC limit*

In the section 1.3 we have seen that in $5d-$TMO materials, like Iridates, all the energy scale λ, J_H and U become almost same order of magnitude. In particular under strong the spin-orbit coupling limit, H_{SO} can not be treated as perturbation, so $\mathbf{L}$ and $\mathbf{S}$ do not commute with the total atomic Hamiltonian. From the LS coupling total momentum $\mathbf{J} = \mathbf{L} + \mathbf{S}$ is the good quantum number in the strong SOC coupling and can have the value from $|\mathbf{L} + \mathbf{S}|$ to $|\mathbf{L} - \mathbf{S}|$. In this section we want to analyse the electronic structure of Na_2IrO_3 under a strong SOC limit and we will see how the insulating behaviour and the magnetic ground state, that we have seen in literature, are described by J_{eff} model and Heisemberg-Kitaev model. respectively

2.6.1 *J_{eff} model scenatio*

The transition metal atom in Na_2IrO_3 is the Iridium whose atomic configuration is $[Xe]4f^{14}5d^74s^2$. In these kind of compounds (e.g Ir_2IrO_3, Sr_2IrO_4 etc..) Ir^{4+} ion forms covalent bond with O^{-2} ion sharing 4 valence electron of Ir. Two electrons come from $4s$ orbital and another 2 from $5d$ orbital. Hence the iridates valence band has $5d^5$ state, half filled $5d$-orbital. The crystal field of oxygen ligands

splits the degenerate 5d-states into two different states t_{2g} and e_g. Since in 5d Hund's coupling energy is of the order of 0.6 eV, which is much smaller than CF splitting ($2-3$ eV), the 5 electrons will be in lower t_{2g} state. If we turn on the SOC, we have to define the orbital angular momentum $|\mathbf{L}|$ of the t_{2g} orbital. Angular momentum matrix element for all the 5 electrons in t_{2g} will be given by $\langle t_{2g}|\mathbf{L}|t_{2g}\rangle$. Resulting angular moment matrix element is same as for the p orbital. Hence orbital angular moment of 5d-orbital L = 2 is quenched to L_{eff} = 1 in iridates by crystal field. The effective spin angular momentum is S_{eff} = 1/2 having one hole t_{2g} in 5d-orbitals. By LS coupling total angular momentum the 3-fold degenerate t_{2g} is split into J_{eff} = 1/2 state and doubly degenerate J_{eff} = 3/2 state due to strong SOC [Kim et al., 2008]. Among 5 electrons, 4 electrons are in the J_{eff} = 3/2 orbital and one is in the J_{eff} = 1/2 orbital. In this interpretation, the system shows a metal behaviour where the partially filled J_{eff} = 1/2 band is split from J_{eff} = 3/2 by a spin-orbit coupling term λ_{SO}=0.5 eV. With the inclusion of Coulomb interaction (U=$1-2$ eV) occurs a further split of partially filled J_{eff} = 1/2 band into ground state, lower Hubbard band (LHB), and first excited state upper Hubbard band (UHB), separated by U. In this way J_{eff} =1/2 LHB will be filled and J_{eff} =1/2 UHB will be empty. In figure 2.8 a schematic drawing of $J_{eff} = \frac{1}{2}$ model is reported. Electron in the spatially extended 5d orbital has very small U which can not split t_{2g} alone but it is much easier to split narrower J_{eff} =1/2 band by small U. Hence this insulating state is mainly due to strong SOC as we can see in figure 2.9.

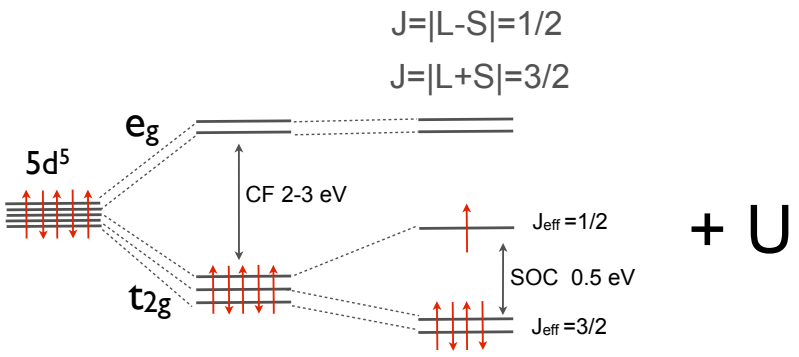

Figure 2.8: Splitting of $5d^5$ state under octahedral crystal electric field (CF) and spin orbit coupling (SOC). Schematics of electronic level splitting of J_{eff} =1/2 spin-orbit Mott insulating state. Red arrows represent 5 spins. Schematic drawing is based upon [Kim et al., 2008] by Kim et. al.

2.6.2 *Heisemberg-Kitaev model*

In the section 2.5 we have seen that the ground state of Na_2IrO_3 present a zig-zag antiferromagnetic order [Choi et al., 2012] [Liu et al.,

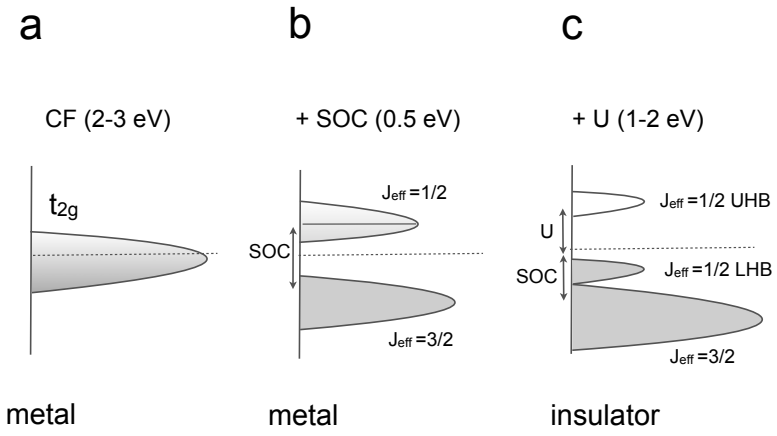

Figure 2.9: a) Partially filled t_{2g} orbital, splitting of it: b) by strong spin orbit coupling (SOC) into partially filled J_{eff} =1/2 and filled J_{eff} =3/2 state. c) Further splitting of partially filled J_{eff} =1/2 band into filled LHB and empty UHB by Coulomb repulsion U. Schematic drawing is based upon [Kim et al., 2008] by Kim et. al.

2011]. This type of ground state is explain by Heisemberg-Kitaev model (HK).

By inspection of the crystal structure in panel **b** of the figure 2.1 we can observe that each IrO_6 octahedron is connected to three neighbouring octahedra so that three t_{2g} orbitals of that Ir-ion participate in three different non equivalent hopping with three neighbouring Ir-ion mediated by the oxygen. In particular the two edge sharing octahedra form 90° Ir-O-Ir as reported by [Chaloupka et al., 2010]. From the panel **a** of the figure 2.10, we can see that along xx bond hopping happens between two neighbouring Ir t_{2g} orbital $|xz\rangle$ and $|xz\rangle$ via O p_x orbital, similarly for along yy bond hopping happens between $|xy\rangle$ and $|yz\rangle$ orbital via O p_y and for zz bond hopping happens between $|xz\rangle$ and $|yz\rangle$ orbital via O p_y.

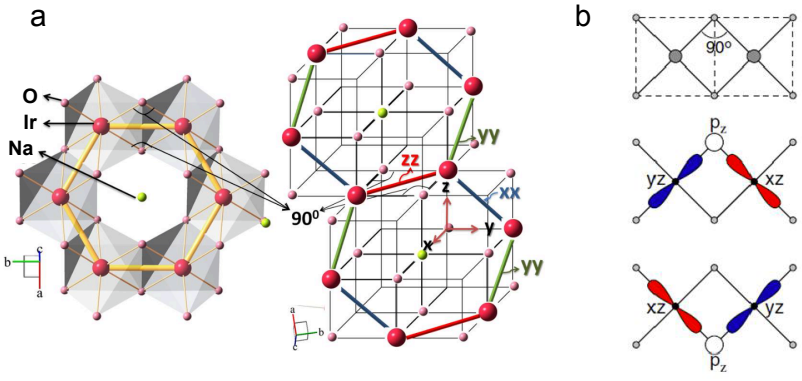

Figure 2.10: Honeycomb lattice of Na_2IrO_3. b) Edge sharing octahedra forms 90 Ir-O-Ir bond. [Jackeli and Khaliullin, 2009]

Chaloupka et. al. derived the total spin-Hamiltonian for honeycomb Na_2IrO_3 with the nearest neighbour (NN) interactions as

[Chaloupka et al., 2013]:

$$H = -K \sum_{<i,j>\gamma} S_i^\gamma S_j^\gamma + J \sum_{<i,j>} \mathbf{S}_i \cdot \mathbf{S}_j \tag{2.4}$$

The first term represents Kitaev exchange via three distinct NN bonds referred as $\gamma(=x, y, z)$ and K is the Ising-like ferromagnetic coupling between the NN Ir-spins. The second term represent the antiferrmagnetic Heisemberg exchange between NN spins where J is the AF spin-coupling. This term has a vector relation, so whatever is the spin direction of a Ir-atom, the NN spin will be in opposite direction.

To determine a phase diagram, 2.4 is parametrized as K =2α and J =$1-\alpha$ [Chaloupka et al., 2013]

$$H_{HK} = -2\alpha \sum_{<i,j>\gamma} S_i^\gamma S_j^\gamma + (1-\alpha) \sum_{<i,j>} \mathbf{S}_i \cdot \mathbf{S}_j \tag{2.5}$$

At α=0 only Heisenberg term contributes, HK model shows a Néel ground state. At the opposite limit α=1 2.5 corresponds to the exactly solvable Kitaev model with short-range spin liquid state [Kitaev, 2006]. There is also an intermediate state which α=1/2 and the ground state present a AF state with spins polarized in the direction of one of the crystallographic axis. Hence HK model gives three ground states shown in phase diagram in figure 2.11. Under T_N, Na_2IrO_3 shows a zig-zag (α=1/2) ground state in short-range regime, while has a quantum spin liquid (α=1) in al long range regime.

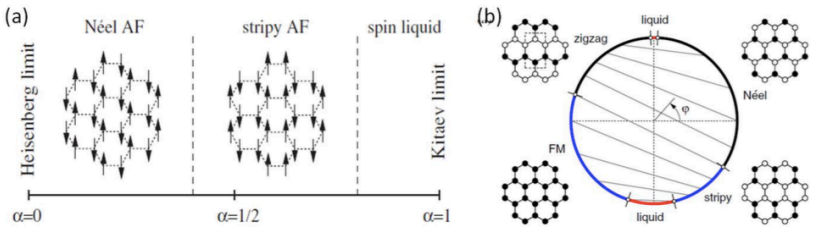

Figure 2.11: (a) Phase diagram of Heisenberg-Kitaev (HK) model with AF Heisenberg and FM Kitaev, reprinted from [Chaloupka et al., 2010] (b) Phase diagram of the generalized HK model containing all four combination of FM and AF; Kitaev and Heisenberg interaction, reprinted from [Chaloupka et al., 2013].

2.7 *Electronic structure under small SOC limit: QMO interpretation*

In the strong SOC limit localized J_{eff} states, described by J_{eff} model, it was assumed that the energy scales are W<λ<U, where W $\approx 4t$ is the d-electron band width, t the effective hopping parameter, λ the SOC parameter and U the on-site Coulomb repulsion. In this limit the electrons are on-site localized. However the single electron hopping t and the bandwidth for $5d$ orbitals is $1.5-2$ eV [Mazin et al.,

2012] and therefore it is unrealistic to expect a completely localized regime. The single electron hopping t would be an important factor which could give itinerant description of Na_2IrO_3. In this section we want to discuss the case in which the electronic structure is dominated by the formation of quasi-molecular orbital (QMOs) which involves six Ir atoms arranged in an hexagon [Mazin et al., 2012].

Starting from the non-relativistic case (without the inclusion of SOC effects), Mazin et. al. had performed DFT calculations and obtaining the relative band structure of Na_2IrO_3. In figure 2.12 the band structure of nonmagnetic Na_2IrO_3 for the experimentally determined crystal structure [Choi et al., 2012] is reported.

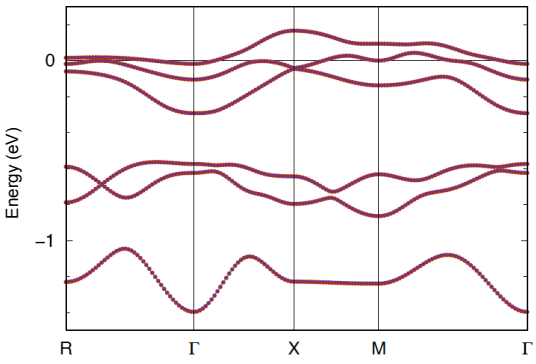

NN		S_{ap}
0	$xy \to xy$	−448.8
	$xz \to xz$	−421.5
	$yz \to yz$	−421.5
	$xy \to xz, xy \to yz$	−27.8
	$xz \to yz$	−23.1
1	$xy \to xy\,(t_{11})$	47.7
	$xy \to xz, xy \to yz\,(t_{10})$	269.6
	$xy \to xz, xy \to yz\,(t_{11})$	−25.6
	$xz \to xz, yz \to yz\,(t_{11})$	30.0
	$xz \to xz, yz \to yz\,(t_{1\bar{1}})$	−20.7
	$xz \to yz\,(t_{11})$	−21.4
$\bar{1}$	$xy \to xy\,(t_{\bar{1}\bar{1}})$	25.4
	$xy \to xz, xy \to yz\,(t_{\bar{1}1})$	−11.9
	$xz \to xz, yz \to yz\,(t_{\bar{1}1})$	33.1
	$xz \to yz\,(t_{\bar{1}0})$	264.4
2	$xy \to xy\,(t_{2a})$	−3.5
	$xy \to xz, xy \to yz\,(t_{20})$	−75.8
	$xy \to xz, xy \to yz\,(t_{2c})$	−36.5
	$xy \to xz, xy \to yz(t_{2d})$	12.5
	$xy \to xz, xy \to yz\,(t_{2e})$	−21.4
	$xz \to xz, yz \to yz(t_{2a})$	−0.6
	$xz \to xz, yz \to yz\,(t_{2b})$	−1.5
	$xz \to yz\,(t_{2c})$	−18.6
	$xz \to yz\,(t_{2d})$	10.2
$\bar{2}$	$xy \to xy\,(t_{2b})$	−1.4
	$xy \to xz, xy \to yz\,(t_{2c})$	−19.0
	$xy \to xz, xy \to yz\,(t_{2d})$	9.3
	$xz \to xz, yz \to yz\,(t_{2a})$	−1.4
	$xz \to yz\,(t_{2a})$	−77.0
	$xz \to yz\,(t_{2c})$	−30.4

Figure 2.12: Left: The Ir 5d t_{2g} band structure of Na_2IrO_3 obtained with DFT calculations in the generalized gradient approximations (GGA). Right: Nearest neighbour (NN) and second NN hopping integrals in meV between Ir t_{2g} orbitals for the experimental structure of Na_2IrO_3. The NN =0 data are Ir t_{2g} on-site energies and interorbital hoppings; the NN =1 and NN =$\bar{1}$ (NN =2 and NN =$\bar{2}$) data are hoppings over non equivalent NN (second NN) Ir bonds

From the electronic structure calculation is evident that the leading channel is the nearest neighbour (NN) O-assisted hopping between unlike orbitals. The panel **b** of the figure 2.12 shows the complete list of the hopping parameters up to the second nearest neighbours. We can identified the dominant hopping integrals for Na_2IrO_3 to be t_{10} ($\approx$ 270 meV) and t_{20} ($\approx$ 75 meV) for NN and second NN hopping respectively. Starting from the dominant hopping (t_{10}), let us consider an electron on a given Ir in a particular orbital state, say, d_{xy}, this electron can hop to a neighbouring state of d_{yz} symmetry, located at a particular NN site. From there, it can hop further into a d_{xy} state on the next site and after six hops it returns to the same state and site from where it started. This means that in the NN O-assisted approximation, where the hopping parameter t_{10} is about 270 meV, every electron is fully localized within six sites, forming a hexagon, as depicted in the figure 2.13 [Mazin et al., 2012].

Each Ir belongs to three hexagons, thus three different t_{2g} orbitals on each Ir site belong to three different quasi-molecular orbitals (QMO)(see figure 2.14). Six QMOs localized on a particular hexagon form six levels grouped into the lowest B_{1u} singlet with the odd parity, the highest A_{1g} with the even parity, and two doublets E_{1g} and

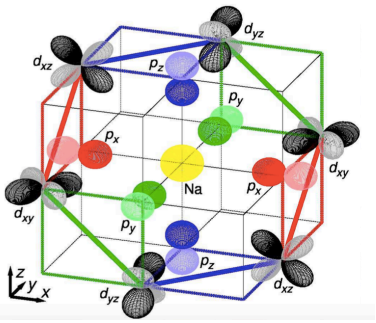

Figure 2.13: Most relevant O p-assisted hopping paths in idealized honeycomb structure, reprinted from [Mazin et al., 2012].

E_{2u} with even and odd parity respectively.

The projections of the total density of states of Na_2IrO_3 onto the quasi-molecular orbitals in non relativistic case and in nonmagnetic phase are reported in the panel **a** of the figure 2.17. Under these conditions the system present a metallic behaviour. The addition of the O-assisted NNN hopping t_{20} connects unlike NNN t_{2g} that belong to the same QMO and therefore retains the complete localization of individual QMOs. In figure 2.15 the comparison between band structure (red symbols) obtained by means of DFT (without spin-orbit coupling) and the tight-binding models (blue symbols) based on nearest neighbours up to 16 Angstrom ere reported.

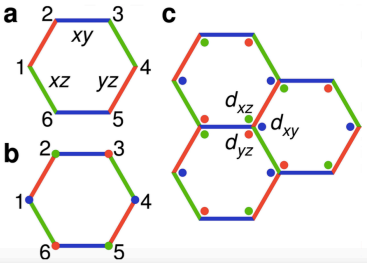

Figure 2.14: (a) Schematic plot of a Ir hexagon. b) A quasimolecular composite orbital on a given hexagon. c) Three neighbouring quasi-molecular orbitals [Mazin et al., 2012].

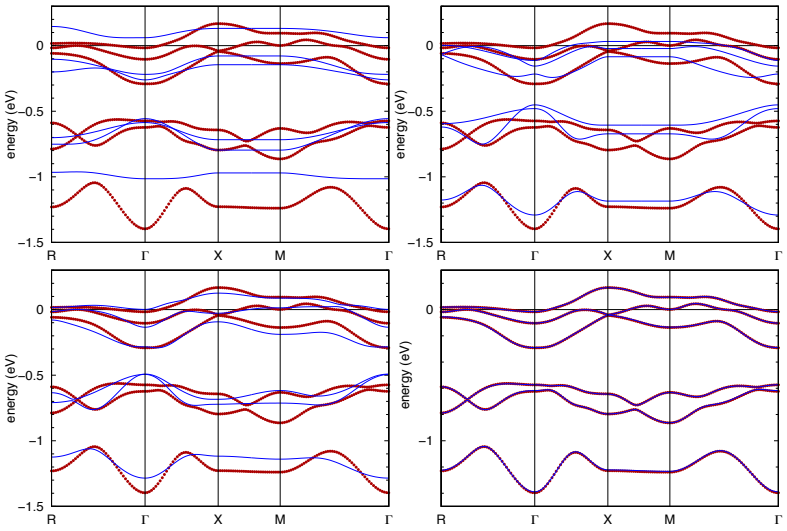

Figure 2.15: Band structure of Na_2IrO_3 (red) shown together with the tight-binding models that include only nearest neighbours (top left), up to next nearest neighbours (top right), up to third nearest neighbours (bottom left) and neighbours up to 16 Angstrom (bottom right).

In the nonrelativistic calculations the states are almost purely QMOs, ordered as B_{1u}, E_{1g}, A_{1g}, E_{2u} with increasing energy [Mazin et al., 2013]. The real-space representation of the QMOs in Na_2IrO_3 as a function of binding energy is reported in figure 3.3.

Turning on the spin-orbit coupling in the DFT calculations [Mazin et al., 2012] [Comin et al., 2012], we can observe a strong relativistic splitting in the upper two bands. In the panel **b** of the figure 2.20 the band structure and the density of states with the inclusion of spin-orbit coupling are reported. By inspection of the density of states and the band structures (the green dots in figure 2.18) [Mazin et al., 2012] obtained by GGA+SO calculations , we can observe that the lowest subbands hardly exhibit any spin-orbit effect, even though the spin-orbit parameter λ in Ir is $\sim$ 0.4-0.5 eV.

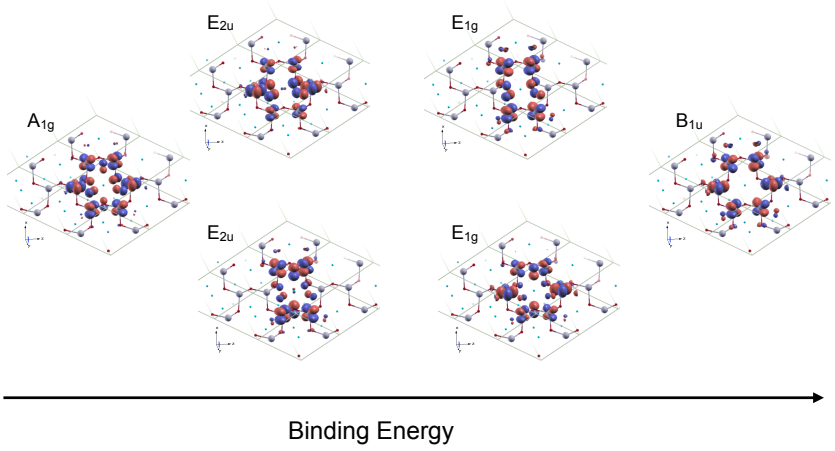

Figure 2.16: Real-space representation of the QMOs in Na_2IrO_3 as a function of binding energy obtained by the Wannier projector method [Foyevtsova et al., 2013].

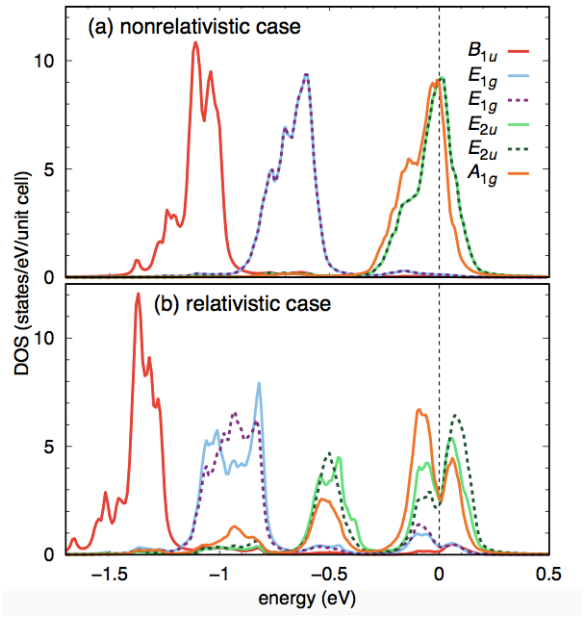

Figure 2.17: Density of the states of Na_2IrO_3 projected onto the six quasi-molecular orbitals for a) a nonrelativistic and b) a relativistic calculation

The density of states of Na_2IrO_3 projected onto the six quasi-molecular orbitals in the relativistic case, reported in panel **b** of figure 2.17, shows the QMOs mixing by spin-orbit interaction. The QMOs mixing in the relativistic regime is due to QMO energy and parity. QMOs with the same energy and different parity will be the most affected by the spin-orbit interaction and they will mix between them. In contrary, QMOs with different energy and same parity will not be affected by spin-orbit interaction. In fact, the spin-orbit coupling has the main effect of heavily mixing among themselves only the highest-in-energy three QMOs A_{1g} (even parity) and two E_{2u} (odd parity), leaving almost completely unaltered the lowest-in-energy three QMO ,B_{1u} and two E_{1g}, having different parity but also different energy. By inspection of the DOS in relativist case we can observe a suppression of the states at E_F therefore the system shows a insulating behaviour.

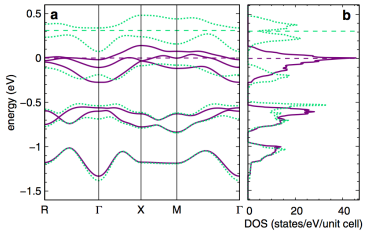

Figure 2.18: Electronic band structures and density of states of Na_2IrO_3 in non relativistic (solid purple line) and in relativistic regime (dotted green line) [Mazin et al., 2012] .

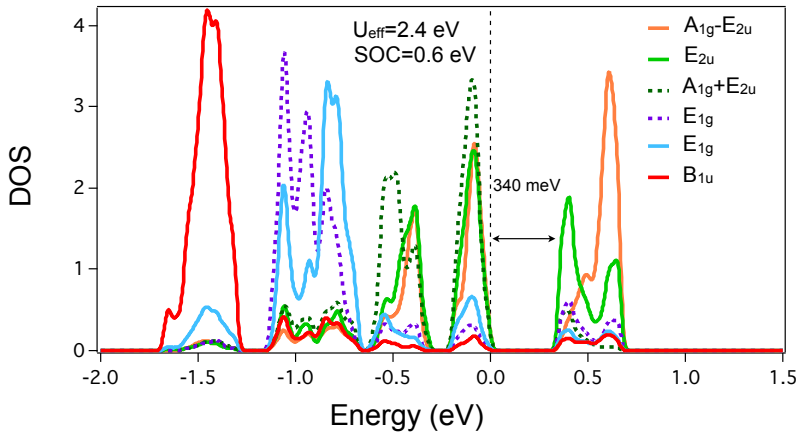

Figure 2.19: Ir $5d$ t_{2g} DOS and band structures for Na_2IrO_3, obtained with a)GGA, b) GGA+SO, and c) GGA+SO+U. Calculations was done by Li et. al [Li et al., 2015]

In order to have a good description of the experimentally observed optical gap in Na_2IrO_3, a Coulomb repulsion (U_{eff}=2.4 eV) had to be included in the DFT calculations. In the figure 2.19 the density of states obtained with GGA+SO+U of Na_2IrO_3 projected onto the six QMOs are reported. With the inclusion of Coulomb repulsion U, a 340 meV gap can be obtained as reported experimentally [Comin et al., 2012]. In figure 2.20 we report the band structures and the DOS for Na_2IrO_3 within GGA, GGA+SO and GGA+SO+U performed by [Li et al., 2015]. One of the most relevant effects of the QMO scenario of scenario is the capability to resolve in four bands what was before a unique band assigned by the J_{eff} scenario to J_{eff} = 3/2. In particular, the spin-orbit coupling leads to a clear predominance of the J_{eff}=1/2 characteristic in the upper quartet reconciling QMO

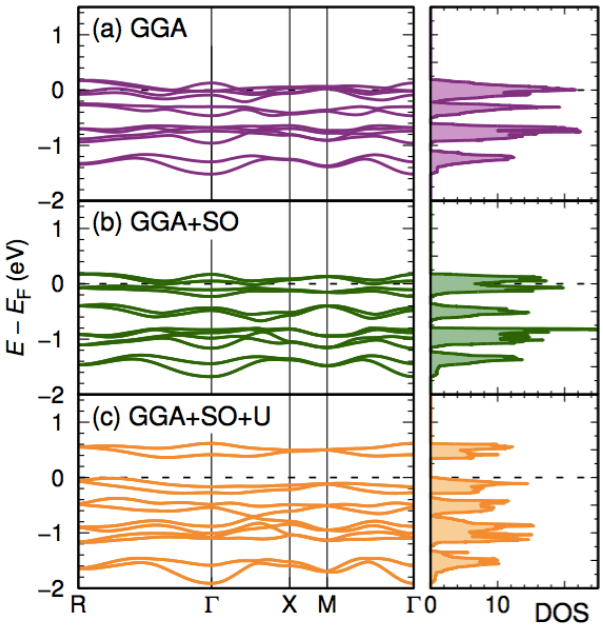

Figure 2.20: Ir $5d$ t_{2g} DOS and band structures for Na_2IrO_3, obtained with a)GGA, b) GGA+SO, and c) GGA+SO+U. Calculations was done by Li et. al [Li et al., 2015]

scenario with an almost-localized moment scenario (J_{eff} scenario) that would much more easily lead to the zig-zag magnetic ordering. Moreover, the spin-orbit coupling has the main effect of heavily mixing among themselves only the highest-in-energy three QMO (A_{1g} and $2E_{2u}$), leaving almost completely unaltered the lowest-in-energy three QMO ($2E_{1g}$ and B_{1u}).

3 Optical properties at equilibrium of Na_2IrO_3

In this chapter we describe the optical equilibrium properties of Na_2IrO_3. As a first step to interpret the experimental optical properties, we will discuss the optical conductivity calculated by density functional theory (DFT), including spin-orbit coupling (SO) and correlation effects (U). We will show how the main features of the experimental dielectric function of Na_2IrO_3 can be naturally explained within the Quasi Molecular Orbital picture [Li et al., 2015]. In this framework the main factor in determining the strength of the optical transitions is the parity of the quasi-molecular orbitals involved as initial and final states [Mazin et al., 2013]. Finally, we will present the results of the fitting of the multi-Lorentz model to the experimental optical conductivity of Na_2IrO_3 and we will compare the experimental results with the calculated one.

3.1 Optical costants

The dielectric function, $\epsilon(\omega)$, is a material-dependent complex function describing, in the frequency domain, the response of a material to an externally applied electric field $\vec{\mathbf{E}}(\omega)$: $\vec{\mathbf{D}}(\omega) = \epsilon(\omega)\vec{\mathbf{E}}(\omega)$ where $\vec{\mathbf{D}}(\omega)$ is the displacement electric field. From the microscopic point of view, $\epsilon(\omega)$ is related to the optical transitions in the material, that depend on the specific material band structure. From the macroscopic point of view, all the optical properties can be calculated starting from $\epsilon(\omega)$. In particular:

- The reflectivity R(ω). At normal incidence is given by:

$$R(\omega) = \left| \frac{1 - \sqrt{\epsilon(\omega)}}{1 + \sqrt{\epsilon(\omega)}} \right|^2 \tag{3.1}$$

- The complex index of refraction $n(\omega) = n_1(\omega) + in_2(\omega)$ is

$$n(\omega) = \sqrt{\epsilon(\omega)} \tag{3.2}$$

- The complex optical conductivity $\sigma(\omega) = \sigma_1(\omega) + i\sigma_2(\omega)$ is

$$\sigma(\omega) = i\frac{\omega}{4\pi}(\epsilon(\omega) - 1) \tag{3.3}$$

- Other useful relations (the frequency dependence is omitted) are:

$$\epsilon_1 = n_1^2 - n_2^2, \epsilon_2 = 2n_1 n_2 \tag{3.4}$$

$$n_1 = \sqrt{(|\epsilon| + \epsilon_1)/2}, n_2 = \sqrt{(|\epsilon| - \epsilon_1)/2} \tag{3.5}$$

$$\epsilon_1 = 1 - 4\pi\sigma_2/\omega, \epsilon_2 = 4\pi\sigma_1/\omega \tag{3.6}$$

The $\epsilon(\omega)$, $n(\omega)$ and $\sigma(\omega)$ are causal response functions (in the sense that no effect can occur before the cause) and their real and imaginary parts are mutually related by the Kramers-Kronig integral relations that allow to calculate the imaginary/real part if the corresponding real/imaginary part is known. The only requirement is that the measured quantity (real or imaginary) should be available over an infinite (or extremely broad) spectral range [Wooten, 2013]. The Kramers-Kronig dispersion relations for the dielectric function $\epsilon(\omega)$ are:

$$\epsilon_1(\omega) - \epsilon_\infty = \frac{1}{\pi} P \int_{-\infty}^{+\infty} d\omega' \frac{\epsilon_2(\omega')}{\omega' - \omega} \tag{3.7}$$

$$\epsilon_2(\omega) = -\frac{1}{\pi} P \int_{-\infty}^{+\infty} d\omega' \frac{(\epsilon_1(\omega') - \epsilon_\infty)}{\omega' - \omega} \tag{3.8}$$

where P denotes the Cauchy principal value [Wooten, 2013].

3.2 *Lorentz model*

Optical spectroscopy constitutes a powerful tool to investigate the electronic properties of solids, since it provides direct information about the underlying electronic structure [Wooten, 2013]. The most common models for reproducing a generic dielectric function are the classical Drude and Lorentz models. The Drude model is applied to describe the optical properties of a large number of metals while the Lorentz model describes well the optical properties of the dielectric materials. These classical models explain the response to a external electric field $\vec{\mathbf{E}}(\omega)$ of bound or free electrons in a solid. Basically, the Lorentz model treats an atom with electrons bound to the nucleus in much the same way as a small mass can be bound to a large mass by a spring. With this assumption an electron with mass m and charge e, when interacts with a electric field $\vec{\mathbf{E}}(t) = \int_{-\infty}^{\infty} \vec{\mathbf{E}}(\omega) e^{-i\omega t} d\omega$, is subject to:

- a driving force: $-e\vec{\mathbf{E}}(\omega)$
- a restoring forced (Hooke's law): $-m\omega_0^2\vec{\mathbf{r}}$

- a viscous dumping: $-m\gamma(d\vec{\mathbf{r}}/dt)$

where γ is the damping term, $\vec{\mathbf{r}}$ is the displacement, ω_0 is the resonant frequency and $\vec{\mathbf{E}}$ is the external electric field.

The motion of an electron bound to the nucleus is described by:

$$m\frac{d^2\vec{\mathbf{r}}}{dt^2} + m\gamma\frac{d\vec{\mathbf{r}}}{dt} + m\omega_0^2\vec{\mathbf{r}} = -e\vec{\mathbf{E}}(t) \tag{3.9}$$

There are two approximations in the equation 3.9:

a) the nucleus has been assumed to have infinite mass and

b) the interaction of electron with the magnetic field of the light wave is neglected.

In the frequency-domain, the solution to 3.9 is:

$$\vec{\mathbf{r}} = \frac{-e\vec{\mathbf{E}}(\omega)/m}{(\omega_0^2 - \omega^2) - i\gamma\omega} \tag{3.10}$$

Considering N atoms per unit volume, the macroscopic polarization is $\vec{\mathbf{P}}$

$$\vec{\mathbf{P}} = -Ne\cdot\vec{\mathbf{r}} = \frac{Ne^2\vec{\mathbf{E}}(\omega)/m}{(\omega_0^2 - \omega^2) - i\gamma\omega} \tag{3.11}$$

We can write the relative dielectric function as

$$\epsilon_r(\omega) = 1 + \frac{\omega_p^2}{(\omega_0^2 - \omega^2) - i\gamma\omega} \tag{3.12}$$

where:

- $\omega_p = \sqrt{\frac{Ne^2}{\epsilon_0}m}$ is the plasma frequency of the material;
- ω_0 is the resonant frequency of the oscillator;
- γ is the damping term. It is inversely proportional to the electron scattering rate τ;

The equation 3.12 is the Lorentz model and describes a resonant response to a time-varying electric field. Typically, to characterize the response of dielectric and metallic materials we have to use several (n)different oscillators. Equation 3.12 thus becomes:

$$\epsilon_r(\omega) = \epsilon_\infty + \sum_n \frac{\omega_{p,n}^2}{(\omega_{0,n}^2 - \omega^2) - i\gamma_n\omega} \tag{3.13}$$

where ϵ_∞ takes into account the effect of high-energy interbands transitions, which are usually not included in the model. Ideally when including all the possible interband transitions, we would have ϵ_∞=1. In figure 3.1 we plot the dielectric function $\epsilon(\omega)$ (panel **a**), the refractive index $n(\omega)$ (panel **b**), the conductivity $\sigma(\omega)$ (panel **c**) and the reflectivity $R(\omega)$(panel **d**) for a Lorentz oscillator, using 3.13.

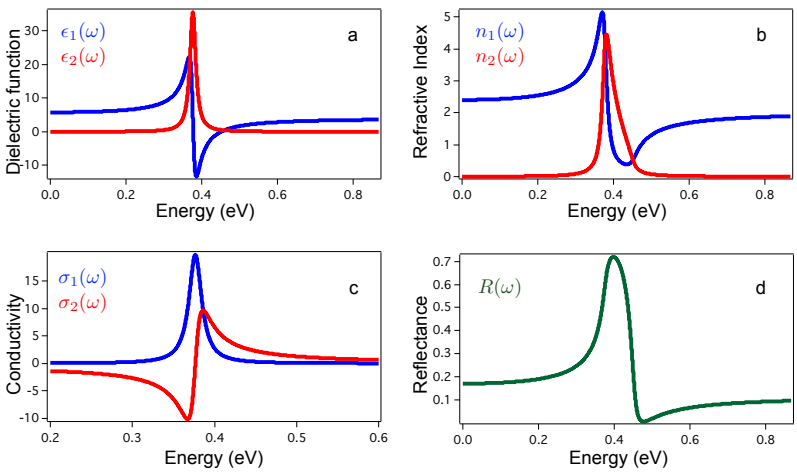

Figure 3.1: **a** dielectric function, **b** the refractive index from the equation 3.2, **c** the conductivity from the equation 3.3 and **d** the reflection from the equation 3.1. The material is modelled to consist of a single Lorentz oscillator of 3.13, with parameters ϵ_∞=4, ω_0=0.38 eV, ω_p=0.5 eV, γ=0.02 eV. The real and imaginary parts of the optical constants are plotted as blue and red, respectively.

If the oscillator is centered at zero frequency $\omega_0 = 0$, the equation 3.12 becomes

$$\epsilon_r(\omega) = 1 - \frac{\omega_p^2}{\omega^2 + i\gamma\omega} \tag{3.14}$$

and in terms of the conductivity

$$\sigma(\omega) = \epsilon_o \frac{\omega_p^2}{\gamma - i\omega} = \epsilon_o \omega_p^2 \left[\frac{\tau}{1 + \omega^2\tau^2} + i\frac{\omega\tau^2}{1 + \omega^2\tau^2} \right] \tag{3.15}$$

This model, generally called the Drude model, describes unbound charges and is useful for characterizing the response of good metals to electromagnetic waves.

3.3 *Optical conductivity and ab-initio band structure calculations*

In the section 2.7 of the previous chapter, we have discussed the electronic band structure of honeycomb lattice iridate, as calculated from density function theory (DFT). The reported DFT calculations were performed in both GGA [**?**] and LDA [Comin et al., 2012] approaches and both of them gave similar results. The theoretical results are in agreement with the experiments [Comin et al., 2012], [Sohn et al., 2013]. In this section we discuss the Na_2IrO_3 optical conductivity obtained by ab-initio calculations [Li et al., 2015].

The imaginary part of the interband contributions to the dielectric function is proportional to the real part of the optical conductivity (see 3.6), and it can be expressed as [Ferber et al., 2010]:

$$Re\sigma_{ii}(\omega) \propto \frac{1}{\omega} \sum_{c,v} \int d\mathbf{k} |p_{i;c,v,\mathbf{k}}|^2 \delta(\epsilon_{c_\mathbf{k}} - \epsilon_{v_\mathbf{k}} - \omega) \tag{3.16}$$

where p_i is the matrix element of the momentum operator along the electric field polarization of the incoming light, ω is the energy of the photon, $c_{\mathbf{K}}$ denotes a state in conduction band with energy $\epsilon_{c_{\mathbf{k}}}$ while $v_{\mathbf{K}}$ denotes a state in valence band with the energy $\epsilon_{v_{\mathbf{k}}}$.

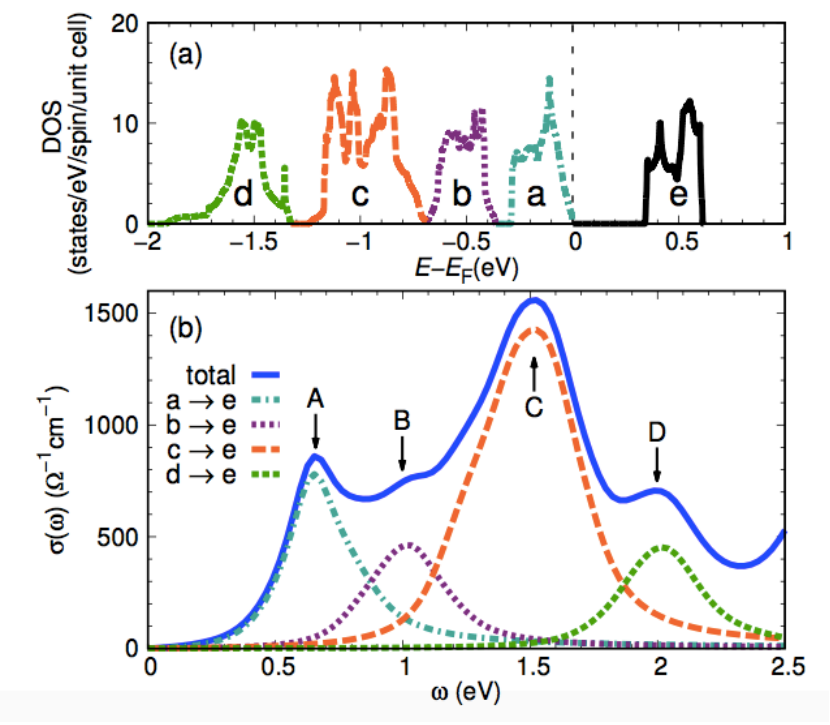

Figure 3.2: panel **a**:Density of the states of the Na_2IrO_3 obtained with GGA+SOC+U and panel **b**:The calculated optical conductivity for Na_2IrO_3 (blue solid line) and the 4 peaks that represent the contributions from different $d-d$ transitions. [Li et al., 2015]

With the optimized atomic parameters and setting zig-zag antiferromagnetic order phase, first principle calculations are performed in which relativistic effects and Coulomb repulsion (U_{eff}=2.4 eV) are taken into account. In the panel **a** of the figure 3.2 Li. et al present the Ir 5d t_{2g} density of states for Na_2IrO_3, obtained with GGA+SO+U. The valence states v_s are labeled by the letters **a**, **b**, **c**, and **d** while the conduction state c_s is labeled by **a**. In the panel **b** of the figure 3.2 (the solid blue line), Li. et al present the calculated optical conductivity in the low-energy region. The optical conductivity, obtained by DFT calculations, shows a multi-peak behaviour where the dominant peak is centered at ω=1.5 eV. Through the 5 states in the panel **a** it is possible to characterize the different features present in the optical conductivity; Li. et. al. identify 4 peaks A,B,C, D that correspond to the optical transitions from **a**, **b**, **c**, **d** to **e** states, respectively. These distinct peaks, that correspond to the contributions from different $d-d$ transitions, reveal the quasi-molecular orbital nature of the electronic structure of Na_2IrO_3 [Mazin et al., 2012]. We have seen

in the section 2.7 of the previous chapter, the features of the quasi-molecular orbitals, obtained in non-relativistic condition, in which their real-space representation are depicted in figure 3.3.

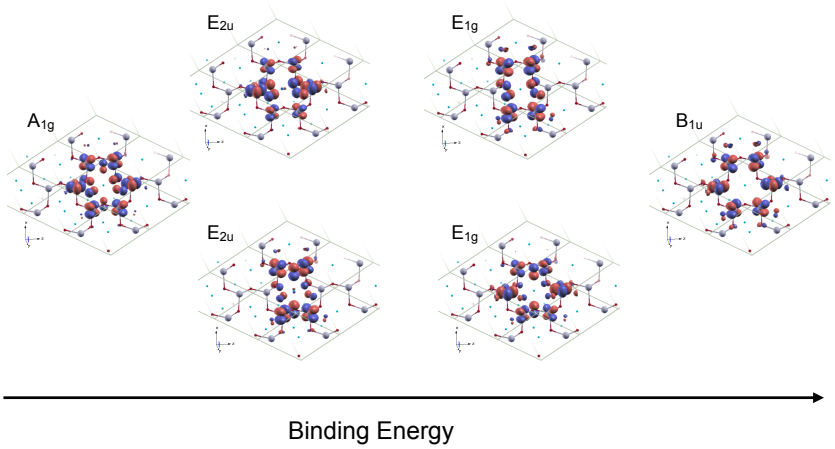

Figure 3.3: Real-space representation of the QMOs in Na_2IrO_3 obtained by Wannier projector method as a function of binding energy

By inspection of the six real-space representation of the QMOs in Na_2IrO_3 as a function of binding energy, we can discuss their parity. The g-orbitals (A_{1g}, E_{1g}) have even (gerade) parity, which means that the orbitals structures within each QMO are symmetric with respect to origin, i.e they remain unchanged after reflection. The u-orbitals (E_{2u}, B_{1u}) have odd (ungerade) parity, which means that the orbital structures have the opposite symmetry, i.e they change after reflection. When including spin-orbit coupling (SO) and the correlation effects (U), the QMO nature of the structures observed in the DOS (see figure 3.4). Therefore, we can argue that the states **a**, **b**, **c**, **d**, and **e** are predominantly of even, odd, even, odd and odd respectively.

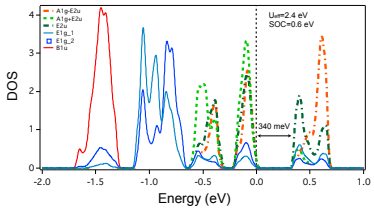

Figure 3.4: Density of the states of the Na_2IrO_3 projected onto the six quasi-molecular orbitals that are obtained with GGA+SOC+U

The strength of the optical transitions depends on the coupling between the valence and conduction bands and this is measured by the magnitude of the momentum matrix elements coupling the valence band states (v_s) and the conduction band state (c_s): $| < v_s|\vec{p}|c_s > |^2$, where $\vec{p}$ is the transition moment operator. Therefore, in accordance with the selection rule, transitions between states of the same parity will be strongly suppressed whereas transitions between states of different parity will dominate. In these terms, since the dominating contribution predicts an odd parity in conduction states c_s, the even parity valence states (**a** and **c**) will have much contribution than the odd parity valence states (**b** and **d**). The characteristics of the peaks shown, in panel **b** of figure 3.2, reflect the parity of the quasi-molecular orbitals: the peaks B and D, that are related to the

transitions **b** and **d** to **e**, are weaker than the peaks A and C, that are related to the transitions **a** and **c** to **e**. In particular we note that the structure centered at $\hbar\omega$=1.5 eV is strongly asymmetric, thus suggesting the presence of two neighbouring contributions with the same even parity. This is in agreement with the calculated band structure which reveal a multi-structure nature of the E_{1g} QMOs, as a consequence of the partial loss of their original degeneracy.

3.4 *Equilibrium optical properties of Na_2IrO_3*

In this section we describe the experimental equilibrium optical properties of Na_2IrO_3 , measured at different temperatures and in 0.7-2.5 eV energy range.

In figure 3.5 we report the real part of the optical conductivity $\sigma_1(\omega)$ of Na_2IrO_3 at different temperatures. In the inset of the figure 3.5 the reflectivity R(ω) has been reported. The optical response of the sample as a function of temperature was obtained using combined reflectivity and ellipsometry measurements on the (001) surface of a freshly cleaved crystalline platelet. These measurements have been performed at the quantum materials group of the University of Geneva. By inspection of the reflectivity reported in the inset of figure 3.5, we observe that the reflectivity is almost constant in the energy range between 0.7 eV and 1.7, eV while it starts decreasing in the 1.7-2.5 eV range.

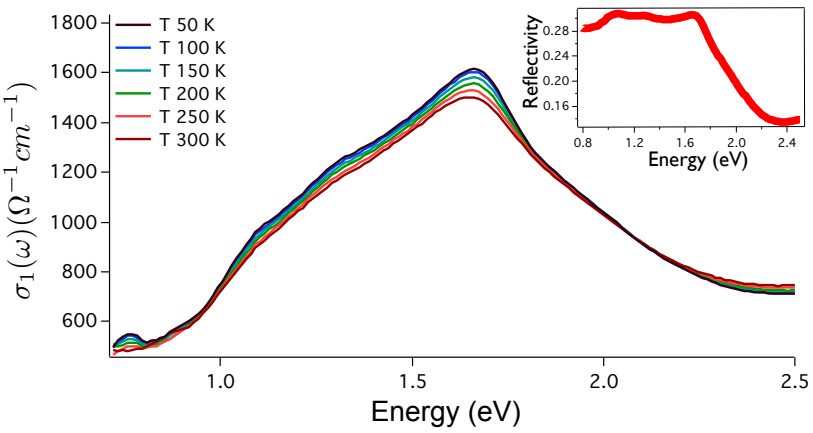

Figure 3.5: The real part of the optical conductivity of Na_2IrO_3, measured by static ellipsometry at T=50, 100, 150, 200, 250, 300 K. In inset the reflectivity of Na_2IrO_3 at T=50 K obtained by the same technique

The optical conductivity $\sigma_1(\omega)$ data in figure 3.5 (measured at different temperatures) is characterized by a a manifold of structures in the 1-2 eV energy range due to the interband transitions that involves the Ir t_{2g} orbital states, while the transitions involving the oxygen $2p$ bands are confined to higher energy ($>$ 2.5 eV) [Comin

et al., 2012]). From the figure 3.5 we can observe that at a frequency of about 1.6 eV, the amplitude of σ_1 at room temperature is slightly less intense than σ_1 at T=50 K. This effect is temperature-related: the decrease in temperature causes a narrowing of each transition structures (oscillators).

In order to disentangle the role of the different t_{2g} orbitals in determining the dielectric function, a sum of the Lorentz oscillators 3.13 is used to reproduce the optical conductivity σ_1 of the system. We have seen in section 3.1 that all the measurable optical quantities (reflectivity, optical conductivity, etc.) can be expressed in terms of the complex frequency -dependent dielectric function $\epsilon(\omega) = \epsilon_1(\omega) + i\epsilon_2(\omega)$, therefore the most important issue is the modelling of the ϵ_1 and ϵ_2. In order to have a correct model to fit the dielectric functions, the number of oscillators in the Lorentz model 3.13 has to be as small as possible. In the the panel **a** of figure 3.6, we report

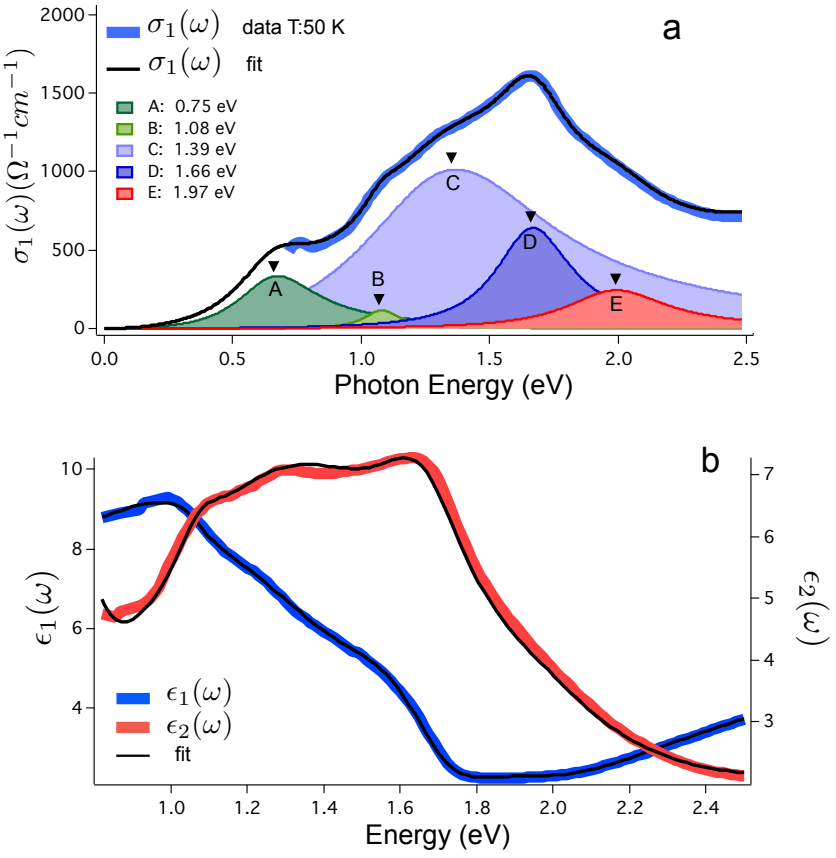

Figure 3.6: In panel **a** the optical conductivity at T=50 K and the Lorentz oscillators, as result from the fitting procedure, are reported. The six oscillators, the parameters of which are reported in 3.1, represent the interband transitions of the Ir t_{2g} orbitals. In panel **b** The real and imaginary parts of the dielectric function of Na_2IrO_3, measured by static ellipsometry at T=50 K, is reported. Solid lines are the fit to the data, performed with the Lorenz model using the same parameters as those used in the optical conductivity

the real part of the optical conductivity (blue solid line) and the fit to the data (solid black line). The minimum number of oscillators

in our model to get the fit to the optical data is five, labeled as A, B, C, D and E. The parameters of the oscillators, represented by the eigenfrequency (ω_0), the plasma frequency (ω_p) and the damping (γ), are reported in table 3.1. In panel **b** the real part (blue) and imaginary part (red) of the dielectric function with their respective fits (solid black line) are reported.

Na_2IrO_3 static optical parameters T= 50 K

	Position (eV)	Plasma Frequency (eV)	Width (eV)
A	0.75	0.46	0.14
B	1.08	0.36	0.17
C	1.39	2.88	0.99
D	1.66	1.097	0.32
E	1.97	0.77	0.46

Table 3.1: Lorentz model parameters used in the fit to the optical constants of the Na_2IrO_3 at T= 50 K

From the table 3.1 we can observe that the main contribution is given by the oscillators centered at ω_0=1.39 eV and ω_0=1.66 eV whose their spectral weights (ω_p) are much higher than the other oscillators. The fitting results show similarities with the ab-initio results described in 3.3.

3.5 *The relation between the Na_2IrO_3 optical conductivity and the QMO picture*

In this section we compare the results of the calculated optical conductivity (panel **b** of figure 3.2), presented in section 3.3, to the experimental optical conductivity reported in panel **a** of figure 3.6.

Both the experimental and calculated optical conductivities show the presence of a dominant peak at about ω=1.5 eV. In the analysis performed by Li.et.al, four interband transitions are identified whose intensities are related to the parity of the underlying quasi-molecular orbital nature of the electronic structure of Na_2IrO_3. On the other hand, the Lorentz model dielectric function fitting results to the Na_2IrO_3 , show that the minimum number of the Lorentz oscillators is five and that the peak at ω=1.5 eV in the ab-initio analysis 3.2 can be seen as the contribution from two different transitions, identified as the Lorentz oscillators C and D in the experimental results of figure 3.6.

The optical conductivity is an important measure of the underlying molecular orbital structure in Na_2IrO_3. In figure the panel **a** 3.7 a sketch of the GGA+ SO+U (S=0.6 eV and U_{eff}=2.4 eV) density of states, projected onto the quasi-molecular orbitals, is depicted. The states of the same parity (**b** and **e** in figure 3.7) have weak optical transitions whereas states of different parity (**a**, **c** and **d**) have strong

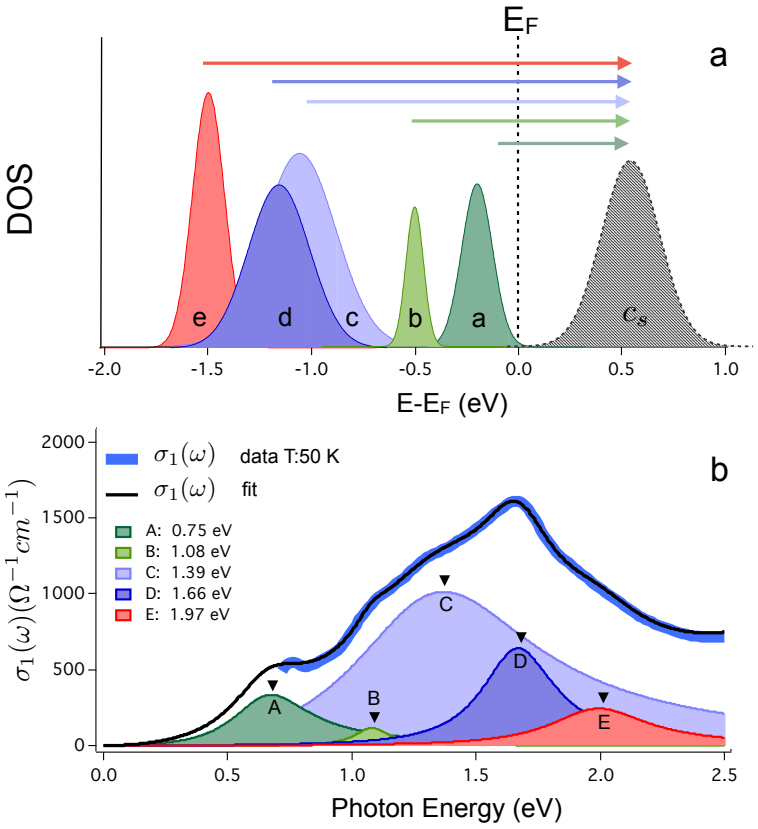

Figure 3.7: In **[a]** the density of the states with the valence states a (even), b (odd), c(even), d (even) e (odd) and the conduction state c_s (odd) are represented. In **[b]** the optical conductivity $\sigma(\omega)$ calculated by the five peaks, that correspond to the transitions from the valence states to conducting state.

optical transitions. The different contribution of these optical transitions are represented by the Lorentz oscillators, as reported in panel **b** 3.7.

4 Experimental setup

4.1 Introduction

The electronic and optical properties of materials (e.g. resistivity and dielectric function) stem from the complex interplay between the lattice, electronic and spin degrees of freedom , which generally interact on a timescale that ranges from 10^{-15} s to 10^{-9} s, or longer. Pump-probe spectroscopic techniques allow us to recover the dynamics of the electronic and optical properties on the femtosecond or picosecond timescales. Pump-probe spectroscopy can be used to determine the non equilibrium dynamics of electron-electron interactions [Groeneveld et al., 1995], to examine the coupling between electron, phonon and spin subsystem [Beaurepaire et al., 1996], to photoinduce nonthermal phase transitions [Cavalleri et al., 2001] [Yonemitsu and Nasu, 2008] and clarify to the electronic structure of complex materials [Demsar et al., 2003a].

In this chapter, after introducing the basics and methods for the ultrafast time-resolved pump-probe spectroscopy, we describe in detail the developed techniques. Three kinds of pump-probe techniques are described: single-color pump-probe setup, single-color pump supercontinuum-probe setup and dual-color ASynchronous OPtical Sampling (ASOPS) pump-probe setup. The last part of the chapter is dedicated to the time-domain THz spectroscopy and, in particular, to the setup that has been developed and employed in the present work.

4.2 Time-resolved optical spectroscopy: general remarks

The pump-probe technique measures the transient optical properties of materials with a temporal resolution that exceeds the electrical bandwidth of the conventional solid-state devices employed for electrical measurements. Typically, the train of pulses produced by an ultrafast laser source is divided in two beams: the more intense one, the pump beam, is used to excite the sample, while the less intense one, the probe beam, is used to measure the pump-induced change of the optical properties of the sample. To overcome limitations in

the response-time of the electronics, the pump-probe spectroscopy technique adopts an all-optical sampling method to reconstruct the signal. The ultrafast time domain signal is reconstructed by probing the pump-induced change of the reflectivity (or transmissivity) at a given time delay and repeating the measurements multiple times for each time delay. We will describe in the next sections the different ways to detect pump-probe signals.

In an ultrafast pump-probe measurements, the minimum time resolution is limited by the pump and probe pulses temporal lengths. The quantity that we measure in this work is the difference between the reflectivity of the excited system $R_{pumped}(\omega,\tau)$ (that depends of the delay between pump and probe beams τ) and the reflectivity of the equilibrium system $R_{unpumped}(\omega)$, divided by the equilibrium reflectivity:

$$\frac{\Delta R}{R}(\omega,\tau) = \frac{R_{pumped}(\omega,\tau) - R_{unpumped}(\omega)}{R_{unpumped}(\omega)} \tag{4.1}$$

This quantity depends on the delay between pump and probe pulses (τ) and on the probe photon energy ω.

4.3 Single-color pump-prope technique

4.3.1 Laser system

The first stage of the laser system is a diode pumped Nd:Yag laser (Coherent Verdi V10) which provides continuum monochromatic output with a wavelength of λ=532 nm and maximum output power of 10 W. This laser pumps a Ti:Sapphire oscillator (Coherent Mira 900) converting the input continuous wave beam into a train of ultrafast pulses characterized by a wavelength λ=800 nm and a temporal width of 120 fs. The output beam has horizontal polarization with a repetition rate of 76 MHz. The technique used to generate these pulses is the Kerr Lens Mode Locking which allows to induce a fixed phase difference between the cavity modes. The Ti:Sapphire crystal in Mira cavity is both the active medium which, pumped by the Verdi, emits light at about 800 nm and the nonlinear crystal responsible of the Kerr-lens modelocking. In fact the Ti:Sapphire crystal has a refractive index which depends of the beam intensity. Initially the modes change phase randomly; when they are in phase, the beam is focused and passes through the slit located after the crystal and the system stabilizes in this state which is energetically favorable.

The last component of the laser system is the cavity dumper which is an acousto-optical switch that allows to vary continuously the repetition rate of the laser from 1 MHz to single shot and to increase

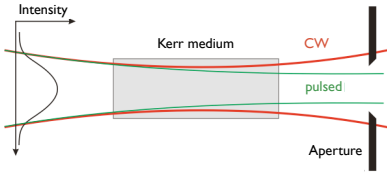

Figure 4.1: Scheme of Kerr lens effect with low intensity (red line) and high intensity (green line) light.

the energy per pulse as compared to the conventional cavities. This instrument is based on the acousto-optical effect for which an intensity modulation in a material generated by an acoustic wave induces a refractive index modulation of the material. The beam which passes through the crystal (silica) is partially diffracted at an angle that depends on the modulation periodicity. While the diffracted pulses are sent out of the cavity, the non-diffracted beam continues his path in the cavity, thus accumulating energy. The output energy per pulse from Mira oscillator and cavity dumper is about 40 nJ at 543 KHz of repetition rate. This laser system is exploited for single-color pump-probe experiments and for single color-pump supercontinuum-probe setup.

4.3.2 *Lock-in amplifier detection*

The $\Delta R/R$ signals are usually very small, in the order a few μV. Accurate measurements can be made even when the small signal is obscured by noise sources many thousands of times larger.

Figure 4.2: Lock-in amplifier

Lock-in amplifiers are used to detect and measure very small variations in the signal (down to a few nanovolts) and use a technique known as phase-sensitive detection to single out the component of the signal at a specific reference frequency and phase. Noise signals, at frequencies other than the reference frequency, are rejected and do not affect the measurement. To obtain a differential signal, the procedure is to acquire the reflected signal R with ("pumped") and without ("unpumped") the pump beam, and performing the difference with the correct parity. To modulated the pump beam, the most common way is to use an optical chopper, that is a device constituted by a disk with a mask of regular holes, designed in order to achieve a 50% duty cycle for the modulation. The laser beam is chopped by the disk at a frequency ranging from $\sim$ 1 Hz to $\sim$ 100 kHz. The lock-in amplifier can extract a large electrical signal, only a that component which has a frequency equal to that of an external reference. In a lock-in based pump probe experiment, we modulate the pump beam and the chopper frequency reference is brought to the lock-in. If the pump pulse has an effect on the optical properties of the system, the lock-in output will be only the pump induced variation of the optical properties.

There are two types of approach as to measure a pump-probe trace using lock-in detection. The first consists in acquiring the signal point-by-point, modifying the relative delay and subsequently acquiring the signal. In order to obtain a good S/N it is necessary to have a high signal average (typically 1 s per different delay) .

The second approach consists in scanning quickly the delay

between pump and probe, and acquiring continuously and synchronously the ΔR/R signal. This method requires a fast delay stage and constitues an advantage because, since every scan is completed on a time of the order of 1 s, it helps to suppressing the disturbing effects related to the laser source fluctuations. The limit of this acquisition technique is that the temporal windows of the acquisition should be kept as small as possible (of the order of 10-50 ps) since many scans are needed (usually 1000 scans give a good S/N). The speed of the delay stage (in ps/s), v_D, and the acquisition time window t_W of the acquisition system set the temporal resolution of the measurements according to the following formula of :

$$\Delta\tau(ps) = v_D(ps/s) \cdot t_W(s). \tag{4.2}$$

Considering a repetition rate source of 543 KHz and the pump beam modulated at $f_{chop} = 3$ KHz, t_W has to be greater (at least 10 times) than f_{chop}^{-1}, and in our single pump-probe measurements $t_W = 5$ ms.

4.3.3 *Single-color pump-probe experimental setup*

At the output of the laser source (see section 4.3.1), the beam is divided in two parts by a beam splitter (BS): 70% of the incident beam is transmitted (pump) while the remaining 30% is used as probe. The temporal delay between the two beams is varied by a motorized high-precision translational stage, placed on the pump path, which is controlled via software and allows to change the optical path in step of 0.1μm. The optical delay between the pump and probe beams is converted into the time coordinate by dividing by the speed of light. The intensity of both beams is tuned by an intensity attenuator given by an half-wave plate ($\lambda/2$) and a polarizer (P). In this type of measurements the pump and the probe beams have the same wavelength ($\lambda = 800$ nm) and are focused on the sample by two piano-convex lenses of 20 cm and 10 cm focal length. The superposition of the pump and probe beams is monitored by a CCD camera equipped with a 10x magnifying objective. In order to avoid any possible interference effect, the pump and probe polarizations are cross-polarized. The probe reflected by the sample is parallelized with a lens of the same focal length f and is refocused on a photodiode (PD). Since the relative variations of the probe are very low (if the total reflected signal corresponds to a voltage on the detector of 1 V, the relative reflectivity variation typically amounts to $\Delta R/R \approx 10^{-5}$) the signal acquisition is based on the lock-in detection (see section 4.3.2) referenced to the modulation of the pump beam by means a mechanical chopper, at a frequency of 3 kHz. For these kind of measurements is used the method of "fast scan", in order to reduce the noise for

the intensity drift of the laser system or the oscillations of the closed-cycle cryostat. In figure (4.3) the single-color pump-probe setup is depicted.

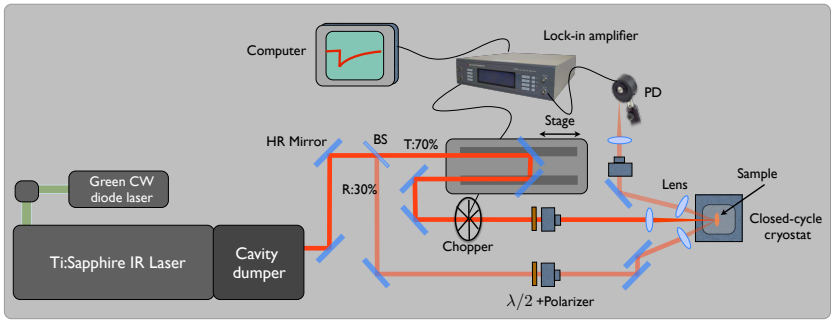

Figure 4.3: Experimental singlecolor pump-probe setup

4.4 *Single-color pump-Supercontinuum prope technique*

In this pump-probe technique the main important feature is the spectral resolution related to the probe pulse, which is a broadband pulse with a wide energy content. This type of pulse is generated by focusing the quasi-monochromatic probe beam (λ=800 nm) into a photonic crystal fiber. The laser system used for this type of measurements is Ti:Sapphire (Coherent Mira 900) coupled with the cavity dumper.

4.4.1 *Probe-Supercontinuum generation*

Supercontinuum generation is a process in which the quasi-monochromatic laser light is converted into light with a broad spectral bandwidth, while the spatial coherence remains high. The spectral broadening is accomplished by propagating optical pulses through a strongly non linear fiber. The physical processes behind supercontinuum generation in fibers can be very different, depending particularly on the chromatic dispersion and length of the fiber, the pulse duration, the initial peak power and the pump wavelength. When femtosecond lasers are used (as in our case), the spectral broadening can be dominantly caused by the combination of self-phase modulation and dispersion. If the dispersion characteristic of photonic crystal fibers is designed in such a way that the dispersion is zero close to the pump pulse wavelength (that in our case is λ=800 nm, fondamental of Ti:Sapphire lasers), the incoming pulse remains short upon propagation in the fiber, and the high peak intensities make it non-linearly interact with the core. The desired dispersion characteristic for the a PCF is obtained thanks to a microstructured cladding, which is

usually composed of a regular pattern of holes which surround the core [Dudley et al., 2006].

The photonic crystal fiber in our setup is the CrystalFiber FemtoWhite 800. This fiber is 12 cm long and its core diameter is 1.6 μm. After propagation into the fiber, the pulse is broadened into a white-light continuum which ranges from 450 to 1600 nm. This fiber is polarization maintaining, thus the supercontinuum is linearly polarized, in the same direction of the incoming pulse.

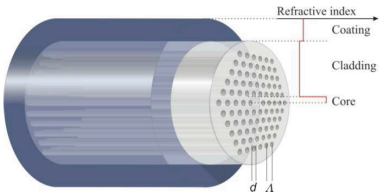

Figure 4.4: A section of the same fiber reveals its actual inner structure.

4.4.2 *Array detection system*

The photonic crystal fiber generates a spectrum in the range of 450-1600 nm. However, this range is limited by the sensibility range of the detectors that covers in the spectral range 200-1050 nm. The detector that we employed is the Hammamatsu *S*8380-128*Q*, which is composed of 128 pixel, each 50μm wide. The total active area, on which the supercontinuum is dispersed through the prism, is 6.4 mm long. The dispersion characteristic of the prism on the sensor is numerically calculated by taking into account the prism material refraction index and the prism dispersion law [Cilento et al., 2010]. The calibration of the array, that is the correspondence pixel-to-wavelength, is made selecting a specific wavelength by means of an interference filter and by recording its position on the sensor. About 4% of the supercontinuum beam is sampled before the interaction on the sample and used as the reference beam. For the acquisition of the transient spectrum $\Delta R/R(\omega, \tau)$ at fixed delay, we have to acquire the $R_{pumped}(\omega, \tau)$ and $R_{unpumped}(\omega)$. For each transient spectrum at fixed pump-probe delay, 2000 spectra $\Delta R/R(\omega)$ are recorded and averaged. To obtain a time and frequency resolved map of the material optical response, many $\Delta R/R(\omega)$ for different delays τ, must be collected. Usually, we record scans of 6 ps length. No lock-in technique is possible with this acquisition scheme. This is due to the array sensors which make available the data in a serial form: the voltage information, that is proportional to the illumination, for the 128 pixels is provided on the same electrical line at 2 MHz. Thus, the data acquisition can be performed solely by digitizing the train voltage values for 128 pixels. This limits the final S/N to a value around 10^{-4}, with an acquisition time of about 1 s. The acquisition is performed simultaneously for both the sensors (signal and reference), and the pixel-by-pixel ratio of the two voltages is immediately computed.

The acquisition is synchronized to the laser trigger (the modulation is on the pump beam by means of the mechanical chopper) in such a way that the same number of pulses is acquired for every spec-

trum, and a constant illumination level is generated, independently of the laser repetition rate. Each spectrum is the result of the accumulation 256 laser pulses since the limit is given by the acquisition boards, which cannot handle a trigger event rate of more then a 4-5 kHz. Each scan timing is about 15 min.

4.4.3 *Single-color pump-Supercontinuum prope experimental setup*

The experimental setup for single-color pump supercontinuum probe measurements is depicted in figure4.5.

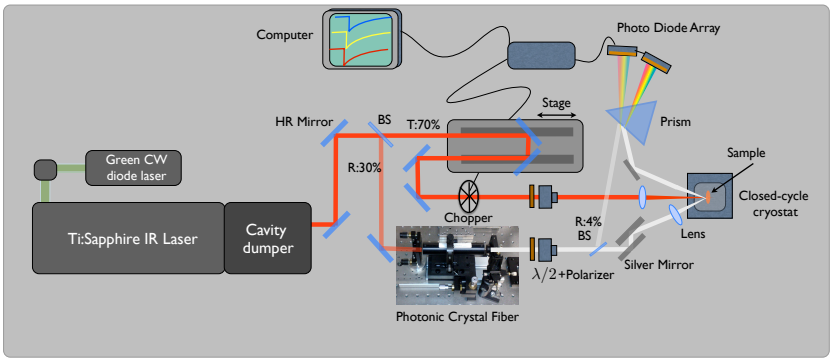

Figure 4.5: Experimental single color pump supercontinuum probe setup

At the output of the laser source, the beam is divided in two part by a beam splitter (BS): the 70% of the incident beam is transmitted (pump) while the remaining 30% is used to generate the supercontinuum light. The temporal delay between the two beams is controlled by a motorized high-precision translational stage, placed on the pump line. A low frequency chopper (20 Hz) is placed along the pump path to modulate the pump beam and perform differential measurements of the transient reflectivity variation. Then, the pump beam passes through a motorized lambda/half waveplate, followed by a fixed polarizer, to allow for a precise control of the pump intensity. The pump beam is focused at the sample position through a 20 cm focal length lens, while the supercontinuum beam is propagated by means of silver mirrors and it is focused at the sample position thanks to a 10 cm focal length achromatic doublet. The superposition of the pump and probe beams is monitored by a CCD camera equipped with a 10x magnifying objective. The probe reflected by the sample is recollected through a 10 cm focal length spherical mirror and is directed towards a prism, which disperses the different wavelengths in different spatial positions. A 20 cm focal length achromatic doublet is placed after the prism; , the linear array sensor is placed in the focus of the doublet.

4.5 ASynchronous OPtical Sampling pump-probe technique

In the conventional pump-probe technique, as we have seen in the sections 4.3 and 4.4, the pump and the probe are usually originated from a single mode-locked laser beam and then divided by a beam-splitter. The relative time delay between the two beams is achieved by a mechanical stage that changes the distance of one of the two beams, typically the pump. However, the most important drawback of this conventional method is the beam alignment instability for long delays of the stage (in addition to the slow acquisition time). This issue is irrelevant if we are interested in dynamics of the order of picosecods (e.g a delay time of 10 ps requires a delay of 1.5 mm), but it becomes serious when we want to study slower dynamics (e.g a delay of 10 ns would require a delay of 1.5 meters, making it impossible to maintain beam alignment). Asynchronous optical sampling (ASOPS) differs from the traditional pump-probe setup in its approach to control the time delay between the pump and the probe beams.

4.5.1 ASynchronous OPtical Sampling pump-probe technique

The ASOPS technique is able to overcome the issues of alignment by creating the time delay via a small difference in the repetition rate (Δf) of two synchronized femtosecond lasers. If the repetition rates of the two lasers are f_{probe} and f_{pump}=$f_{probe} + \Delta f$ where Δf is the detuning, the time delay between each pair of pump and probe pulses will increase as multiple of

$$\Delta\tau = \frac{\Delta f}{f_{probe} \cdot f_{pump}} = \frac{\Delta f}{f_{probe} \cdot (f_{probe} + \Delta f)} \tag{4.3}$$

The ASOPS approach involves no moving parts (no translation stages) and thus eliminates the instability problem inherent to the delay line method. The maximum time delay of the scan is $1/f$. The time-resolution of the measurements is then given by two other factors: the width of the pulses and the bandwidth the detection electronics. The bandwidth B of the detection electronics is 350 MHz.

The detuning Δf can be selected in the range 1 Hz-10 KHz; for example with a typical Δf=1KHz, the time resolution is $\Delta\tau$=100 fs and it takes $1/f$=1 ms to complete the scan.

The ASOPS system consists of a pair of fiber laser, each driven by a passively mode-locked fiber ring laser with Erbium as active medium. Each laser generates a train of pulses with a central wavelength of 1560 nm, a repetition rate of around 100 MHz and a pulse length of about 200 fs. One laser (the slave laser) is phase-locked to the other laser (the master laser) to synchronize the two repetition

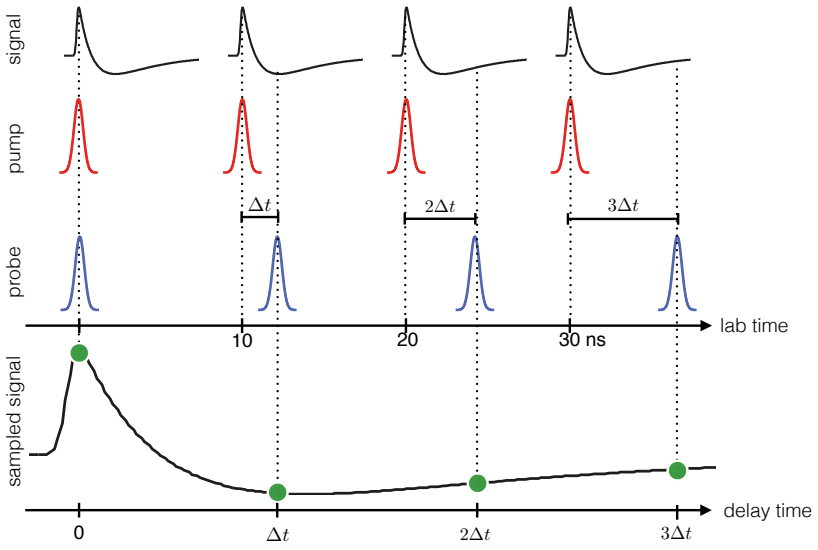

Figure 4.6: ASOPS scheme . In top) Actual sample response. In the middle) Pump (1560 nm) and probe (780 nm) pulses with frequency offset gradually increasing the time gap between them. In bottom) The detected signal.

rates. The repetition rate difference is maintained via a feedback loop and piezo motors. The 1560 nm beam generated by the slave laser is sent to the second harmonic generation module. Inside this module, the beam goes through a periodically poled lithium niobate (PPLN) crystal and frequency-doubled to 780 nm. The beam coming out of the PPLN crystal goes through a dichroic mirror and separates into a 780 nm beam and a 1560 nm beam [Stoica et al., 2008]. The output power of both of ASOPS lasers is $\sim$ 150 mW.

4.5.2 *ASynchronous OPtical Sampling detection*

In order to measure the transient reflectivity with the ASOPS technique we don't use the lock-in amplifier detection scheme, but simply a balanced amplified photodetector (BPD). Balanced photodetection is realized when two phohtodiodes are connected such that their photocurrents cancel with each other. In this case, it is necessary to equalize the DC optical power that hits upon each photodiode by using a variable neutral density filter. When this is done, the effective output of the balanced pair of photodiodes is zero until there is some difference in the intensity of one of the beams (pump-induced).

When this occurs, it causes the pair to become "unbalanced" and a net signal appears on the output. In particular the reflected probe beam is detected by "input $+$" port (see figure 4.7) of the balanced detector, meanwhile a small percentage of the probe beam that does not interact with the sample is detected by "input $-$" port. The subtracted signal from the two ports is sent to the data acquisition board on a computer. For the measurements we use a detuning Δf=1

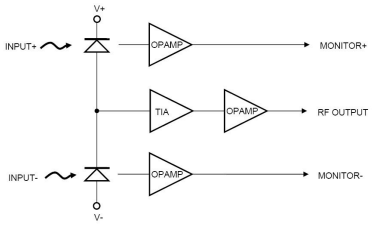

Figure 4.7: Electronic scheme of Balanced Photodetector.

kHz that allow us to investigate dynamics of 10 ns with a resolution of $\Delta\tau$=150 fs and the time for a single scan is very fast, 1 ms.

4.5.3 *ASOPS experimental setup*

The figure 4.8 shows a sketch of the experimental ASOPS setup. The 1560 nm beam from the master laser acts as the pump beam, while the 780 nm beam from the slave laser acts as the probe beam. The intensity and polarization of each beam is adjusted by a half-wave plate coupled with a polarizer. As a consequence of the asynchronous sampling scheme, the paths of the probe and the pump beams not necessarily must be the same. A reference probe beam is required in order to detect the reflectivity variation by the balanced amplified photodetector. The 780 nm laser path is divided in two part by a beam splitter: the 70% of the incident beam is transmitted and used to probe the reflectivity variation, while the remaining 30% is used as the reference. Pump and probe beams are focused on the sample with a piano convex lens of 20 cm and 10 cm. Since the pump beam is invisible to CCD camera (λ=1560 nm), the superposition of the pump and probe beams is found generating the sum of frequency (SHG) using non-linear crystal (BBO) and then fixing the probe beam (λ=780 nm, visible) with the CCD camera. The probe

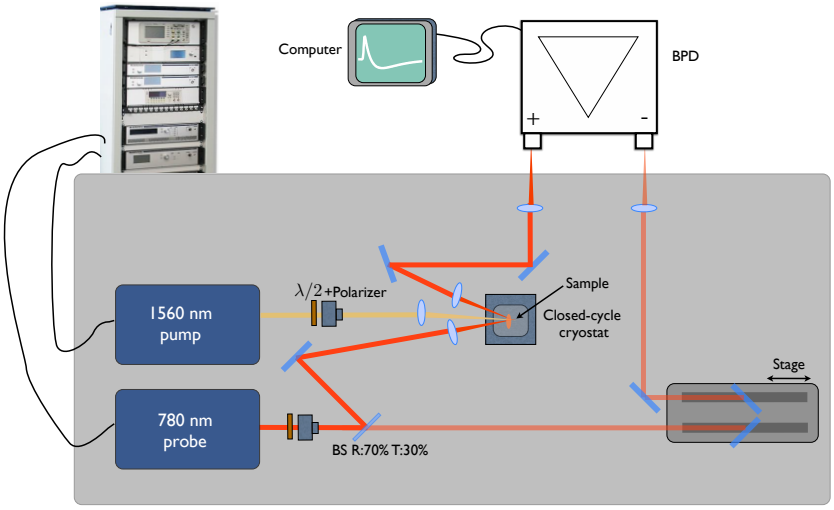

Figure 4.8: Experimental ASOPS setup

reflected by the sample is parallelized with a 10 cm local length lens and is refocused on the photodiode "input+" port. The balanced photodetector measures the difference in intensity between the probe pulse (which contains the pump-induced sample reflectivity variation) and the reference pulse. The intensities and the phase shift of these pulses are carefully equalized before the differential

acquisition. In order to do that, a translational stage is place on the reference line. When the pulses impinge on the fast detector exactly at the same time, the difference between them will be zero. A variable neutral filter is used to equalize the optical power impinging upon each photodiode.

4.6 Closed-cycle cryostat

To cool down the samples studied in the experiments we use an closed-cycle cryostat (DMX-20) to allow the temperature of the sample be varied in the range 10-350 K. A water-cooled compressor cycles high-purity helium at a high pressure through heatsick within a vacuum chamber. Thermal energy from the heatsink flows into the cooler gas, the gas is pumped out, raised to high pressure again, and the excess heat is transferred to water at room temperature, before the gas is cycled back through. This system has the advantage of only requiring electricity and water, the helium itself being contained internally and thus can be run for long periods of time uninterrupted.

The internal structures within the cryostat are made from oxygen-free high thermal conductivity copper (OFHC) and the sample holder is directly coupled with the cryostat cold finger. Such a cryostat is strongly affected by mechanical vibrations: the motor that alternates which gas line is connected to the heatsink and the compressor is very mechanically noisy. To avoid the problem related to the vibrations the cold finger has been mechanically separated by the vibrating parts of the cryostat. In order to move the cryostat, and therefore the sample, along its x-y-z axes keeping the decoupling between the motors and the a three-axis manipulator has been ad-hoc developed. The temperature near to the sample region is accurately measured with a calibrated Cernox sensor and is controlled by a controller (Lake shore). The latter has a PID feedback system that stabilizes the sample within ± 0.1 K from the set temperature. The system is kept in UHV thanks to a pumping system composed of a scroll pump combined with a turbomolecular pump. A base pressure in the order of 10^{-8} mbar can be reached inside UHV chamber. The UHV chamber is equipped with UHV optical window, through which the pump and probe impinge on reach the sample.

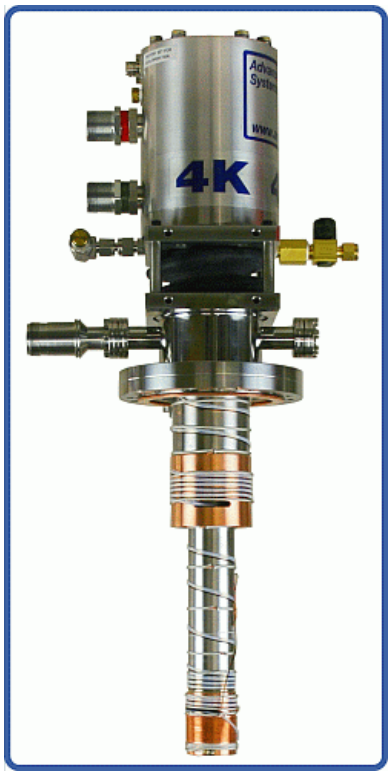

Figure 4.9: closed-cycle cryostat DMX 20.

4.7 Time-domain terahertz spectroscopy setup

Terahertz (THz) frequency electromagnetic radiation lies between infrared and millimetre wave radiation in the electromagnetic spectrum. Figure 4.10 illustrates the THz band in the electromagnetic spectrum, which merges into the neighbouring spectral bands .

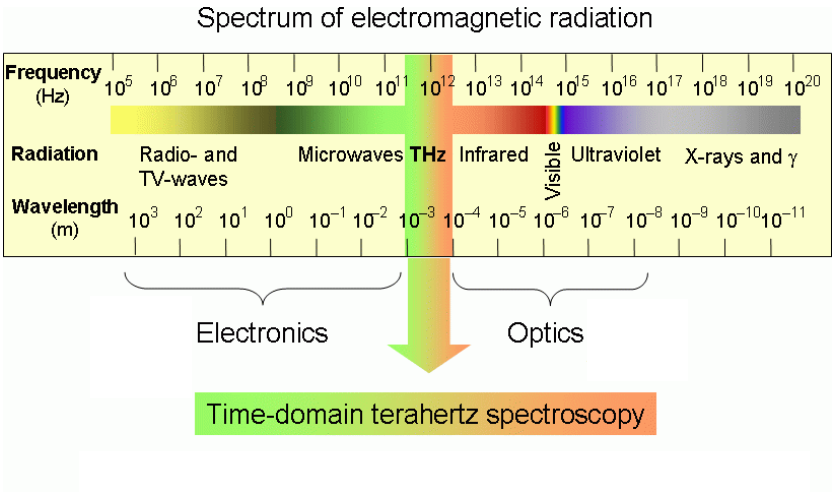

Figure 4.10: Terahertz band in the electromagnetic spectrum.

The units that are frequently used in the THz science are the following:

- Frequency: $\nu = 1$ THz
- Period: T$= \nu = 1$ps
- Angular frequency: $\omega = 2\pi\nu = 6.28$ THz
- Wavelength: $\lambda = c/\nu = 300\mu$m
- Wavenumber: $\hat{k} = k/2\pi = \lambda = 33.3$ cm^{-1}
- Photon energy: h$\nu = \hbar\omega = 4.14$ meV
- Temperature: T=h$\nu/k_B = 48$ K

There are many different approaches for the generation and detection of THz radiation which include both coherent and incoherent systems. Coherent system can be divided into continuous-wave or pulsed systems. We will focus on the pulsed THz systems, since we will start from an ultrashort pulsed source. Pulsed THz emission under excitation of ultrashort laser pulses has been observed from different materials such as metal, semiconductors, superconductors, organic and inorganic materials and air plasma. The emission of pulsed THz radiation can be attributed to various effect: photoconductive antenna structure [Auston et al., 1984], optical rectification [Chuang et al., 1992], transient current effect, coherent polarization oscillations, coherent phonons, coherent plasmon oscillations [Dekorsy et al., 1995], [Garrett et al., 1996], [Kersting et al., 1997], transitions in coupled quantum wells and ultrafast modulation of the

superconductivity in high T_c superconductors. The most common mechanisms for broadband pulsed THz emission from semiconductors using ultrashort pulses are photoconductivity and optical rectification in nonlinear crystals.

4.7.1 *Photoconductive mechanism*

A photoconductive antenna (see figure 4.12) consists of two metallic electrodes that are depositated onto a semiconductor substrate (typically GaAs). The substrate is photoexcited with ultrashort laser pulses with energy above the gap which cause electron-hole pairs to be generated in the semiconductor. These photocarriers are then accelerated by the applied external DC bias voltage, which creates a transient current gradient and radiates THz pulses. The polarization of the THz wave is parallel to the bias field, which is perpendicular to the gap between the two electrodes. The laser pulses need to have an energy larger than the bandgap of the semiconductor to generate photo-induced free carriers [Tani et al., 2006]. Because of the pulsed nature of the laser beam, the amplitude of this current is a function of time and, thus, the derivative of the current with respect time generates the THz pulse.

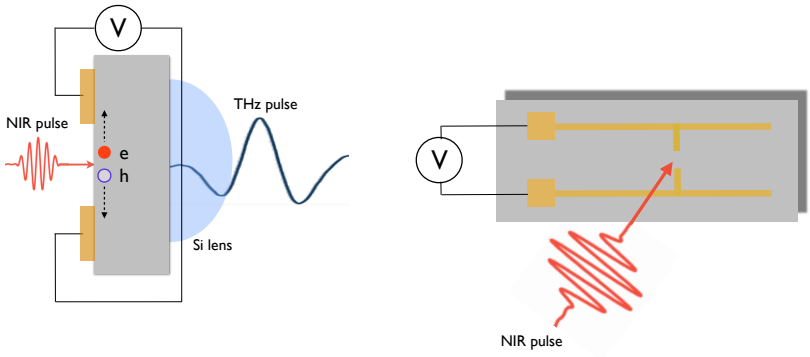

Figure 4.11: Photoconductive emission mechanism. Photocarriers, generated from the antenna substrate under excitation of NIR pulses, are accelerated by the external bias voltage and emit transient THz pulses.

$$E_{THz} = \frac{Ae}{4\pi\epsilon_0 c^2 z}\frac{\partial N(t)}{\partial t}\mu E_b \tag{4.4}$$

where A is the area of illumination, ϵ_0 is the permittivity in vacuum, c is the speed of light, e is the electron charge, z is the penetration of the laser pulse into the semiconductor, μ is the mobility of the carriers, E_b is the bias field, and N the density of photo-carriers.

4.7.2 *Electro-optical rectification*

In this mechanism, the optical excitation causes a change in the polarization of the crystal by exploiting the nonlinearity of the material to produce sum-frequency and difference-frequency polarization components. For ultrashort NIR pulses, the polarization components with difference frequencies are in the THz range [Chuang et al., 1992], [Greene et al., 1992]. The THz field in terms of second-order nonlinear polarization components can be written as :

$$E_{THz}(\Omega) \propto \frac{\partial J(\Omega)}{\partial t} = \frac{\partial^2 P(\Omega)}{\partial t^2} = \chi^{(2)} \frac{\partial^2 E_{laser}(\Omega)}{\partial t^2} \tag{4.5}$$

where χ is the second-order susceptibility tensor, E_{laser} is the incident excitation electric field and $P^2(\Omega)$ is the second-order polarization at frequency $\Omega = \omega_1 - \omega_2$.

Electro-optical rectification does not need bias to realize THz generation. For a given material, the radiation efficiency and bandwidth are affected by factors such as thickness, laser pulse duration, absorption and dispersion, crystal orientation, and phase matching conditions [Khurgin, 1994]. In particular:

- **Laser pulse duration**. The shorter is the duration of the laser pulse, the wider is the bandwidth of the THz spectrum.
- **Absorption**. It refers to the absorption of the laser pulse and the THz waves by the material. The higher is the absorption, the lower is the THz output power.
- **Phase matching**. An optimal THz wave generation occurs when the group velocity of the laser pulse is equal to the phase velocity of the THz pulse.
- **Dispersion**. It refers to the fact that the different frequency components contained in the laser pulse can propagate at different velocities within a material. Dispersion affects the phase matching characteristics of the crystal and it has a major impact on bandwidth and radiation efficiency. The higher the dispersion, the more difficult is to achieve phase matching and, therefore, narrower bandwidth.
- **Crystal thickness**. the thinner is the crystal, the broader is the bandwidth of the THz pulse because different matching conditions have smaller effect due to the reduced interaction length. However, thinner crystals tend to generate lower output powers and introduces secondary echoes very close to the main THz pulse that reduces the practical scan length, and thus, the frequency resolution.

Many nonlinear materials are used for THz emission via the optical-rectification mechanism: semiconductors such as GaAs [Wu and Zhang, 1997], ZnTe, InP , InAs [Gu et al.], [Reid et al., 2005] or dielectric crystals such as lithium tantalate ($LiTaO_3$) or organic materials, polimers and metals such as gold. Among them, ZnTe is the most favorable as THz wave emitter because of its high nonlinear coefficient, high damage threshold, and best phase matching characteristics with Ti:Sapphire laser (far-infrared pulses). The range of ZnTe spans approximately 0.1-3 THz. The tensor property of χ implies that the nonlinear process will strongly depend on the orientation of the light polarizations with respect to the crystal axes. For normal incidence the more efficiently cut for the ZnTe crystal is in the $< 110 >$ orientation and the angle between the near-IR pulse polarization and the in-plane axis $[110]$ of the crystal is $\approx 54.7^\circ$.

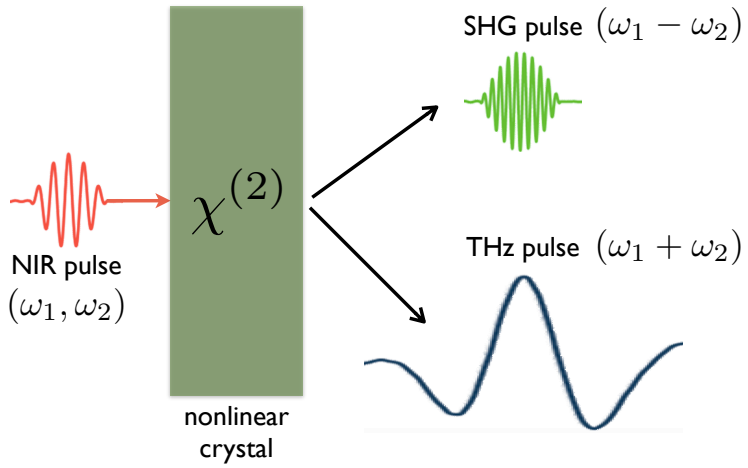

Figure 4.12: Optical rectification mechanism. The incident NIR pulse exploits the nonlinearity property of the crystal and generates sum frequency (SHG) and difference frequency (DFG) components.

4.7.3 *Therahertz Detection: Electro-optical sampling*

The emission mechanism of electro-optical rectification (and also for photoconductive antenna) can be reversed and used for the detection of THz pulses. Electro-optical sampling is based on the Pockels effect, in which the birifrangence properties of a material are induced or modified by the application of an electric field. In the electro-optical sampling method, the THz field is measured by the change it causes on the birifringence of ZeTe crystal [Lee, 2009]. Such changes in the birifrangence of the crystal can be measured by analysing the polarization properties of an optical probe beam going through the crystal. To measure the THz waveform with electro-optical sampling a balanced measurement is usually adopted. A schematic representation of electro-optical sampling is depicted in

figure 4.14. A linearly polarized optical probe beam goes through a polarizer and then travels through the nonlinear crystal; a quarter wave plate (QPW) located after the nonlinear crystal changes the ellipticity of the probe beam and a Wollaston prism (WP) separates the two perpendicular components of the elliptical polarization. The difference of the intensity of the perpendicularly-polarized beams (horizontal and vertical) is detected by a differential balanced photodiode. When no THz wave is illuminating the nonlinear crystal, the ellipticity of the probe beam can be set so that the two intensities are equal and the net current from the differential photodiodes is zero. When the THz wave illuminates the nonlinear crystal, the electric field associated with the THz wave changes the birifrangence of the material and, thus, changes the ellipticity of the sampling beam (800 nm). This variation of the ellipticity breaks the balance between the two beams with different polarization and, therefore, a net current, that is proportional to the amplitude of the electric field of the THz wave,, is generated on the differential photodiode. Scanning the probe beam at different delays respect than the THz beam on the nonlinear crystal, we can reconstruct the THz waveform.

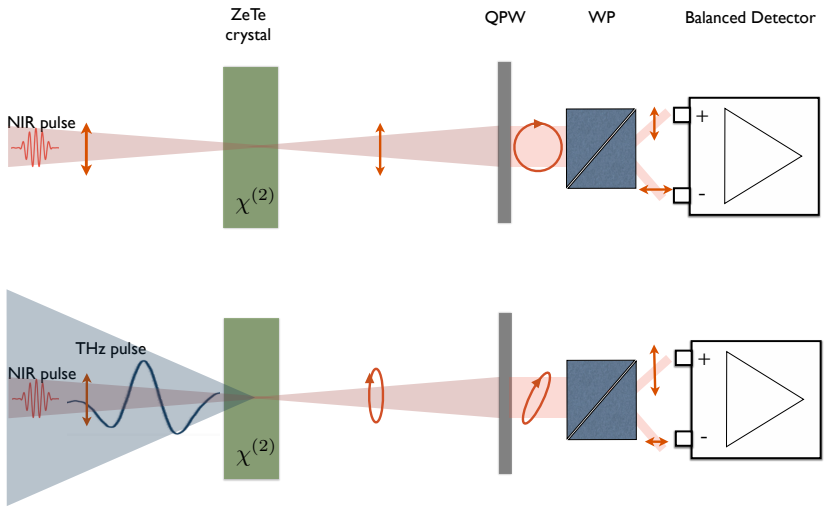

Figure 4.13: Electro-optical sampling mechanism. Probe polarizations with and without a THz field are depicted before and after the polarization optics.

4.7.4 *Terahertz Time-Domain Spectroscopy setup*

A schematic representation of the THz time domain spectroscopy setup is illustrated in figure 4.15. The modelocked Ti:Sapphire (see section 4.3.1) provides a train of femtosecond optical pulses that are divided into two arms. One laser beam (95%) is used to generate the THz radiation by means of a ZnTe nonlinear crystal. The second laser beam (5%) is used to detect the generated THz radiation by means of

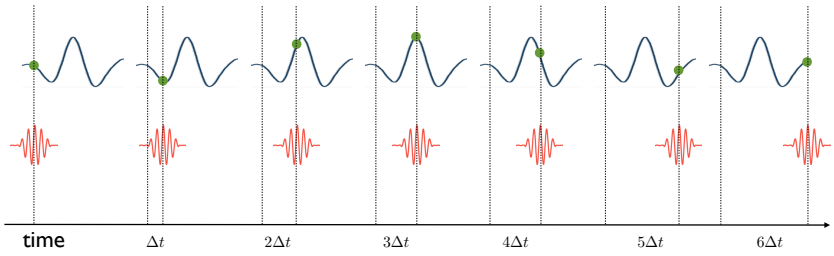

Figure 4.14: Electro-optical sampling mechanism. Many sampling pulses (red) interact with THz pulses (blue) at different positions. In this way is possible to reconstruct the time-domain THz waveform

electro-optical sampling. In this latter beam, the sampling line, it is placed a stage which is controlled via software and allows to change the path length of the sampling pulse, in order to detect the the entire THz waveform.

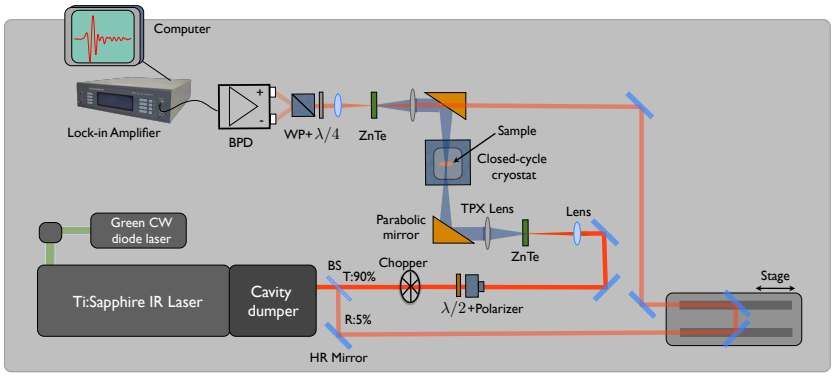

Figure 4.15: Optical rectification mechanism. The incident NIR pulse exploits the nonlinearity property of the crystal and generates sum frequency (SHG) and difference frequency (DFG) components.

To generate the THz radiation, the 800 nm Ti:Sapphire pulses are focused into the ZnTe nonlinear crystal with 10 cm focal length lens. The nonlinear crystal used for THz generation has <110> orientation with a thickness of 1 mm. The THz pulses (and also the residual part of 800 nm pulses) are collimated with a 5 cm focal lenght TPX lens and focused into the sample with a 15 cm parabolic mirror. After the TPX lens a white paper is put on the THz line so that the THz radiation goes through the paper without absorption while the residual 800 nm radiation is blocked. The THz beam is then collimated with a second 15 cm parabolic mirror and focused into the ZnTe nonlinear sampling crystal with a 5 cm focal length TPX lens. The latter parabolic mirror has a central hole of 3 mm diameter. In this way the sampling 800 nm pulses are collinear with the THz pulses for the electro-optical sampling. The sampling beam output of the nonlinear crystal is parallelized with 5 cm focal length lens and then collected in the electro-optical sampling scheme (see section 4.7.3). The ZnTe nonlinear crystal used for the optical sampling has

the same type of cut of the generation one, but has a thickness of 0.5 mm. The acquisition scheme is lock-in based (see section 4.3.2). The differential balanced photodiode signal is sent to the lock-in amplifier that measure the difference of sampling beam intensity polarizations that come out from the Wollaston prism (WP). To maximize the S/N we modulate the THz beam with a chopper that works at 3 kHz, which is used as the reference for lock-in detection. The THz detection is point-by point, modifying the relative delay between THz pulse and sampling pulse and subsequently acquiring the signal. The water vapour shows strong absorption lines in the THz frequency bands. The water content and relative humidity of the environment would therefore significantly influences on the THz frequency spectra at certain frequencies [Slocum et al., 2013]. In offer to minimize the water line absorption, a plexiglas box , fluxed by gaseous nitrogen, is built around the THz line.

4.7.5 *From time-domain to frequency-domain data*

Through the electro-optical sampling we are able to reconstruct the THz pulse electric field in the time domain. To switch from the time-domain data to frequency-domain we compute a Fourier Transform of the acquired signal. The general result of computing the Fourier transform is a complex function, which provides amplitude and the phase information of the THz field detected [Kauppinen and Partanen]. In this way the real and the imaginary parts of the optical properties (refractive index, dielectric function, conductivity) of a material can be measured without indirect methods such as Kramers-Kronig transformations. The Discrete Fourier Transform (DFT) and Inverse Discrete Fourier Transform (IDFT) are the practical method to computed the FT and are calculated as:

$$DFT : Y_k = \sum_{n=0}^{N-1} x_n \cdot e^{-2\pi i \frac{k}{N} n} \tag{4.6}$$

$$IDFT : x_n = \frac{1}{N} \sum_{k=0}^{N-1} Y_k \cdot e^{-2\pi i \frac{k}{N} n} \tag{4.7}$$

Therefore computing the DFT, the waveform is multiplied by a sampling window. The multiplication of the waveform $x(t)$ and the sampling window $w(t)$ means that the FT is the result of

In the FT, frequency resolution (Δf) and bandwidth (B) are functionally related to the window lenght (T) and the sampling interval (Δt) respectively [Oppenheim et al., 1989] . Three main aspects should be considered in a THz-time domain measurement

- **Frequency resolution versus window length.** Frequency resolution (Δf) is inversely proportional to the window length.The

longer the window length is, the higher the frequency resolution that we can get.

- **Bandwidth versus sampling rate (Nyquist-Shannon theorem).** An analog signal (THz field pulse) can be perfectly reconstructed if the sampling rate f_{SR} is at least twice the bandwidth B, which is defined as the highest frequency component of the signal. Typical THz system have a bandwidth of 3 THz, which requires a sampling frequency of at least 6 THz.

- **Etalon effect.** Most THz system show echoes of the original THz pulse due to the reflection of the THz pulse at the interferences of the optical elements such as beam splitters and lenses. If such echoes are included in the Fourier Transform, the result is a spectrum with interference features knows as Etalon effect that make the analysis of the spectrum very difficult. One way to solve the problem is to limit the maximum frequency resolution (i.e to reduce the length of the scan).

5 Single color pump probe measurements on Na_2IrO_3

Introduction

In this chapter we report time-domain reflectivity measurements on Na_2IrO_3, as a function of temperature and probed and by 1.55 eV (λ=780 nm) pulses. We will present two different pump-probe setups, which have been developed to investigate the relaxation dynamics on very different time windows: in the conventional pump probe setup, based on Ti:sapphire oscillator, the delay between the pump and the probe is tuned by a mechanical translator which controls the difference of the relative optical path of the two beams; in the second scheme, the time resolution is obtained by exploiting the frequency detuning between two high repetition rate fiber lasers. In the later case, the dynamics can be easily investigated up to the nanosecond timescale without the use of any mechanical stage. These measurements evidenced a specific dynamics, which diverges as T_N is approached. After few nanoseconds, the energy excess provided by pump pulse is dissipated and the system cools down recovering the initial condition before the excitation. Our conclusion is that the dynamics probed by the 1.55 eV pulses is directly proportional to the magnetic dynamics of the systems.

5.1 Single-colour pump-probe measurements at room temperature

In this paragraph we report the measurements of reflectivity variation as a function of delay time (τ) between pump and probe performed at T= 300 K, on Na_2IrO_3. The quantity that we measure is:

$$\Delta R/R(\tau) = \frac{R_{exc}(\tau) - R_{eq}}{R_{eq}} \tag{5.1}$$

where R_{eq} is the static reflectivity of the system and $R_{exc}(\tau)$ is the reflectivity after a time τ from the pump excitation. In these measurements both pump and probe pulses have the same energy of 1.55 eV

(i.e $\lambda = 800$ nm). Once that signal Δ R/R(τ) is optimized at high pump fluence ($\sim 450\mu J/cm^2$), we decrease the pump power until a fluence of $8\mu J/cm^2$ is reached. In figure 5.1, the red trace is the Δ R/R(τ) signal, measured at room temperature. At negative delays, i.e. before the pump excitation, the reflectivity variation is zero. At $\tau = 0$, i.e. when the pump and probe overlap in time, we suddenly observe a negative reflectivity variation with amplitude of $1.2 \cdot 10^{-4}$. At positive delays ($\tau > 0$) the measured reflectivity variation is still negative and gradually recovers the equilibrium value, exhibiting a dynamics characterized by two different timescales. In order to study more deeply the ΔR/R(τ) dynamics, the following double exponential function has been fitted to the data:

$$f(\tau) = y_0 + A_1 exp\left(\frac{-\tau}{\tau_1}\right) + A_2 exp\left(\frac{-\tau}{\tau_2}\right) \tag{5.2}$$

where τ_1, A_1, τ_2, A_2 are the time and amplitude values of the first and the second exponential, respectively. As we can see in figure 5.1 the double exponential function well describes the measured dynamics. The two timescales which characterize the dynamics, turn

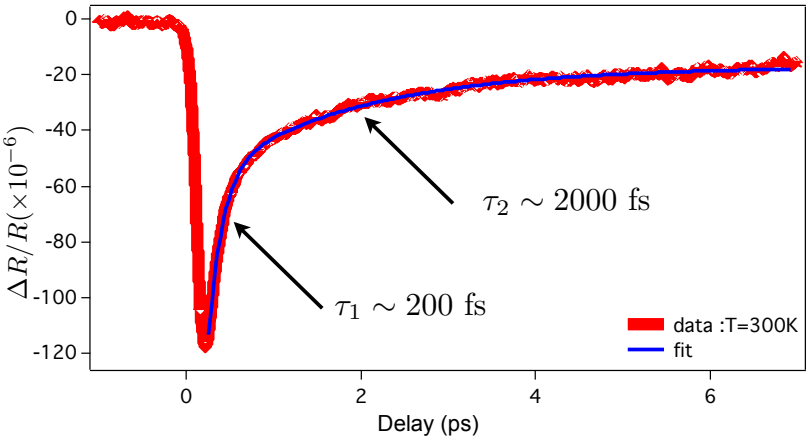

Figure 5.1: The red trace represents time-resolved optical signal (in reflectivity) measured on Na_2IrO_3 at room temperature. The blue is the double exponential function 5.2 fitted to the data. This double exponential function is characterized by two relaxation dynamics: $\tau_1 = 200$ fs and $\tau_2 = 2000$ fs

out to be $\tau_1 = 200 \pm 10$ fs and $\tau_1 = 2000 \pm 50$ fs. Once characterized the dynamics of the reflectivity variation at room temperature, we cool down the sample at T= 10 K, i.e. below its Néel temperature ($T_N = 15$ K) and we performed a low temperature measurements with the same the time resolution and time window. Since at low temperature the specific heat significantly decreases [Singh., 2010], the pump-probe measurement can be strongly affected by the local average heating related to the mean power of the laser beams. To avoid this effect, the pump fluence was kept at $8\mu J/cm^2$, corresponding to an average power of 90 μW. Below T_N we can see that the

reflectivity variation has a minimum value of $\sim -1 \cdot 10^{-4}$ (a little bit less than the room temperature) but after several picoseconds the reflectivity variation becomes positive. Using the same fit

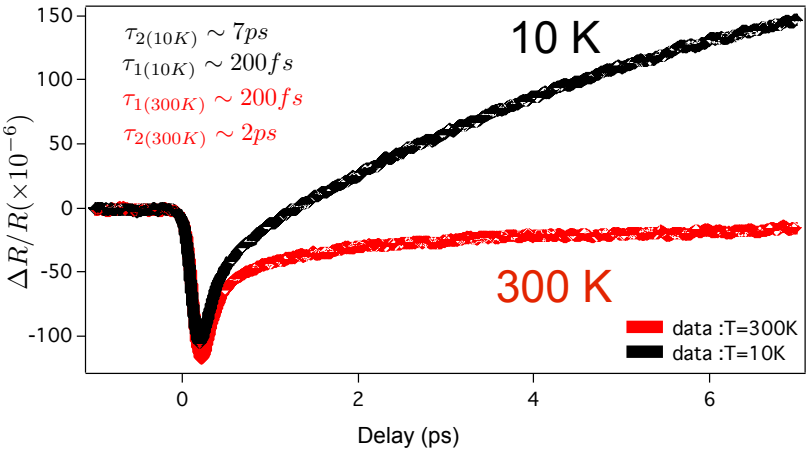

Figure 5.2: The red trace represent the reflectivity variation signal measured on Na_2IrO_3 at room temperature. The black one is the reflectivity variation on Na_2IrO_3 at T= 10 K.

formula (5.2) for the measured signal at low temperature (black trace in figure 5.2) we find that the amplitude A_1 and the time τ_1 of the first exponential have the same values than those at room temperature. The second exponential parameters, however, are much greater respect than room temperature; we found that at 10 K, $\tau_2 = 7000 \pm 100$ fs (instead of $\tau_2 = 2000 \pm 100$ fs at room temperature) and also the amplitude A_2 of the second exponential is about one of magnitude larger than that at room temperature.

5.2 *Single-color pump-probe as function of the pump fluence and the temperature*

In order to clarify the role of the excitation fluence in determining the relaxation dynamics, a study as a function of the pump fluence at fixed temperature T= 10 K has been carried out. Figure 5.3 reports the reflectivity variation at four different pump fluences: 30 μJ/cm^2, 80 μJ/cm^2, 160 μJ/cm^2, 320 μJ/cm^2. The probe fluence is maintained at 8μJ cm^2. The measured ΔR/R(τ) signals in figure 5.3 are normalized and shows a different behaviour as the pump fluence is increased. In details: at 30 μJ/cm^2 pump fluence (black trace) the negative fast reflectivity transient is accompanied by a slower positive component; increasing the pump fluence to 80μJ/cm^2 (red trace) we see that, while the fast component of the reflectivity variation remains almost constant, the slow positive signal is partially quenched as compared to the scan obtained at lower fluence. This dif-

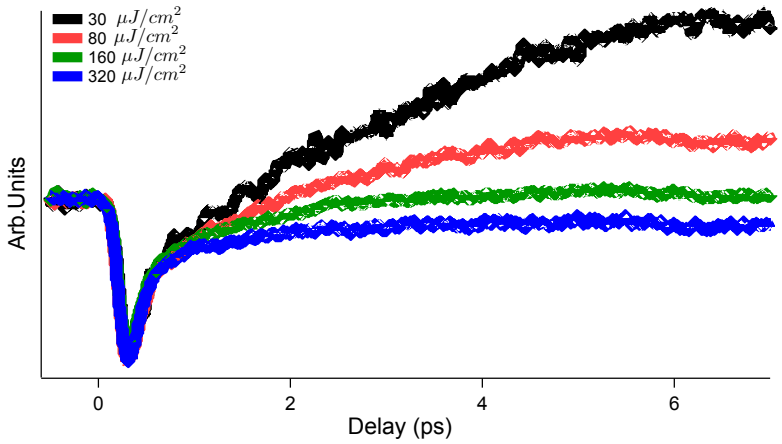

Figure 5.3: The time-resolved reflectivity traces on Na_2IrO_3 at four different pump fluences are reported. Both the pump and the probe are set to $\omega = 1.55$ eV

ferent behaviour in the slower dynamic as function of pump fluence can be attributed either to single energy pulse effect or to average heating that changes the sample temperature. In order to answer this question, we studied Δ R/R(τ) at T$=$ 10 K as a function of pump fluence at two different pulses repetition rate: 543 KHz and 181 KHz. The 2D plot of figure 5.4 and figure 5.5 describes ΔR/R as a function of pump fluence at two different pulse repetition rate. The color scale represents the amplitude of the reflectivity variation, ΔR/R(τ, F). In panels b) of figure 5.4 and 5.5 two ΔR/R traces at two different pump fluences are described: the black trace is taken at 25 μJ/cm^2 while the red one is taken at 52 μJ/cm^2. Comparing these results we can conclude that the different ΔR/R(τ) in figure 5.4 is because of the higher repetition rate, and so the average heating, than repetition rate of figure 5.5.

In the panel c) of figure 5.4 we report an intensity plot of ΔR/R at fixed delay time, $\tau = 6$ ps. The amplitude of the positive component progressively decreases as the average heating is increased. This analysis of the measurements as a function of the pump fluence demonstrates that different slower dynamics are due to different temperatures of the sample that is caused by the average heating.

In order to clarify the temperature dependence of the photoinduced relaxation dynamics, we performed detailed measurements in the vicinity of T_N, as reported in figure 5.6

The measurements have been performed a fixed pump fluence of 15 μJ/cm^2. As shown In figure 5.6, the dynamics of the ΔR/R(τ) signal remains almost constant down to a temperature of about 60 K, below which the positive and slow component starts to develop. In order to quantitatively analyse the temperature-dependent signal, the

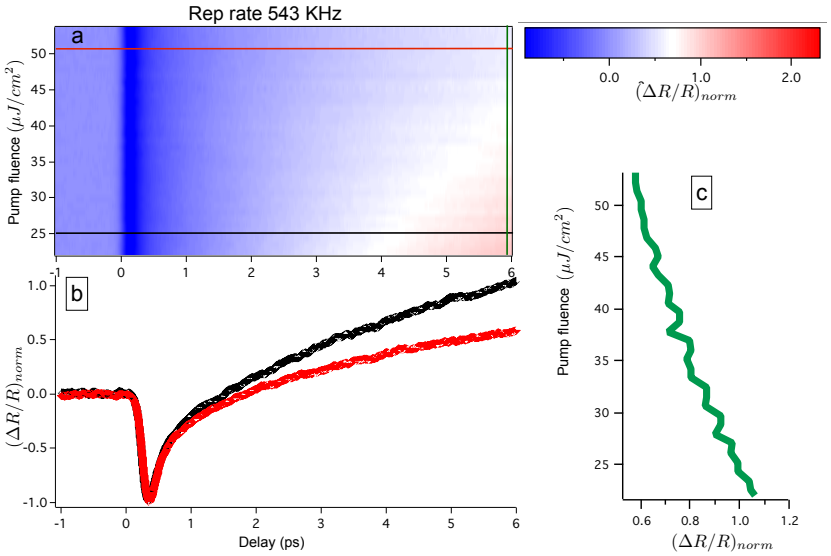

Figure 5.4: Time-resolved reflectivity on Na_2IrO_3. **[a]**The 2D plot are Time-resolved reflectivity for different pump fluences when the sample is at T= 10 K and the repetition rate of laser pulses is 543 KHz. In **[b]** two temporal cut in 2D at $25\mu J/cm^2$ (black) and $51\mu J/cm^2$ (red). In **[c]** a fluence cut in 2D plot (green line) at fixed delay $\tau = 6$ ps.

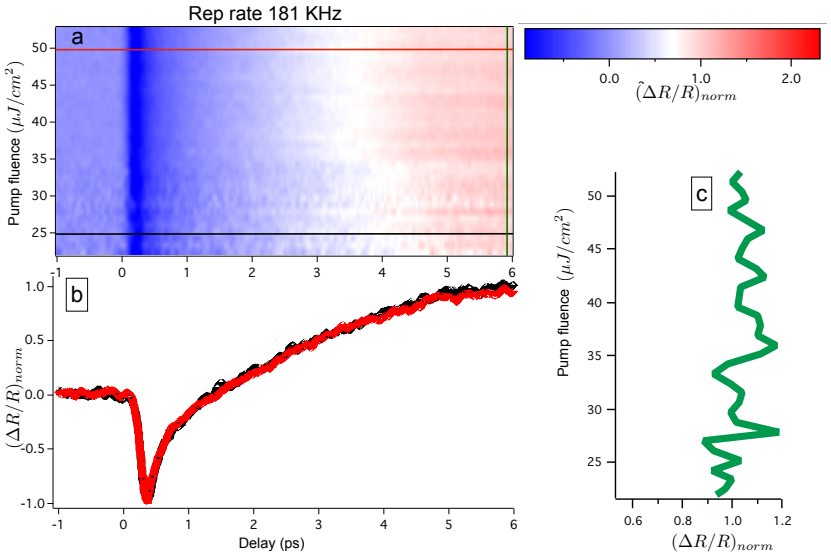

Figure 5.5: Time-resolved reflectivity on Na_2IrO_3. **[a]**The 2D plot are Time-resolved reflectivity for different pump fluences when the sample is at T= 10 K and the repetition rate of laser pulses is 181 KHz. In **[b]** two temporal cut in 2D at $25\mu J/cm^2$ (black) and $51\mu J/cm^2$ (red). In **[c]** a fluence cut in 2D plot (green line) at fixed delay $\tau = 6$ ps.

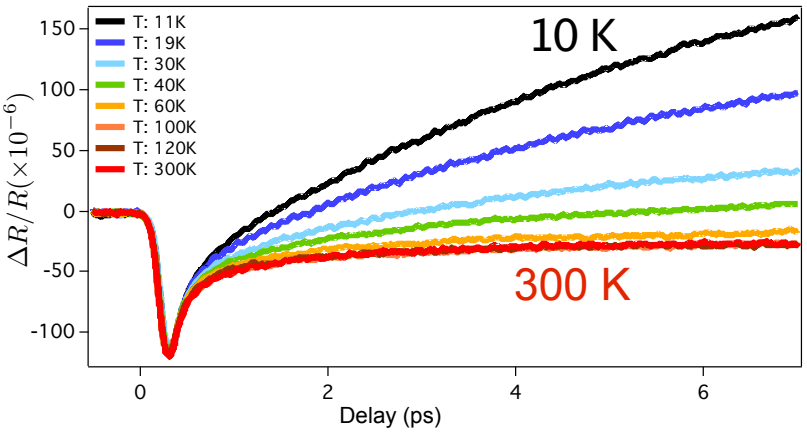

Figure 5.6: Pump-probe reflectivity measurements as a function of temperature. The pump fluence is $15\mu J/cm^2$, at energy 1.55 eV.

function 5.2 has been fitted to the data reported in figure 5.6.

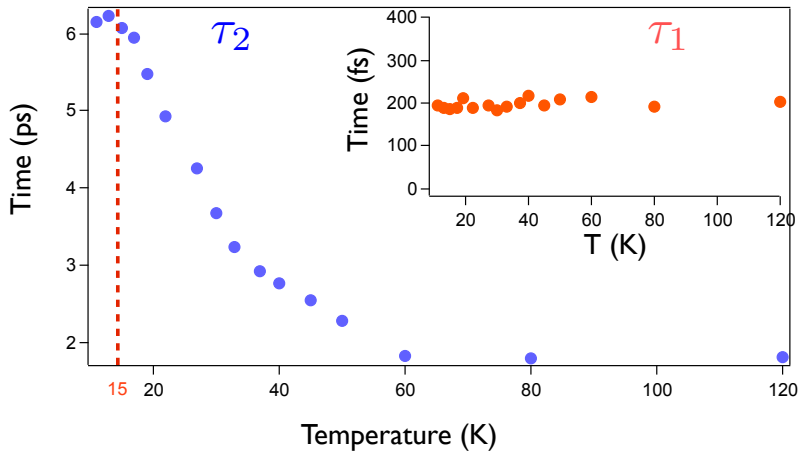

Figure 5.7: The temperature dependence of the τ_2 (blue dots) dynamic obtained by the fit function 5.2. In the inset τ_1 dynamic (red dots) as a function of temperature is reported

Figures 5.7 and 5.8 report the values of the decay times (τ_1 and τ_2) and amplitudes (A_1 and A_1) of the exponential functions as a function of the temperature. While both the amplitude and decay time of the fast dynamics are constant in the entire temperature range, the slow dynamics turns out to be strongly temperature-dependent as T_N is approached. Both the amplitude and decay time tend to diverge at $T \to T_N$. Interestingly, the slow component is detected already at a relatively large temperature, 50 K, which represents a temperature range much larger than the expected width of a conventional second-order phase transition at T_N. This outcome, suggests that the system manifests magnetic correlations well above the onset of long range zig-zag order at T_N. This observation is in

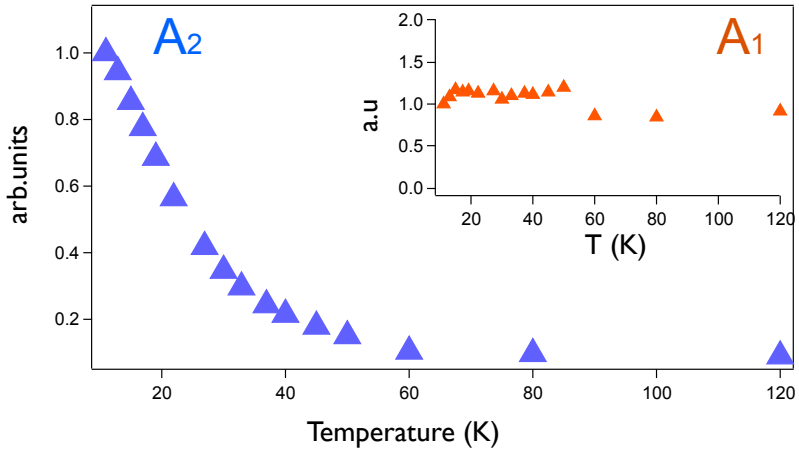

Figure 5.8: The temperature dependence of the A_2 (blue triangles) obtained by the fit function 5.2 and normalized. In the inset A_1 dynamic (red triangles) as a function of temperature is reported

agreement with entropy measurements, which pointed out the high degree of magnetic frustration of the Na_2IrO_3 [Singh., 2010]. More in general, the divergence of the relaxation time in proximity of a phase transition has been reported on other iridates and in many other systems subject to a phase transition [Hinton et al., 2015] [Alpichshev et al., 2015].

5.3 *ASynchronous OPtical Sampling (ASOPS) measurements*

In the previous section we discussed the behaviour of Na_2IrO_3 as a function of temperature and pump fluence. These results showed that approaching $T_N = 15$ K an additional picosecond dynamics, related to the photoinduced quench of the magnetic order, appears in the relaxation process. As discussed in section 5.2 the slow timescale can be attributed to the time needed to quench the local magnetic order, after the impulsive photoinjection of high-energy electron-hole excitations. On a longer timescale, which is out of the explored time window, the system will eventually relax back to the equilibrium state through the cooling via phonons and the thermal bath. In order to investigate the recovery of the equilibrium state, which is expected to happen on the nanosecond timescale, we extended the time window of the previous measurements by adopting a novel Asynchronous Optical Sampling Technique (ASOPS), as introduced in section 4.5. With the ASOPS technique it is possible to study $\Delta R/R(\tau)$ of Na_2IrO_3 with 200 fs time resolution up to 10 ns of time delay maintaining the alignment between pump and probe pulses. The asynchronous optical sampling (ASOPS) technique employs two separate femtosecond mode-loked lasers with different repetition rate

f_1 and f_2 respectively, to generate the pump and the probe pulses. The difference in repetition rate is the source of the optical delay (for details see section 4.5). Compared to the standard pump probe technique (in which the delay between the two pulses is made by a transitional stage), in ASOPS-based measurements the main differences are the different repetition rate of pulses (100 MHz instead of 543 KHz) and the photon energy of the pump pulses (0.78 eV instead of 1.55 eV).

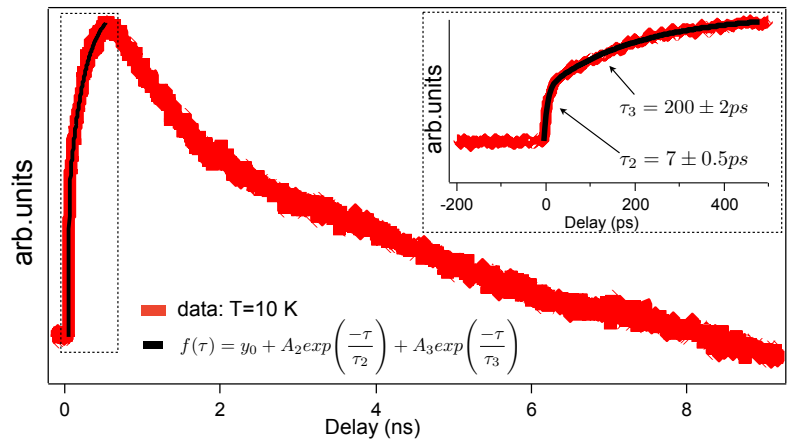

Figure 5.9: The red trace represents a time-resolved optical signal (in reflectivity) measured on Na_2IrO_3 by means of the ASOPS technique. The pump energy is 0.78 eV. The black line trace is the double exponential function 5.2 fitted to the data. This double exponential function is characterized by two relaxation dynamics called $\tau_2 = 7$ ps and $\tau_3 = 200$ ps. The details of the dynamics within the first 200 ps are reported in the inset.

In figure 5.9 we report the reflectivity variation at T= 10 K, as measured by the ASOPS technique. The data reported in figure 5.9 show the complete dynamics, from the initial non-thermal excitation of electron-hole pairs to the cooling down process for $\tau > 1$ ns. Interestingly, the ASOPS measurements demonstrate that the build-up time of the positive signal contains two different dynamics (see inset of figure 5.9). While the first one corresponds to the slow dynamics of ~ 7 ps measured through the conventional technique, the second one represents an additional build-up time dynamics (τ_3) on the 200 ps timescale. Eventually, the system cools down via the energy exchange with the thermal bath and recovers the initial state within 10 ns.

Using the double exponential fit function 5.2 to analyze $\Delta R/R(\tau)$ measurements at different temperatures of figure 5.11 up to $\tau = 4000$ ps , we find that the second dynamics τ_2 is temperature dependent, similarity to what observed in the conventional pump probe measurements discussed in the section 5.2, while the third dynamics show a temperature independent behaviour which we attribute to the further local heating of the area excited by the pump pulse. On a longer timescale (> 1 ns) the system eventually cools down via heat diffusion in the bulk.

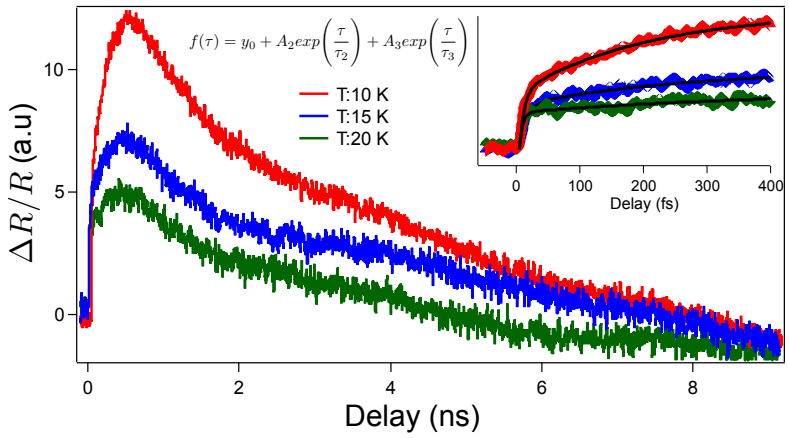

Figure 5.10: Pump-probe reflectivity measurements as a function of temperature performed by ASOPS technique

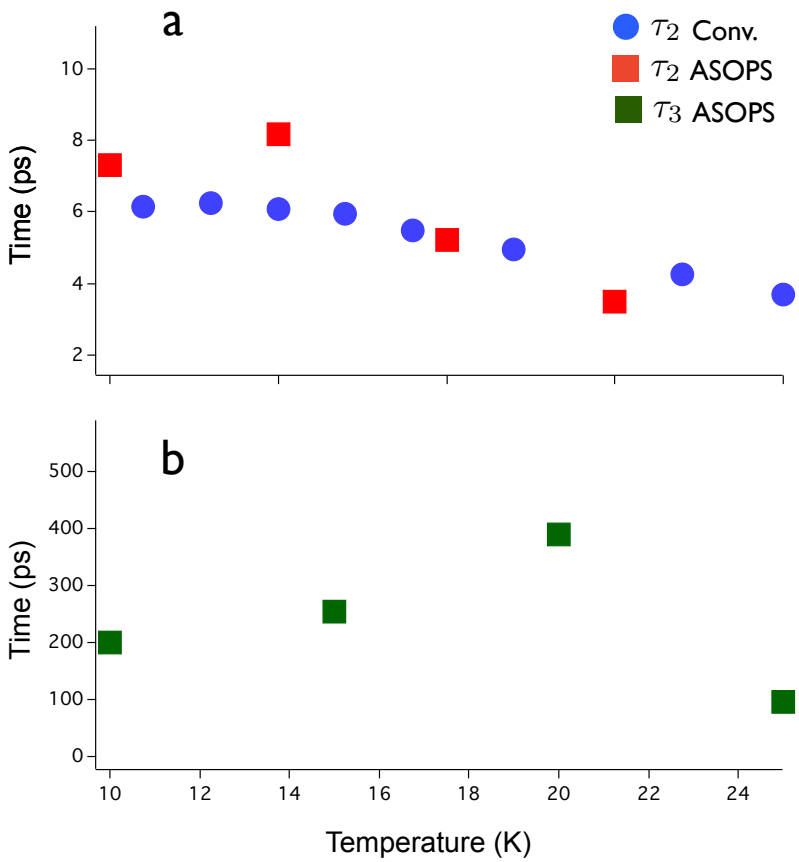

Figure 5.11: **a**) Fit results obtained with ASOPS technique (red squares) regarding the τ_2 dynamics, that is till 10 ps, and these are compared with the fit results obtained with conventional technique (blue dots). **b**) Fit results obtained with ASOPS technique (green squares) regarding the τ_3 dynamics, that is till 400 ps

In addition the ASOPS measurements also suggest that the temperature-dependent reflectivity variation in the vicinity of T_N does not depend on the pump photon energy. we have understood that the different reflectivity behaviour across T_N is not correlated with pump pulse energy.

By combining the conventional pump-probe technique combined with the ASOPS technique reported in this chapter, we were able to perform a comprehensive temperature-dependent study of the reflectivity variation on Na_2IrO_3 at $\omega_{probe} = 1.55$ eV. The results demonstrate that the relaxation dynamics is characterized by four different dynamics, which depend on sample temperature while they are not affected by the change in the pump photon energy (1.55 eV and 0.77 eV). Here I summarize the four different relaxation dynamics of Δ R/R:

- the first temporal dynamic, $\tau_1 = 200$ fs, is independent from the temperature. We attribute it to the relaxation across the Mott gap.
- $\tau_2 = 2 \rightarrow 8$ ps is strongly temperature-dependent and exhibit the tendency to diverge when T_N is approached. This dynamic is related to the perturbation of the magnetic state of the system.
- the third temporal dynamic $\tau_3 \sim 200$ ps is temperature independent and it can attributed to the further demagnetization of the system related to the local heating in the excited area.
- the system recovers its ground state by dissipating the locally accumulated excess energy via heat dissipation in the bulk.

Discussion

The time-resolved measurements on Na_2IrO_3 unveiled a complex dynamics which contains four different typical time scales, that are related to specific excitation/relaxation processes in the system.

- Ultrafast relaxation dynamics (τ_1)

  The pump pulses of 1.55 eV photons excites electrons within the Ir $_{2g}$ manifold and causes electron transition from a $J_{eff} = 3/2$ band into the upper Hubbard band (UHB), as shown in figure 5.12 (see chapter 1 description J_{eff}). This is expressed by a rapid decrease in the reflectivity that thus tracks the cooling of the electrons. The ultrafast relaxation of high-energy electron-hole excitations has been already observed and discussed in both Na_2IrO_3 and Sr_2IrO_4 [Alpichshev et al., 2015] and [Hsieh et al., 2012]. The effective cooling is mediated by electron-electron interactions and by the coupling to optical phonons on the $100 - 200$ fs timescale. At

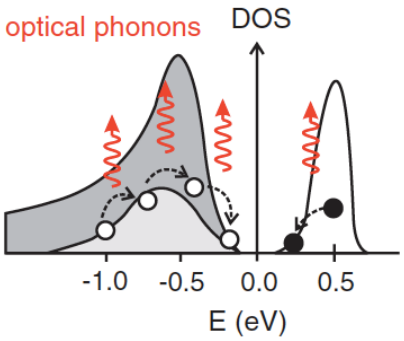

Figure 5.12: Schematic drowning that the initial fast decay process is governed by energy relaxation of photoexcited electrons and holes towards the band edges via optical phonon emission [Hsieh et al., 2012]

the end of this ultrafast process, a non-thermal population of electron-hole excitations remains trapped at the gap edges.

- Coupling to the magnetic state (τ_2)

  After the fast relaxation of e-hole excitations, the electron-hole excitations can recombine across the gap by emitting magnetic excitations that perturb the magnetic background, in both the long-ranged zig-zag magnetic phase and in the highly frustrated state at $T>T_N$ in which magnetic correlations persists even in the absence of long-range magnetic order ([Alpichshev et al., 2015]). Since this relaxation process is mediated by magnetic excitations, it is reasonable that it depends on the magnetic state and, therefore, on the temperature of the system. At low temperatures (AFM regime), these magnetic excitations perturb the system bringing it as close as possible to the disordered phase. In this picture, the small energy of the coherent magnetic excitations (spin waves) ($\sim$ 5 meV [Choi et al., 2012]) as compared to the gap energy of 340 meV, which is the total energy that needs to be dissipated during the recombination process, make the lifetime exponentially large ($\tau_2 = 1 \rightarrow 8$ ps).

- Thermalization and Cooling (τ_3 and τ_4) The production of magnetic excitations and the consequent perturbation of the zig zag phase, take place in a non-thermal regime, in which the distribution of the charge carriers and of the bosonic (magnetic and phononic) excitations cannot be described by simple thermodynamic expressions. On a longer timescale (τ_3 $\sim$200 ps), the energy exchange between the charge excitations and the reservoir constituted by the magnons and phonons will lead to a progressive thermalization at a local effective temperature larger than the equilibrium one.
  Once established a quasi-thermal distribution, the system eventually release all the energy locally stored in the excited area via heat

diffusion towards the bulk. This leads to the slow cooling down, which is described by the fourth dynamics, τ_4 $\sim$10 ns.

The results obtained on Na_2IrO_3 by single-colour pump-probe techniques are in agreement with previous experiments on similar systems. For example, it has been shown in [Alpichshev et al., 2015] and [Li et al., 2015] that, approaching $T_N = 15$ K in Na_2IrO_3 there is a change in both the amplitude and the sign of the reflectivity variation signal. These different Δ R/R variations between the nonmagnetic and the antiferromagnetic states of the system are interpreted by [Alpichshev et al., 2015] and [Li et al., 2015] as a consequence of the photo-demagnetization of the system. As it has been reported by [Li et al., 2015], photo-demagnetization occurs via the local distortion of magnetic order in the neighbourhood of each of the non-equilibrium quasiparticles. According to [Alpichshev et al., 2015], ΔR/R corresponds to a non equilibrium population of unoccupied and occupied sites (see figure 5.12). The positive reflectivity variation at low temperature is attribuited to the binding of these excitations due to the energy cost of deforming the zig-zag magnetic structure.

The entire set of results presented here, along with the outcome of experiments already reported in the literature, suggest that the dynamics probed by the 1.55 eV pulses is directly proportional to the magnetic dynamics of the systems. These findings raise an important issue about the origin of such a signal and the microscopic mechanism that allows to mirror the low-energy physics related to the magnetism ($5 - 10$ meV) in the high-energy optical properties. This issue will be tackled in the next chapter, in which we will report multi-colour transient reflectivity measurements on Na_2IrO_3.

6 Optical spectroscopy out of equilibrium measurements on Na_2IrO_3

6.1 Introduction

In the previous chapter we have described the reflectivity variation on Na_2IrO_3 probed by the 1.55 eV pulses as a function of temperature. We have observed the onset of a specific dynamics in the $\Delta R/R$ signal, which tends to diverge as the T_N is approached, thus suggesting a direct relation with the magnetic state of the system. By means of both conventional and ASOPS pump-probe techniques the time relaxations of the system have been studied in the 100 fs-10 ns time window.

In this chapter we extend the study of the reflectivity variation to a broader energy range ($1.4 - 2.1$ eV) using the white light produced by a photonic fiber seeded by a Ti:sapphire oscillator. Exploiting the spectroscopic information and analysing the experimental results with a the differential dielectric function approach, we demonstrate that our results are well interpreted in the frame of Quasi Molecular Orbital scenario, introduced by [Mazin et al., 2012].

6.2 Optical spectroscopy measurements on Na_2IrO_3

In this section we present a study of time and energy resolved pump probe reflectivity measurements on Na_2IrO_3 at three different temperatures: T=10 K, T=20 K and T=50 K. This kind of measurements provides a spectroscopic information which will be crucial in modelling the origin of the measured reflectivity variation. In order to have a spectroscopic measurements, the ultrashort infrared pulses (with ω_{probe}=1.55 eV i.e λ=780 nm) are focused into a photonic crystal fiber that generates supercontinuum pulses with an energy range of 1.4-2.1 eV. The setup used for this type of measurement is described in chapter 4.

The quantity that we measure with time resolved optical spectroscopy is the transient reflectivity $\Delta R/R$, which includes the probe

energy information ω, i.e $\Delta R/\mathrm{R}\ (\omega, \tau)$, where τ is the pump-probe delay. This quantity is defined as:

$$\Delta R/R(\omega, \tau) = \frac{R_{exc}(\omega, \tau) - R_{eq}(\omega)}{R_{eq}(\omega)} \tag{6.1}$$

where $\mathrm{R}_{eq}(\omega)$ is the static reflectivity and $\mathrm{R}_{exc}(\omega, \tau)$ is the excited reflectivity which depends on pump probe delay τ. In figure 6.1 we report the time and energy resolved reflectivity $\Delta\mathrm{R}/\mathrm{R}(\omega, \tau)$ at three different temperatures, T=10 K (below T_N), T=20 K (above T_N) and T=50 K (above T_N). These measurements are performed by pump pulses of energy $\hbar\omega_{pump}$=1.55 eV and fluence of 40 $\mu\mathrm{J/cm}^2$. The temporal range scanned in the experiments shown in 6.1 is 2 ps. In the central panels of figure 6.1 (panels $\mathbf{b}_1$, $\mathbf{b}_2$, $\mathbf{b}_3$) the 2D plots of $\Delta\mathrm{R}/\mathrm{R}(\omega, \tau)$ at three different temperatures are reported. The colour of these plots indicates the sign of the reflectivity change: red for positive variation, blue for negative variation. Comparing the 2D plots of figure 6.1, we note a dramatic change of the $\Delta\mathrm{R}/\mathrm{R}$ signal when the temperature is decreased from 50 to 10 K. In particular, the differences are more pronounced at a delay of about 1 ps and in a narrow energy region, extending from 1.5 to 1.7 eV. For each 2D plot we take a time domain trace at $\hbar\omega_{probe}$=1.55 eV (panels $\mathbf{c}_1$, $\mathbf{c}_2$, $\mathbf{c}_3$) and energy-domain traces at fixed $\tau = 1.5$ ps (panels $\mathbf{a}_1$, $\mathbf{a}_2$, $\mathbf{a}_3$) in order to better analyze the time and spectral resolved optical measurements. The time-domain traces at $\hbar\omega_{probe}$=1.55 eV (panels $\mathbf{c}_1$, $\mathbf{c}_2$, $\mathbf{c}_3$) at the three different temperatures, show the same ralaxation dynamics than those observed by single color measurements presented in chapter 5. By inspection of the three energy resolved graphs (panels $\mathbf{a}_1$, $\mathbf{a}_2$, $\mathbf{a}_3$), we can note the different trend of $\Delta\mathrm{R}/\mathrm{R}(\omega)$ as a function of probe energy. In panel $\mathbf{a}_1$, at T= 10 K, we can see a positive increase of ΔR up to 1.7 eV; above this energy the $\Delta R/$ R signal becomes negative up to a photon energy of about 1.8 eV. Finally, in the $1.9 - 2.1$ eV energy range, the signal turns positive and reaches its maximum at about 2.1 eV. This spectrally-localized component of the $\Delta R/\mathrm{R}$ signal is not observed at T= 50 K (panel $\mathbf{a}_3$) in which $\Delta R/\mathrm{R}(\omega)$ presents a negative plateau in the 1.4-1.8 eV energy range for all the time delays.

Thanks to the extended probed energy range (1.4-2.1 eV), it is possible to spectrally characterize the reflectivity variation as a function of temperature.

6.3 *Differential model*

In the section 5.2 we have extensively discussed the different relaxation dynamics of the $\Delta\mathrm{R}/\mathrm{R}$ signal, as measured at 1.55 eV for different temperatures. Using the fit function in 5.2 we observed that

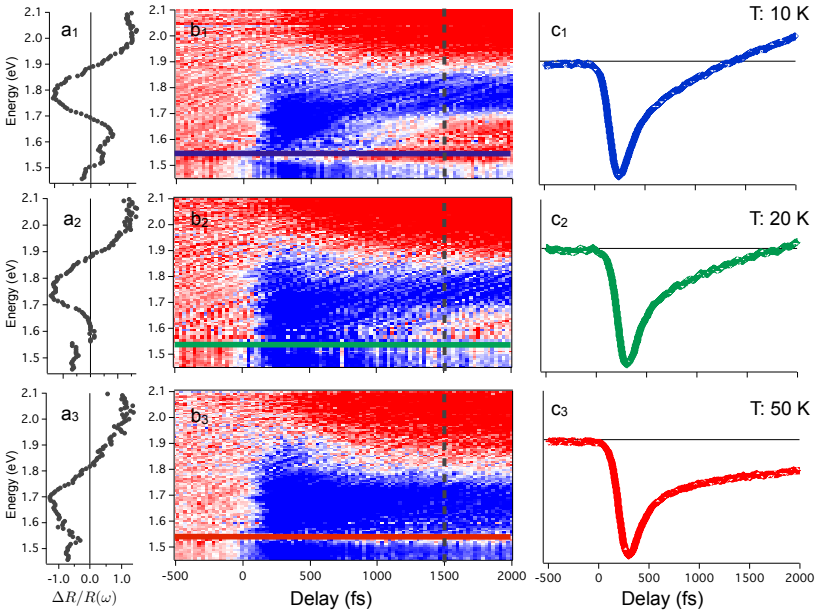

Figure 6.1: The temporally and spectrally resolved plots for reflectivity variation on Na_2IrO_3 at thre different temperatures: T= 10 K,T= 20 K, T= 50 K (panel **b**. The cuts at $\tau = 1.5$ ps pump probe delay are reported in panel **a**, evidencing the spectral structure of transient signal. The temporal cut of 2D plots at probe energy $\omega_{probe} = 1.55$ eV are reported in panel **c** and they are in agreement with measurements performed with single-color probe. (see figure 5.6)

approaching the magnetic phase at T_N=15 K, the second dynamics (τ_2>1 ps) presents a divergence that is attributed to a photoinduced demagnetization ([Alpichshev et al., 2015] and [Hinton et al., 2015]). In this section we introduce a model to quantitatively analyse the transient spectral measured on Na_2IrO_3, called *differential dielectric function* approach. This model allows to establish a precise relationship between the time-resolved optical signal in the energy domain and the pump-induced modification of the equilibrium dielectric function of the system. In order to adopt the differential approach, an essential requirement is that the equilibrium optical properties of Na_2IrO_3 are completely characterized. In chapter 3 we have seen the equilibrium optical properties of Na_2IrO_3 and in particular we have seen how the equilibrium complex dielectric function can be reproduced by a model composed of a sum of Lorentz oscillators, representing the interband transitions that involves the Ir t_{2g} orbitals. This model constitutes the static equilibrium dielectric function ϵ_{eq} (ω,T) and will be the starting point of the differential approach. The quantity that we have measured is described in the formula 6.1 where $R_{eq}(\omega)$ is related to ϵ_{eq} (ω) through the formula 3.1 and $R_{exc}(\omega, \tau)$ is the excited reflectivity which is related to non-equilibrium dielectric function, indicated with ϵ_{exc} (ω, τ). The differential approach consists in using the static dielectric function model equilibrium parameters and to change as few parameters as possible in order to reproduce the $\Delta R/R(\omega)$ signal.

6.3.1 *Differential dielectric function fitting*

In figure 6.2 we present $\Delta R/R(\omega)$ traces at T=10 K represented by blues squares, and T=50 K represented by the red dots. The reflectivity variation signals in figure 6.2 are as a function of probe energy (1.4-2.1 eV) for a fixed delay time of τ=1.5 ps. The blue and red solid lines in figure 6.2 represent the results of the fitting of the differential dielectric function model to the $\Delta R/R(\omega)$.

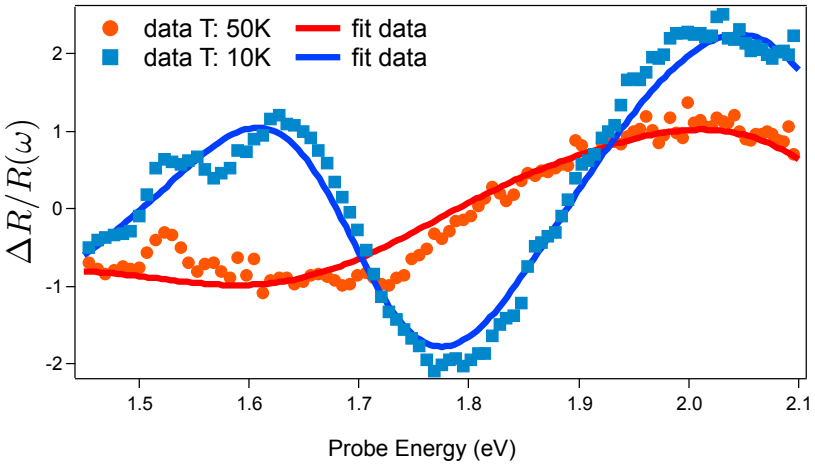

Figure 6.2: $\Delta R/R$ (ω) experimental data at T= 50K (red dots) and T= 10K (blue squares). The pump-probe delay is fixed at $\tau = 1.5$ ps. Solid lines are the fit to the data.

The fits to the data are obtained keeping unchanged the static dielectric function model parameters except for the oscillator parameters centered at 1.66 eV (the D oscillator in figure 3.7 described in section **??**). In particular, the parameters that we have modified from the static model are the following:

- The differential fit of $\Delta R/R$ at T=10 K (blue solid line) is obtained by keeping all the equilibrium parameters fixed, except for the eigenfrequency ω_0 and for the plasma frequency ω_p of D Lorentzian oscillator (see figure 6.3).

- The differential fit of $\Delta R/R$ at T=50 K (red solid line) is obtained by keeping all the equilibrium parameters fixed, except for the plasma frequency ω_p of D Lorentzian oscillator (see figure 6.4).

The differential fits results show that when the system is above T_N, the reflectivity variation respect to the static reflectivity presents a change in spectral weight in the oscillator centered at 1.66 eV. Instead when the system from the normal state phase switches in the antiferromagnetic phase, the oscillator at ω_0=1.66 eV is shifted to lower energies.

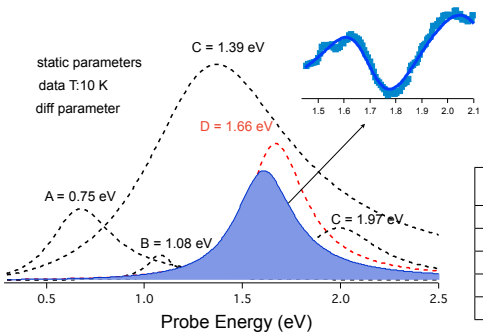

Na_2IrO_3 differential optical parameters T=10K (eV)

	ω_0	ω_p	γ
A	0.75	0.46	0.14
B	1.08	0.36	0.17
C	1.39	2.88	0.99
D	1.65	1.086 (1.097)	0.32
E	1.97	0.77	0.46

Figure 6.3: Lorentz oscillators used in the differential dielectric function model for $\Delta R/R(\omega)$ at T=10 K. The oscillators represented by dashed line are also those used for the static dielectric function model. From this picture we can see that the only variation between static and differential Lorentz oscillators, is the D oscillator plasma frequency plasma frequency (ω_p) and its eigenfrequency (ω_0).

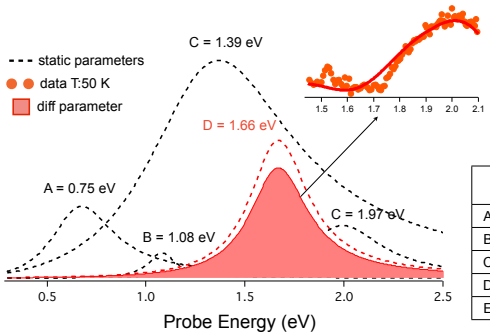

Na_2IrO_3 differential optical parameters T=50K (eV)

	ω_0	ω_p	γ
A	0.75	0.46	0.14
B	1.08	0.36	0.17
C	1.39	2.88	0.99
D	1.66	1.092 (1.097)	0.32
E	1.97	0.77	0.46

Figure 6.4: Schematic drawing of the Lorentz oscillators used in the differential dielectric function model for $\Delta R/R(\omega)$ at T=50 K. The oscillators represented by dashed line are also those used for the static dielectric function model. From this picture we can see that the only variation between static and differential Lorentz oscillators, is the D oscillator plasma frequency plasma frequency (ω_p).

The change in the D oscillator spectral weight in the T=50 K trace is due to the pump-induced thermomodulation effect. The temperature variation modifies the reflectivity of the sample because of a broadening of the occupation of the states near E_F. This modifies the sample absorption, and therefore the reflectivity. The amplitude of the reflectivity change, strongly depends on the probe photon energy [Schoenlein et al., 1987], [Eesley, 1983].

When the system is cooled below T_N, the D oscillator changes spectral weight but also its frequency. While the spectral weight change is observed at any temperature and can be attributed to the thermomodulation effect, the frequency change of the oscillator D reflects a modification of the band structure that is related to the onset of zig-zag order. In section 3.3 ab-initio calculations of the optical conductivity of Na_2IrO_3 (with the inclusion of the spin-orbit interaction and the Coulomb repulsion), the E_{1g} state projected on QMO in figure 3.4 presents a sizeable overlap with the states near E_F . The transition from the normal state to antiferrmomagnetic state implies a change in the linear combinations of the QMOs close to E_F and in conducting states and, as a result of its sizeable overlap, a change of the E_{1g} state as well. On the other hand, the B_1u QMO at

1.5 eV binding energy (see figure 3.4) retains almost its pure nature and its overlap with the states at E_F is very small. As a consequence, it is barely affected by the rearrangements of the states at E_F associated to the onset of zig-zag order. This picture is supported by the fact that no variation of the optical transition E is observed at low temperature.

Thanks to the non-equilibrium approach and the spectroscopic information, we have been able to detect the shift in energy of the E_{1g} state that correspond to the optical transition represented by the D oscillator.

6.4 Discussion

Reconnecting with the relaxation process discussed in the section 5.3, the broadband probe pulse allow us to describe he dynamics of the high-energy (1.5-2.5 eV) electronic properties. From the analysis of the non-equilibrium spectroscopic informations, when the system is in the zig-zag antiferromagnetic state, we can distinguish the following relaxations processes:

- For τ_0<100 fs the λ=800 nm pump pulse photoexcites the system by inducing transitions from the valence band into the conduction band. The excitation process thus creates a highly non-thermal distribution of high-energy (1.5 eV) electron-hole excitations.

- For $\tau_1 \sim$ 200 fs the high-energy electron-hole excitations relax through electron-electron interactions and coupling to optical phonons. This relaxation process leads to the accumulation of electrons (holes) at the bottom (top) of the conduction (valence) band. The effective cooling is mediated by electron-electron interactions and by the coupling to optical phonons.

- For τ_2>1 ps the hot distribution of electrons and holes can recombine by multi-magnon emission, which perturb the magnetic background. This process, that involves energy of the order of several meV, can be detected in an energy scale of the order of eV thanks to QMO picture. The E_{1g} state, with binding energy of 1 eV, is affected by the perturbation of the magnetic order since it has a sizeable overlap with the conducting states. On the other hand, the B_{1u} state, centered at binding energy of 1.5 eV and isolated from the other states, is not affected by the perturbation of the magnetic order.

6.5 Conclusion

With the combined spectral and temporal resolution we have demonstrated that the quasi-molecular orbital picture introduced by [Mazin et al., 2012] to describe the Na_2IrO_3 electronic properties. The time and energy-resolved reflectivity variation measured at three different temperatures have been reported in this chapter. Thanks to the spectral resolution we have seen the different transient optical response of Na_2IrO_3 in a spectral range among 1.4 eV and 2.1 eV, when the system is in a antiferromagnetic (below T_N=15 K) and in normal state (above T_N=15 K). We have seen that the antiferromagnetic transition leads to a positive reflectivity variation in a certain spectral range (1.5-1.7 eV) on a timescale of several picoseconds. This dynamic is related to the demagnetization process and is connected to eV energy scales thanks to the quasi-molecular orbital (QMO) scenario [Mazin et al., 2012], discussed in section2.7 and in section 3.3. DFT calculations, in which spin-orbit interaction and Coulomb repulsion are included, [Li et al., 2015], support the description of the optical properties in terms of QMOs description. One specific QMO (E_{1g} state), despite having a binding energy centered at 1 eV, has a sizeable overlap with the state close to E_F. This overlap makes it possible to detect the demagnetization process pump-induced when the system is in the antiferromagnetic zig-zag transition (5-10 meV) also at optical energy range.

7 Time-domain THz spectroscopy on $\alpha - CaCr_2O_4$

In this chapter we discuss the characterisation of THz time-domain spectroscopy (THz-TDS) setup, described in section 4.7.4. After introducing the main THz spectroscopy studies on a different kinds of materials, we present the crystal structure and the main physical properties of a frustrated triangular magnet $\alpha - CaCr_2O_4$. This system reveal an interesting features in THz-frequency range, when his temperature drops below T_N=43 K. In order to characterize the setup, we present the THz signal acquired in standard atmospheric environment and the signal in a N_2 environment an we will calculate the size of the THz beam focus through knife edge method. Finally we discuss the THz-TDS on $\alpha - CaCr_2O_4$ an we will discuss of the results obtained.

7.1 Terahertz spectroscopy

In the section 4.7.4 we have seen the hallmarks of the THz radiation. One THz corresponds to a photon energy of about 4 meV. As a result, measurement of the THz electromagnetic response in the $\approx$ 0.1-50 THz range yields insight into a particularly relevant spectrum of excitations in complex materials [Basov and Timusk, 2005]. These include, for example, the conductivity of itinerant charges, plasmons, and polarons, as well as transitions across internal exciton states, quantized levels of nano-confined carriers, superconducting gaps and different spin excitations. In particular in antiferromagnetic materials the resonance occurs at THz frequencies and a lot of measurements on antiferromagnetic crystals such as NiO, MnO [Sievers III and Tinkham, 1963a], NiF,MnF_2 [Sievers III and Tinkham, 1963b] [Richards, 1963], $CoCl_2$ $FeCl_2$ [Jacobs et al., 1965]. The ability to perform pulsed time dependent measurements and record phase information by coherent detection has made THz spectroscopy a important tool for time dependent magnetic studies [Song et al., 2013] [Yoshikiyo et al., 2014]. Furthermore, THz spectroscopy is also an important comple-

mentary technique to inelastic neutron scattering measurements, that is the higher standard technique for measuring the spin-wave dispersion across the Brillouin zone and magnetic excitations [Matsuda et al., 2012]. The sensitivity of polarised neutrons to chiral symmetry in spin lattice ordering has assisted THz investigations in identifying novel excitations associated with atomic vibrations, that are both and magnetically active [Chaix et al., 2013]. In figure 7.1 polarised THz spectroscopy is used to identify electrically and magnetically active excitations based on the orientation of the THz field relative to the crystallographic axes. The dispersion of the excitations is measured by complementary inelastic neutron scattering.

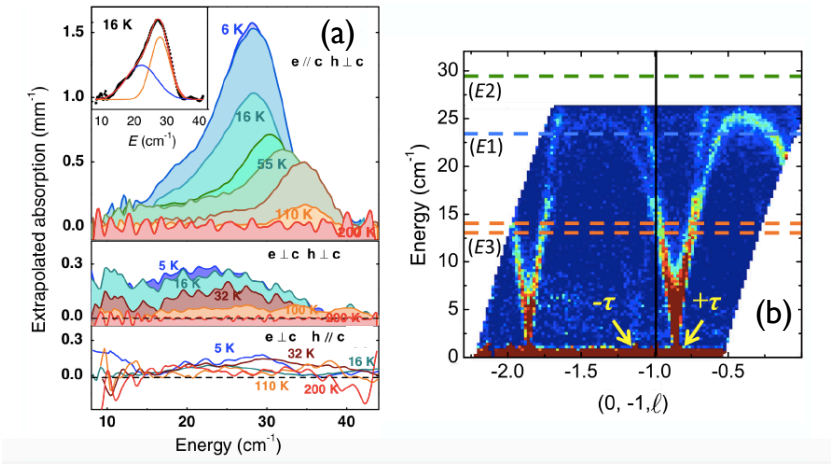

Figure 7.1: **a** THz spectroscopy and **b** inelastic neutron scattering measurements in the analysis of electromagneto spin waves in $Ba_3NbFe_3Si_2O_{14}$ performed by Chaix et.al [Chaix et al., 2013].

Relevant important are the studies on magnetodielectric materials that are characterized by a strong coupling of magnetic and dielectric properties and as a consequence different spin excitations. One of these are the electromagnon [Pimenov et al., 2006] that is an elementary excitation of the magnetoelectric interaction induced by the electric field and characterized by a spin resonance in the THz frequencies [Pimenov et al., 2008].

7.2 *Crystal structure and physical properties of* $\alpha - CaCr_2O_4$

Geometrical frustration is an important feature in magnetism, where it stems from the relative arrangement of spins. A typical characteristic of magnetically frustrated systems is the lack of long-range magnetic behaviour order down to temperatures far below the energy scale of the exchange interactions. Instead of adopting a unique magnetic ground state a low temperatures, a magnetically frustrated system typically remains unordered, because its desired ground state

in non-existent within the given lattice geometry [Ramirez et al., 2001]. This ground state can be highly degenerate leading to exotic physical states like spin liquid behaviour. The simplest frustrated system is the triangular lattice antiferromagnet where all magnetic interactions between nearest neighbours are equal.

$\alpha-CaCr_2O_4$ is a distorted triangular lattice antiferromagnet. The triangular layers of Cr^{3+} ions are only slightly distorted with four different nearest neighbour distances. They build up two zig-zag and two chain patterns running along the *c*-axis. This special distortion and competing next nearest neighbour interactions makes $\alpha-CaCr_2O_4$ a good compound for studying frustration effects on the physics of an antiferromagnet. The magnetic Cr^{3+} ions lie in an octahedral environment and are characterized by a half-filled t_{2g} shell giving rise to spin 3/2 and quenched orbital angular momentum which ensure that the magnetic interactions are isotropic . They

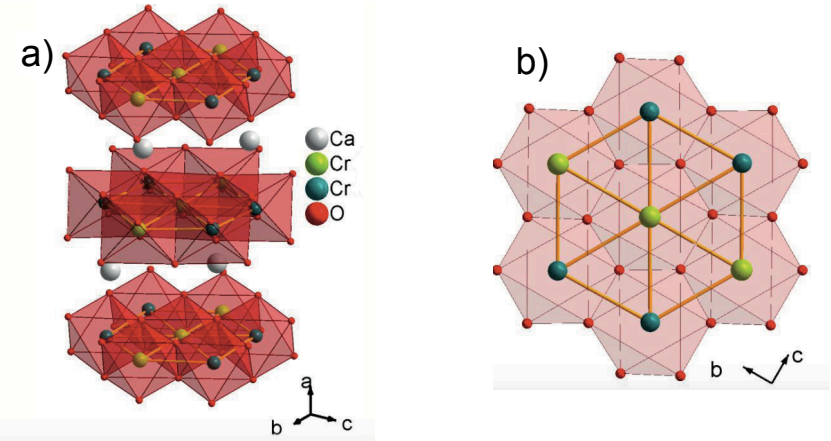

Figure 7.2: **a** Crystal structure of $\alpha-CaCr_2O_4$. In **b** the respective triangular plane [Schmidt et al., 2013].

form distorted triangular layers stacked along the *a* axis, with two layers and eight magnetic ions per unit cell. In figure 7.2 the crystal structure of $\alpha-CaCr_2O_4$ and its respective triangular plane are represented.

There are four slightly different nearest neighbour Cr^{3+} in-plane distances, which are organized into zig-zag and chain patterns. The magnetic structure was determined by utilizing neutron powder diffraction [Toth et al., 2011], single crystal diffraction and spherical polarimetry [Chapon et al., 2011]. With a Curie-Weiss temperature of θ_{CW}=−564 K and a Néel temperature of T_N =42.3 K the system is clearly geometrically frustrated and exhibits a planar 120° spin structure in the crystallographic in the *ac* plane. A optical transmission spectroscopy on $\alpha-CaCr_2O_4$ in the near-infrared to visible-light frequency range was performed by Schmidt et.al [Schmidt et al.,

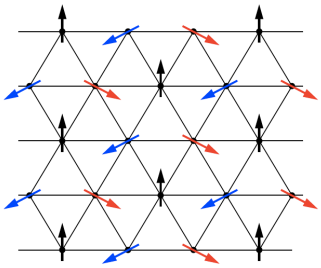

Figure 7.3: Coplanar 120° spin structure of the Heisenberg triangular-lattice antiferromagnet [Mourigal et al., 2013].

2013]. In figure 7.4 Schmidt et.al present the absorption spectra

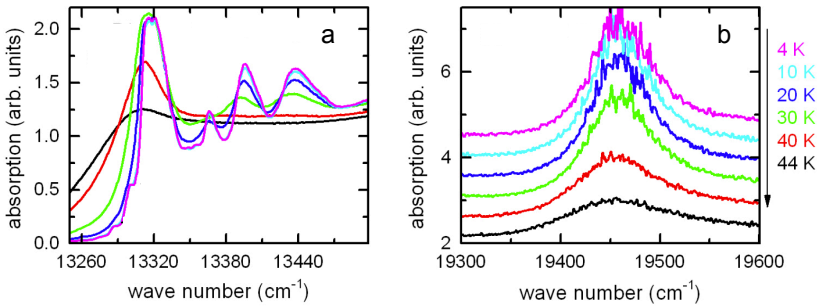

Figure 7.4: Panels **a** and **b** show the absorption spectra for various temperatures in the different frequency range in the E$\|$ c condition. Measurement was done by M. Schmidt et.al [Schmidt et al., 2013]

of $\alpha-CaCr_2O_4$ in the magnetically ordered phase at different temperatures in the frequency region of the $^4A^2 \rightarrow {}^2E$ and $^4A^2 \rightarrow {}^2T_1$ crystal-field excitations which depend on the polarization of the light with respect to the crystallographic axis in the investigated plane, for the electric field of the incoming light polarized parallel to the crystallographic c (E$\|$ c). This study reveals that the fine structure is much more intense E$\|$ c configuration than in E$\|$ b, which points toward a corresponding selection rule.

7.3 *Time-domain THz spectroscopy measurements in air and nitrogen environment*

In this section we present and discuss the THz measurements performed in atmospheric and controlled environment. These measurements are performed with the setup discussed in section 4.7.4.

Both for the generation that for the detection (described in sections 4.7.2 and 4.7.3), we use the ZnTe nonlinear crystal which through the 800 nm ultrashort laser pulse produces a ultrashort THz pulse with a useful bandwidth in the range of 0.3-2.8 THz, In the figure 7.5 we present the THz pulse (panel **a**) and its Fourier transform (panel **b**) after free propagation in air. By inspection of the THz spectra we can observe several peaks, that are caused by absorption and re-radiation from molecules in air, in which water vapour is the predominant process.

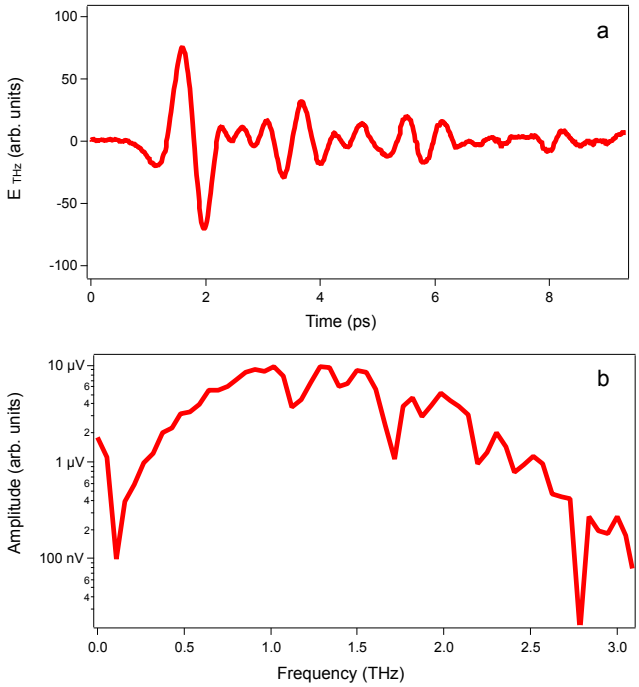

Figure 7.5: Electric field $E_{THz}(t)$ of the THz waveform in atmospheric environment (panel **a**) and its Fourier transform (**b**).

Comparing the water vapour transmission spectrum [Yun-Shik, 2008] with our THz spectrum (see figure 7.6) we can see several peaks in THz spectrum corresponding to different lines of water vapour absorption spectrum [Xin et al., 2006]. The most intense and large peak includes the two higher peaks of water absorption spectrum at 1.66 and 1.72 THz other three small peaks at 1.6, 1.76 and 1.8 THz.

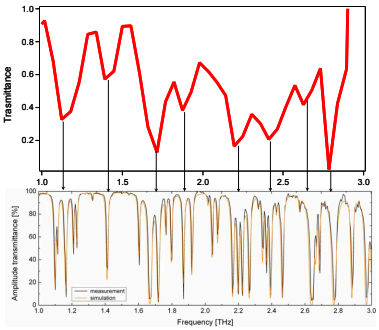

Figure 7.6: Comparison of transmittance spectra obtained by our measurement and transmittance that we have found in the literature [Xin et al., 2006] .

In order to create a water vapour free environment along the THz beam path, necessary to get a clean spectrum, we encompass the THz path with a plexiglass box wherein the pure N_2 gas is fluxed.

In figure 7.7 we present the THz pulse and its Fourier transform measured in a N_2-saturated environment. As we can see, the N_2 spectrum is significantly cleaner than air spectrum. A closer look at the N_2 spectrum reveals that a peak centered at 1.6 THz still remains. This can be attributed to the absorption from phonon difference modes in ZnTe crystal, as reported in literature Chen et al. (2001) see inset in figure .

The THz pulse is focused on the sample by a 15 cm focal length off-axis parabolic mirror. In order to determine THz beam focus we used the Knife-edge technique: a set of measurements of the normalized transmitted power of the THz pulse as a function of the knife-edge position are record through a photodiode coupled

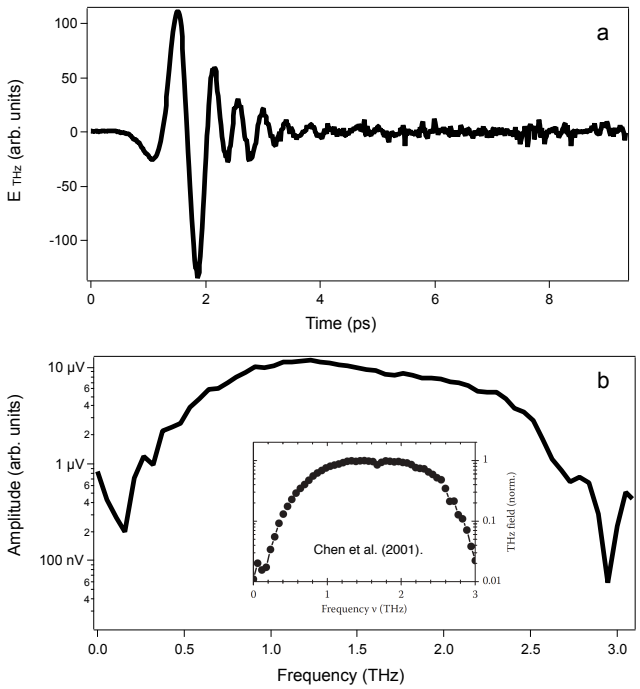

Figure 7.7: Electric field $E_{THz}(t)$ of the THz waveform in N_2-saturated environment (panel **a**) and its Fourier transform (**b**).

to lock-in amplifier. The lock-in amplifier records the integral of the gaussian THz beam up to the position of the knife edge. In the figure 7.8 we present the normalized beam profiling data. By fitting the distribution function to the data we determine the standard deviation σ and hence the full width at half maximum (FWHM) of the THz pulse using the formula .

$$FWHM = 2\sqrt{2\ln 2} \cdot \sigma \tag{7.1}$$

Finally we determine the THz beam focus to be in the order of 1100 μm.

7.4 *Time-domain THz spectroscopy measurements on $\alpha-CaCr_2O_4$*

In the section 7.2 we have seen the study of optical transmission spectroscopy on $\alpha-CaCr_2O_4$ in the near-infrared to visible-light frequency range done by Schmidt et.al [Schmidt et al., 2013]. In this section we want to perform time-domain THz spectroscopy (THz-TDS) measurements on $\alpha-CaCr_2O_4$ at different temperatures in order to characterise the system in low-frequency domain.

For these kind of measurements the $\alpha-CaCr_2O_4$ c axis is oriented in plane of the THz electric field, i.e E$\parallel c$. In the panel **a** and in panel **b** of the figure 7.9 we present the THz electric pulses in time and frequency domain transmitted through $\alpha-CaCr_2O_4$ at various tem-

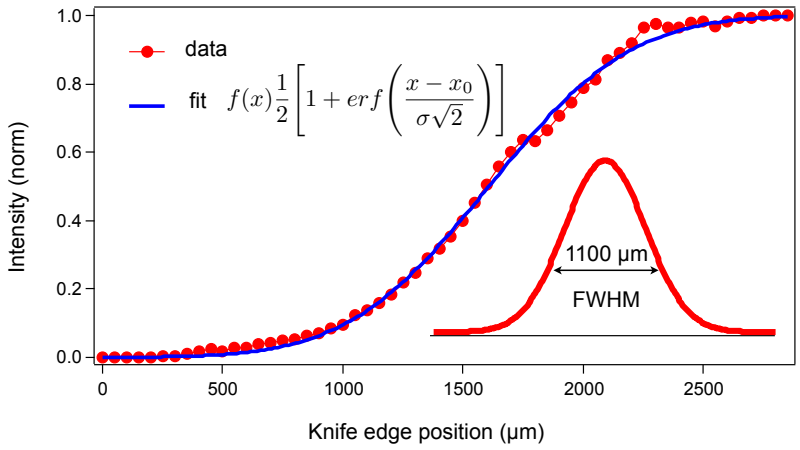

Figure 7.8: Knife-edge scan of the THz pulse focus

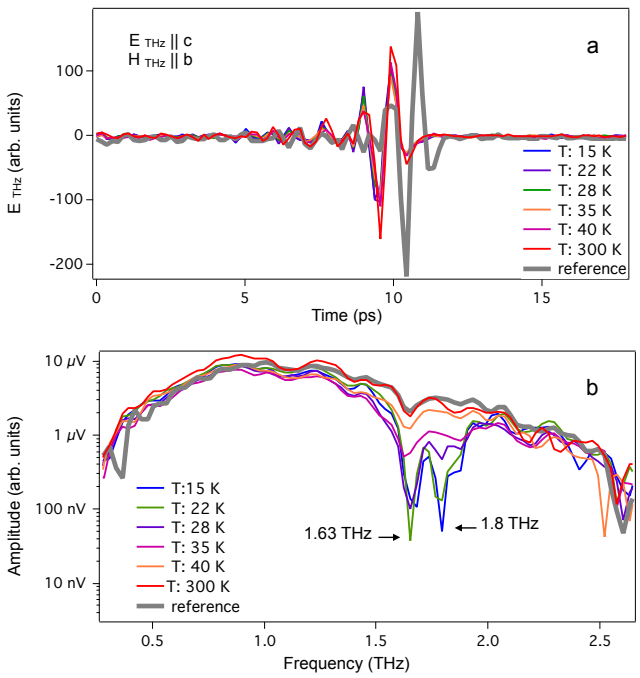

Figure 7.9: **a**: Comparison of electric field $E_{THz}(t)$ of the THz waveform transmitted through the $\alpha-CaCr_2O_4$ at different temperatures and reference E_{THz} waveform. **b**: Comparison of $\alpha-CaCr_2O_4$ and reference spectra.

peratures, in a free-water-vapour condition. The reference signal, i.e the THz pulse and spectra measured without sample, is represented in the panel **a** and **b** of the figure 7.9 by the grey line. By inspection of the frequency-domain measurements we can observe that at room temperature the sample frequency spectra is the same as reference spectra, with a small absorption peak centered at 1.6 THz due to ZnTe phonon mode. This means that at room temperature $\alpha-CaCr_2O_4$ is completely transparent to the THz pulse. When the sample is cooled down, we can observe an absorption peak at 1.63 THz (6.75 meV) just below the T_N K of the system. By lowering the temperature, the THz measurements reveals that this mode splits into two modes around T=28 K. The first mode, at 1.63 THz, exhibits a local maximum around T=22 K while the second has a local maximum centered at 1.8 THz at T=15 K. In figure 7.10 we present the $\alpha-CaCr_2O_4$ frequency-domain absorbance at different temperatures.

The THz spectra measured at various temperatures from 300 K to

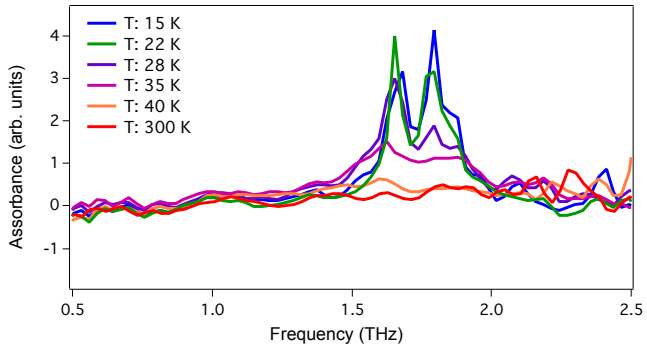

Figure 7.10: Temperature evolution of absorbance spectra of of $\alpha-CaCr_2O_4$.

15 K reveal an absorption peak at 1.65 THz that arises at 35 K and an additional peak at 1.8 THz that arises at 28 K, when the THz electric field is parallel to *c*-axis of the crystal. These excitations, that taking place under T_N, may be attributed both electric and magnetic ordering properties of the system. Magnetoelectric (ME) coupling creates a new quasiparticle excitation at THz frequencies, the electromagnon, and this new class of excitations has been observed in several orthorhombic manganites $TbMnO_3$, $GdMnO_3$ [Pimenov et al., 2006], $DyMnO_3$ [Kida et al., 2008], $TbMn_2O_5$, YMn_2O_5 [Sushkov et al., 2007], $Ba_2Mg_2Fe_{12}O_{22}$ [Kida et al., 2009] and in $BiFeO_3$ [Cazayous et al., 2008].

7.5 Conclusion

In this chapter the we have discussed the characterisation of THz time-domain spectroscopy (THz TDS) setup and we have performed

a preliminary spectroscopic measurements on frustrated triangular magnet system .

For the generation and the detection of the THz pulses we employed the optical rectification process and electro-optic effect, described in section 4.7.2 and in section 4.7.3. The electro-optic process allows the direct measurement of the THz electric field which implies a considerable advantage as compared to conventional spectroscopy, since information about the amplitude and the phase of the electric field can be simultaneously retrieved. From the free propagation of the THz pulse, we have measured the absorption spectrum, in THz region, of the air. In particular we have seen how the water vapour in the air can absorbs most of THz spectrum and how remedy this shortcoming by isolating the THz path in a free-water vapour environment. The THz beam focus was calculated, through the knife edge method. Finally, THz time-domain measurements were performed on a frustrated triangular magnet $\alpha-CaCr_2O_4$. The system turns out to be completely transparent to electric radiation in the range of 0.3-2.8 THz (1.3-12 meV) at room temperature. When the system is cooled below T_N up to T=15 K, a couple of structures are observed: a first absorption peak centered at 1.63 THz (6.75 meV) starting to raise at 35 K while at 28 K a second peak centered at 1.8 THz (7.5 meV) was detected. In according with the other literature results, these two modes are due to the rotational mode of the spiral spin plane that becomes active when Thz electric field is set parallel to to *c*-axis of the crystal.

An additional improvement of this setup will be the introduction of a optical pump pulse in order to to perform optical pump-THz probe measurements at low temperature. Optical-pump THz-probe experiments determine transient changes of the THz dielectric response. THz probes provide the necessary spectral selectivity in ultrafast studies to resonantly reveal optical coherences, transient correlations and phase transitions, or relaxation processes with meV-scale signatures. In cuprate superconductors, manganites, and other correlated materials ultrafast THz studies can discern basic interactions and phase transitions via thermally inaccessible perturbations of the correlated ground state ([Kaindl et al., 2005]; [Averitt et al., 2001]; [Demsar et al., 2003b]; [Prasankumar et al., 2005]).

8 Conclusions

The main work in this thesis has been the study of out-of-equilibrium physics of honeycomb lattice iridates Na_2IrO_3. Thanks to the pump-probe technique, the reflectivity variation as a function of delay time between the pump pulse (1.55 eV, 800 nm) and the probe pulse were performed, in the nonmagnetic and antiferromagnetic state of the system. In addition, a spectroscopic study of the system was made using a microstructure optical fiber seeded by the output of a Ti:Sapphire laser to generate supercontinuum spectrum in the energy range 1.4-2.2 eV. The results we have achieved are the following:

Single-color pump probe measurements The time-resolved differential reflectivity $\Delta R/R$ signals are obtained through ultrashort pulses with temporal length of $\sim$ 100 fs, and photon energy of $\hbar\omega$=1.55 eV. The time resolution is in the order of the pulse length while the temporal window is in the order of 7 ps. The measurements were performed at various temperature, above and below the T_N=15 K, and all of them were characterised by two dynamics. The first one, τ_1=200 fs didn't show any temperature-dependence. The second one, instead, showed a heavy temperature-dependence and the time scale of this variation increase from about 2 ps at 50 K to 6 ps at 12 K.
These type of measurements didn't describe all the relaxation dynamics because the time window of 7 ps is too short. We have therefore completed the relaxation dynamics through Asynchronous Optical Sampling (ASOPS) Technique, where the time resolution was in the order of $\sim$ 200 fs and the time window was in the order od 10 ns. Thanks to this technique we were able to describe the entire reflectivity variation relaxation dynamics on Na_2IrO_3 at various temperatures. These dynamics are in agreement with the literature results [Alpichshev et al., 2015] and [Hinton et al., 2015], and they can be explained as:

τ_1 : after that the pump photoinduce photoelectrons in the conduction band and a photoholes in the valence band, there is a decreasing of reflectivity variation and the system is cooled by

electron-electron and the electron-phonon coupling.

τ_2 :the electron-hole excitations can recombine across the gap by emitting magnetic excitations that perturbs the magnetic background. The time scale necessary to perturb the system, bringing it to the disordered state, is much longer when the system is at low temperatures.

τ_3 : the energy exchange between the charge excitations and the reservoir constituted by the magnons and phonos will lead to thermalization at a local effective temperature.

τ_4 : the system release all the energy locally stored in the excited area via heat diffusion towards the bulk.

These time-domain measurements are interpreted as a consequence of the photo-demagnetization and revealed the validity of J_{eff} model, where the spin-orbit coupling splits the t_{2g} levels of Ir in two main bands: the lower energy band J_{eff}=3/2 and the higher energy band J_{eff}=1/2, opening the gap across the Fermi level.

Single-color pump supercontinuum-probe measurements : By adding the spectral information on the time-resolved measurements we were able to understand the reason why we see a divergence in the $\Delta R/R$ signal, when the system is in the magnetic phase, at the photon-energy $\hbar\omega$=1.55 eV thousand times greater than magnetic energies. By comparing the differential fitting in out-equilibrium with the fitting results in equilibrium condition, five transitions are necessary to reproduce the experimental results. These number of Lorentz peaks are well in agreement with the band structure calculated by Foyevtsova.et.al [Li et al., 2015] where the quasi-molecular orbital (QMO) scenario was adopted. The out of equilibrium spectroscopy on Na_2IrO_3 showed the presence of these fine structure. In particular, when the zigzag antiferromagnetic phase of the system is destroyed by the pump pulse, we see a redshift of a specific QMO centered at binding energy of 1 eV, since it has a sizeable overlap with the conducting states. On the other hand, the QMO centered at binding energy of 1 eV and isolated from the other states, is not affected by the perturbation of the magnetic order.

In conclusion, from the time and energy resolved pump-probe technique we have observed that in Na_2IrO_3 both scenarios J_{eff} and QMO are realized, but in different energy scales. J_{eff} scenario is realized close to the Fermi level and it is necessary to explain the relaxation dynamics in the time resolved pump-probe measurements. QMO scenario is realized in the deeper valence bands, and it is nec-

essary to explain the energy scales where a divergence in reflectivity variation is measured as T_N is approached.

Bibliography

Zhanybek Alpichshev, Fahad Mahmood, Gang Cao, and Nuh Gedik. Confinement-deconfinement transition as an indication of spin-liquid-type behavior in na_2iro_3. *Phys. Rev. Lett.*, 114:017203, Jan 2015. DOI: 10.1103/PhysRevLett.114.017203. URL http://link.aps.org/doi/10.1103/PhysRevLett.114.017203.

B Andlauer, J Schneider, and W Tolksdorf. Optical absorption, fluorescence, and electron spin resonance of ir4+ on octahedral sites in y3ga5012. *physica status solidi (b)*, 73(2):533–540, 1976.

E Antonides, EC Janse, and GA Sawatzky. Lmm auger spectra of cu, zn, ga, and ge. i. transition probabilities, term splittings, and effective coulomb interaction. *Physical Review B*, 15(4):1669, 1977.

Neil W Ashcroft and N David Mermin. *Solid State Physics (Holt, Rinehart and Winston, New York, 1976)*. 2005.

D. H. Auston, K. P. Cheung, and P. R. Smith. Picosecond photoconducting hertzian dipoles. *Applied Physics Letters*, 45(3):284–286, 1984.

Richard D Averitt, AI Lobad, C Kwon, SA Trugman, VK Thorsmølle, and AJ Taylor. Ultrafast conductivity dynamics in colossal magnetoresistance manganites. *Physical review letters*, 87(1):017401, 2001.

DN Basov and T Timusk. Electrodynamics of high-t c superconductors. *Reviews of modern physics*, 77(2):721, 2005.

E. Beaurepaire, J.-C. Merle, A. Daunois, and J.-Y. Bigot. Ultrafast spin dynamics in ferromagnetic nickel. *Phys. Rev. Lett.*, 76:4250–4253, May 1996. DOI: 10.1103/PhysRevLett.76.4250. URL http://link.aps.org/doi/10.1103/PhysRevLett.76.4250.

KW Blazey and F Levy. Epr of rhodium, osmium and iridium-doped rutile. *Solid state communications*, 59(6):335–338, 1986.

Kieron Burke and Lucas O Wagner. Dft in a nutshell. *International Journal of Quantum Chemistry*, 113(2):96–101, 2013.

G. Cao, J. Bolivar, S. McCall, J. E. Crow, and R. P. Guertin. Weak ferromagnetism, metal-to-nonmetal transition, and negative differential resistivity in single-crystal sr_2iro_4. *Phys. Rev. B*, 57:R11039–R11042, May 1998. DOI: 10.1103/PhysRevB.57.R11039. URL http://link.aps.org/doi/10.1103/PhysRevB.57.R11039.

A. Cavalleri, Cs. Tóth, C. W. Siders, J. A. Squier, F. Ráksi, P. Forget, and J. C. Kieffer. Femtosecond structural dynamics in vo_2 during an ultrafast solid-solid phase transition. *Phys. Rev. Lett.*, 87:237401, Nov 2001. DOI: 10.1103/PhysRevLett.87.237401. URL http://link.aps.org/doi/10.1103/PhysRevLett.87.237401.

M Cazayous, Y Gallais, A Sacuto, R De Sousa, D Lebeugle, and D Colson. Possible observation of cycloidal electromagnons in bifeo 3. *Physical review letters*, 101(3):037601, 2008.

Laura Chaix, Sophie De Brion, Florence Lévy-Bertrand, Virginie Simonet, Rafik Ballou, Benjamin Canals, Pascal Lejay, Jean-Blaise Brubach, G Creff, Fabrice Willaert, et al. Thz magnetoelectric atomic rotations in the chiral compound ba 3 nbfe 3 si 2 o 14. *Physical review letters*, 110(15):157208, 2013.

Ji říChaloupka, George Jackeli, and Giniyat Khaliullin. Kitaev-heisenberg model on a honeycomb lattice: Possible exotic phases in iridium oxides A_2iro_3. *Phys. Rev. Lett.*, 105:027204, 2010.

Ji říChaloupka, George Jackeli, and Giniyat Khaliullin. Zigzag magnetic order in the iridium oxide na_2iro_3. *Phys. Rev. Lett.*, 110: 097204, 2013.

LC Chapon, P Manuel, F Damay, P Toledano, V Hardy, and C Martin. Helical magnetic state in the distorted triangular lattice of α-cacr 2 o 4. *Physical Review B*, 83(2):024409, 2011.

S. K. Choi, R. Coldea, A. N. Kolmogorov, T. Lancaster, I. I. Mazin, S. J. Blundell, P. G. Radaelli, Yogesh Singh, P. Gegenwart, K. R. Choi, S.-W. Cheong, P. J. Baker, C. Stock, and J. Taylor. Spin waves and revised crystal structure of honeycomb iridate na_2iro_3. *Phys. Rev. Lett.*, 108:127204, 2012.

Shun Lien Chuang, Stefan Schmitt-Rink, Benjamin I. Greene, and Anthony F. J. Saeta, Peter N.and Levi. Optical rectification at semiconductor surfaces. *Phys. Rev. Lett.*, 68:102–105, Jan 1992. DOI: 10.1103/PhysRevLett.68.102. URL http://link.aps.org/doi/10.1103/PhysRevLett.68.102.

Federico Cilento, Claudio Giannetti, Gabriele Ferrini, Stefano Dal Conte, Tommaso Sala, Giacomo Coslovich, Matteo Rini, An-

drea Cavalleri, and Fulvio Parmigiani. Ultrafast insulator-to-metal phase transition as a switch to measure the spectrogram of a supercontinuum light pulse. *Applied Physics Letters*, 96(2): 021102, 2010. DOI: http://dx.doi.org/10.1063/1.3291105. URL http://scitation.aip.org/content/aip/journal/apl/96/2/10.1063/1.3291105.

JP Clancy, N Chen, CY Kim, WF Chen, KW Plumb, BC Jeon, TW Noh, and Young-June Kim. Spin-orbit coupling in iridium-based 5 d compounds probed by x-ray absorption spectroscopy. *Physical Review B*, 86(19):195131, 2012.

R. Comin, G. Levy, B. Ludbrook, Z.-H. Zhu, C. N. Veenstra, J. A. Rosen, Yogesh Singh, P. Gegenwart, D. Stricker, J. N. Hancock, D. van der Marel, I. S. Elfimov, and A. Damascelli. na_2iro_3. *Phys. Rev. Lett.*, 109:266406, 2012.

Elbio Dagotto, Jan Burgy, and Adriana Moreo. Nanoscale phase separation in colossal magnetoresistance materials: lessons for the cuprates? *Solid State Communications*, 126(1):9–22, 2003.

T. Dekorsy, H. Auer, C. Waschke, H. J. Bakker, H. G. Roskos, H. Kurz, V. Wagner, and P. Grosse. Emission of submillimeter electromagnetic waves by coherent phonons. *Phys. Rev. Lett.*, 74:738–741, Jan 1995. DOI: 10.1103/PhysRevLett.74.738. URL http://link.aps.org/doi/10.1103/PhysRevLett.74.738.

J. Demsar, R. D. Averitt, A. J. Taylor, V. V. Kabanov, W. N. Kang, H. J. Kim, E. M. Choi, and S. I. Lee. Pair-breaking and superconducting state recovery dynamics in mgb_2. *Phys. Rev. Lett.*, 91:267002, Dec 2003a. DOI: 10.1103/PhysRevLett.91.267002. URL http://link.aps.org/doi/10.1103/PhysRevLett.91.267002.

J Demsar, RD Averitt, AJ Taylor, VV Kabanov, WN Kang, HJ Kim, EM Choi, and SI Lee. Pair-breaking and superconducting state recovery dynamics in m g b 2. *Physical review letters*, 91(26):267002, 2003b.

John M. Dudley, Goëry Genty, and Stéphane Coen. Supercontinuum generation in photonic crystal fiber. *Rev. Mod. Phys.*, 78:1135–1184, Oct 2006. DOI: 10.1103/RevModPhys.78.1135. URL http://link.aps.org/doi/10.1103/RevModPhys.78.1135.

GL Eesley. Observation of nonequilibrium electron heating in copper. *Physical review letters*, 51(23):2140, 1983.

Johannes Ferber, Yu-Zhong Zhang, Harald O Jeschke, and Roser Valenti. Analysis of spin-density wave conductivity spectra of iron

pnictides in the framework of density functional theory. *Physical Review B*, 82(16):165102, 2010.

Kateryna Foyevtsova, Harald O. Jeschke, I. I. Mazin, D. I. Khomskii, and Roser Valentí. Ab initio. *Phys. Rev. B*, 88:035107, 2013.

S Fujiyama, H Ohsumi, T Komesu, J Matsuno, BJ Kim, M Takata, T Arima, and H Takagi. Two-dimensional heisenberg behavior of j eff= 1/2 isospins in the paramagnetic state of the spin-orbital mott insulator sr 2 iro 4. *Physical review letters*, 108(24):247212, 2012.

G. A. Garrett, T. F. Albrecht, J. F. Whitaker, and R. Merlin. Coherent thz phonons driven by light pulses and the sb problem: What is the mechanism? *Phys. Rev. Lett.*, 77:3661–3664, Oct 1996. DOI: 10.1103/PhysRevLett.77.3661. URL http://link.aps.org/doi/10.1103/PhysRevLett.77.3661.

B.I. Greene, P.N. Saeta, D.R. Dykaar, S. Schmitt-Rink, and Shun Lien Chuang. Far-infrared light generation at semiconductor surfaces and its spectroscopic applications. *Quantum Electronics, IEEE Journal of*, 28 (10):2302–2312, Oct 1992. ISSN 0018-9197. DOI: 10.1109/3.159537.

Hlynur Gretarsson, JP Clancy, X Liu, JP Hill, Emil Bozin, Yogesh Singh, S Manni, P Gegenwart, Jungho Kim, AH Said, et al. Crystal-field splitting and correlation effect on the electronic structure of a 2 iro 3. *Physical review letters*, 110(7):076402, 2013.

Rogier H. M. Groeneveld, Rudolf Sprik, and Ad Lagendijk. Femtosecond spectroscopy of electron-electron and electron-phonon energy relaxation in ag and au. *Phys. Rev. B*, 51:11433–11445, May 1995. DOI: 10.1103/PhysRevB.51.11433. URL http://link.aps.org/doi/10.1103/PhysRevB.51.11433.

Ping Gu, Masahiko Tani, Shunsuke Kono, Kiyomi Sakai, and X.-C. Zhang. Study of terahertz radiation from inas and insb. *Journal of Applied Physics*, year = 2002, volume = 91, number = 9, pages = 5533-5537, url = http://scitation.aip.org/content/aip/journal/jap/91/9/10.1063/1.1465507, doi = http://dx.doi.org/10.1063/1.1465507*.

M Zahid Hasan and Charles L Kane. Colloquium: topological insulators. *Reviews of Modern Physics*, 82(4):3045, 2010.

J. P. Hinton, S. Patankar, E. Thewalt, A. Ruiz, G. Lopez, N. Breznay, A. Vishwanath, J. Analytis, J. Orenstein, J. D. Koralek, and I. Kimchi. Photoexcited states of the harmonic honeycomb iridate $\gamma - li_2iro_3$. *Phys. Rev. B*, 92:115154, Sep 2015. DOI: 10.1103/PhysRevB.92.115154. URL http://link.aps.org/doi/10.1103/PhysRevB.92.115154.

P Hohenberg and W Kohn. Physical review 136. *B864*, 1964.

D. Hsieh, F. Mahmood, D. H. Torchinsky, G. Cao, and N. Gedik. Observation of a metal-to-insulator transition with both mott-hubbard and slater characteristics in sr_2iro_4 from time-resolved photocarrier dynamics. *Phys. Rev. B*, 86:035128, 2012.

John Hubbard. Electron correlations in narrow energy bands. iii. an improved solution. In *Proceedings of the Royal Society of London A: Mathematical, Physical and Engineering Sciences*, volume 281, pages 401–419. The Royal Society, 1964.

Masatoshi Imada, Atsushi Fujimori, and Yoshinori Tokura. Metal-insulator transitions. *Reviews of Modern Physics*, 70(4):1039, 1998.

Motohiko Ishii, Takaho Tanaka, Takashi Akahane, and Nobuo Tsuda. Infrared transmission spectra of metallic reo3. *Journal of the Physical Society of Japan*, 41(3):908–912, 1976.

G. Jackeli and G. Khaliullin. Mott insulators in the strong spin-orbit coupling limit: From heisenberg to a quantum compass and kitaev models. *Phys. Rev. Lett.*, 102:017205, 2009.

IS Jacobs, S Roberts, and PE Lawrence. Antiferromagnetic resonance in cocl2 and fecl2. *Journal of Applied Physics*, 36(3):1197–1198, 1965.

Robert A Kaindl, Marc A Carnahan, Daniel S Chemla, Seongshik Oh, and James N Eckstein. Dynamics of cooper pair formation in bi 2 sr 2 ca cu 2 o 8+ δ. *Physical Review B*, 72(6):060510, 2005.

Jyrki Kauppinen and Jari Partanen. *Frontmatter and Index*. Wiley Online Library.

R. Kersting, K. Unterrainer, G. Strasser, H. F. Kauffmann, and E. Gornik. Few-cycle thz emission from cold plasma oscillations. *Phys. Rev. Lett.*, 79:3038–3041, Oct 1997. DOI: 10.1103/PhysRevLett.79.3038. URL http://link.aps.org/doi/10.1103/PhysRevLett.79.3038.

Jacob B. Khurgin. Optical rectification and terahertz emission in semiconductors excited above the band gap. *J. Opt. Soc. Am. B*, 11(12): 2492–2501, Dec 1994. DOI: 10.1364/JOSAB.11.002492. URL http://josab.osa.org/abstract.cfm?URI=josab-11-12-2492.

N Kida, Y Ikebe, Y Takahashi, JP He, Y Kaneko, Y Yamasaki, R Shimano, T Arima, N Nagaosa, and Y Tokura. Electrically driven spin excitation in the ferroelectric magnet dymno 3. *Physical Review B*, 78 (10):104414, 2008.

N Kida, D Okuyama, S Ishiwata, Y Taguchi, R Shimano, K Iwasa, T Arima, and Y Tokura. Electric-dipole-active magnetic resonance in the conical-spin magnet ba 2 mg 2 fe 12 o 22. *Physical Review B*, 80 (22):220406, 2009.

B. J. Kim, Hosub Jin, S. J. Moon, J.-Y. Kim, B.-G. Park, C. S. Leem, Jaejun Yu, T. W. Noh, C. Kim, S.-J. Oh, J.-H. Park, V. Durairaj, G. Cao, and E. Rotenberg. Novel $J_{\text{eff}} = 1/2$ mott state induced by relativistic spin-orbit coupling in sr_2iro_4. *Phys. Rev. Lett.*, 101: 076402, 2008.

PDC King, T Takayama, Anna Tamai, E Rozbicki, S McKeown Walker, M Shi, L Patthey, RG Moore, D Lu, KM Shen, et al. Spectroscopic indications of polaronic behavior of the strong spin-orbit insulator sr 3 ir 2 o 7. *Physical Review B*, 87(24):241106, 2013.

Alexei Kitaev. Anyons in an exactly solved model and beyond. *Annals of Physics*, 321(1):2–111, 2006.

Charles Kittel. *Introduction to solid state physics*. Wiley, 2005.

Hiromichi Kuriyama, Jobu Matsuno, Seiji Niitaka, Masaya Uchida, Daisuke Hashizume, Aiko Nakao, Kunihisa Sugimoto, Hiroyuki Ohsumi, Masaki Takata, and Hidenori Takagi. Epitaxially stabilized iridium spinel oxide without cations in the tetrahedral site. *arXiv preprint arXiv:1005.2926*, 2010.

Y.S. Lee. *Principles of Terahertz Science and Technology*. Lecture Notes in Physics. Springer US, 2009. ISBN 9780387095400. URL https://books.google.it/books?id=4ZqkuUURxFcC.

Ying Li, Kateryna Foyevtsova, Harald O. Jeschke, and Roser Valentí. Analysis of the optical conductivity for $A_2iro_3 (a = \text{Na}, \text{Li})$ from first principles. *Phys. Rev. B*, 91:161101, Apr 2015. DOI: 10.1103/PhysRevB.91.161101. URL http://link.aps.org/doi/10.1103/PhysRevB.91.161101.

X Liu, T Berlijn, W-G Yin, W Ku, A Tsvelik, Young-June Kim, H Gretarsson, Yogesh Singh, P Gegenwart, and JP Hill. Long-range magnetic ordering in na 2 iro 3. *Physical Review B*, 83(22):220403, 2011.

Masaaki Matsuda, Randy Scott Fishman, Tao Hong, CH Lee, T Ushiyama, Y Yanagisawa, Y Tomioka, and T Ito. Magnetic dispersion and anisotropy in multiferroic bifeo 3. *Physical review letters*, 109 (6):067205, 2012.

I. I. Mazin, Harald O. Jeschke, Kateryna Foyevtsova, Roser Valentí, and D. I. Khomskii. na_2iro_3. *Phys. Rev. Lett.*, 109:197201, 2012.

I. I. Mazin, S. Manni, K. Foyevtsova, Harald O. Jeschke, P. Gegenwart, and Roser Valentí. Origin of the insulating state in honeycomb iridates and rhodates. *Phys. Rev. B*, 88:035115, 2013.

Nevill Mott. On metal-insulator transitions. *Journal of Solid State Chemistry*, 88(1):5–7, 1990.

M Mourigal, WT Fuhrman, AL Chernyshev, and ME Zhitomirsky. Dynamical structure factor of the triangular-lattice antiferromagnet. *Physical Review B*, 88(9):094407, 2013.

Yoshihiko Okamoto, Minoru Nohara, Hiroko Aruga-Katori, and Hidenori Takagi. Spin-liquid state in the s= 1/2 hyperkagome antiferromagnet na 4 ir 3 o 8. *Physical review letters*, 99(13):137207, 2007.

Alan V Oppenheim, Ronald W Schafer, John R Buck, et al. *Discrete-time signal processing*, volume 2. Prentice-hall Englewood Cliffs, 1989.

John P Perdew, JA Chevary, SH Vosko, Koblar A Jackson, Mark R Pederson, DJ Singh, and Carlos Fiolhais. Atoms, molecules, solids, and surfaces: Applications of the generalized gradient approximation for exchange and correlation. *Physical Review B*, 46(11):6671, 1992.

Dmytro Pesin and Leon Balents. Mott physics and band topology in materials with strong spin–orbit interaction. *Nature Physics*, 6(5): 376–381, 2010.

A Pimenov, AA Mukhin, V Yu Ivanov, VD Travkin, AM Balbashov, and A Loidl. Possible evidence for electromagnons in multiferroic manganites. *Nature Physics*, 2(2):97–100, 2006.

A Pimenov, AM Shuvaev, AA Mukhin, and A Loidl. Electromagnons in multiferroic manganites. *Journal of Physics: Condensed Matter*, 20 (43):434209, 2008.

RP Prasankumar, H Okamura, H Imai, Y Shimakawa, Y Kubo, SA Trugman, AJ Taylor, and RD Averitt. Coupled charge-spin dynamics of the magnetoresistive pyrochlore tl 2 mn 2 o 7 probed using ultrafast midinfrared spectroscopy. *Physical review letters*, 95(26): 267404, 2005.

TF Qi, OB Korneta, Xiangang Wan, LE DeLong, P Schlottmann, and G Cao. Strong magnetic instability in correlated metallic bi2ir207. *Journal of Physics: Condensed Matter*, 24(34):345601, 2012.

Xiao-Liang Qi and Shou-Cheng Zhang. Topological insulators and superconductors. *Reviews of Modern Physics*, 83(4):1057, 2011.

AP Ramirez et al. Handbook of magnetic materials. *Ed. KHJ Buschow, Elsevier, Amsterdam*, 13:423, 2001.

Matthew Reid, Igor V. Cravetchi, and Robert Fedosejevs. Terahertz radiation and second-harmonic generation from inas: Bulk versus surface electric-field-induced contributions. *Phys. Rev. B*, 72:035201, Jul 2005. DOI: 10.1103/PhysRevB.72.035201. URL http://link.aps.org/doi/10.1103/PhysRevB.72.035201.

PL Richards. Far-infrared magnetic resonance in cof2, nif2, knif3, and ybig. *Journal of Applied Physics*, 34(4):1237–1238, 1963.

Marcelo Salamon. The physics of manganites: Structure and transport. *Reviews of Modern Physics*, 73(3):583, 2001.

M Schmidt, Zhe Wang, Ch Kant, F Mayr, S Toth, ATMN Islam, B Lake, V Tsurkan, A Loidl, and J Deisenhofer. Exciton-magnon transitions in the frustrated chromium antiferromagnets cucro 2, α-cacr 2 o 4, cdcr 2 o 4, and zncr 2 o 4. *Physical Review B*, 87(22): 224424, 2013.

R. W. Schoenlein, W. Z. Lin, J. G. Fujimoto, and G. L. Eesley. Femtosecond studies of nonequilibrium electronic processes in metals. *Phys. Rev. Lett.*, 58:1680–1683, Apr 1987. DOI: 10.1103/PhysRevLett.58.1680. URL http://link.aps.org/doi/10.1103/PhysRevLett.58.1680.

MD Segall, Philip JD Lindan, MJ al Probert, CJ Pickard, PJ Hasnip, SJ Clark, and MC Payne. First-principles simulation: ideas, illustrations and the castep code. *Journal of Physics: Condensed Matter*, 14(11): 2717, 2002.

AJ Sievers III and M Tinkham. Far infrared antiferromagnetic resonance in mno and nio. *Physical Review*, 129(4):1566, 1963a.

AJ Sievers III and M Tinkham. Far infrared spectra of rare-earth iron garnets. *Physical Review*, 129(5):1995, 1963b.

Singh. Antiferromagnetic mott insulating state in single crystals of the honeycomb lattice material na_2iro_3. *Phys. Rev. B*, 82:064412, Aug 2010. DOI: 10.1103/PhysRevB.82.064412. URL http://link.aps.org/doi/10.1103/PhysRevB.82.064412.

David M Slocum, Elizabeth J Slingerland, Robert H Giles, and Thomas M Goyette. Atmospheric absorption of terahertz radiation and water vapor continuum effects. *Journal of Quantitative Spectroscopy and Radiative Transfer*, 127:49–63, 2013.

C. H. Sohn, H.-S. Kim, T. F. Qi, D. W. Jeong, H. J. Park, H. K. Yoo, H. H. Kim, J.-Y. Kim, T. D. Kang, Deok-Yong Cho, G. Cao, J. Yu, S. J. Moon, and T. W. Noh. Mixing between $J_{\text{eff}} = \frac{1}{2}$ and $\frac{3}{2}$ orbitals in na_2iro_3: A spectroscopic and density functional calculation study. *Phys. Rev. B*, 88:085125, 2013.

Gaibei Song, Junjie Jiang, Xinyan Wang, Zuanming Jin, Xian Lin, Guohong Ma, and Shixun Cao. Selective excitation of spin resonance in orthoferrite prfeo3 with impulsive polarized terahertz radiation. *Journal of Applied Physics*, 114(24):243104, 2013.

Vladimir A. Stoica, Yu-Miin Sheu, David A. Reis, and Roy Clarke. Wideband detection of transient solid-state dynamics using ultrafast fiber lasers and asynchronous optical sampling. *Opt. Express*, 16(4): 2322–2335, Feb 2008. DOI: 10.1364/OE.16.002322. URL http://www.opticsexpress.org/abstract.cfm?URI=oe-16-4-2322.

AB Sushkov, R Valdés Aguilar, S Park, SW Cheong, and HD Drew. Electromagnons in multiferroic ymn 2 o 5 and tbmn 2 o 5. *Physical review letters*, 98(2):027202, 2007.

Masahiko Tani, Yuichi Hirota, ChristopherT. Que, Shigehisa Tanaka, Ryo Hattori, Mariko Yamaguchi, Seizi Nishizawa, and Masanori Hangyo. Novel terahertz photoconductive antennas. *International Journal of Infrared and Millimeter Waves*, 27(4):531–546, 2006. ISSN 0195-9271. DOI: 10.1007/s10762-006-9105-8. URL http://dx.doi.org/10.1007/s10762-006-9105-8.

Tokura. Colossal magnetoresistive manganites. *Journal of magnetism and magnetic materials*, 200(1):1–23, 1999.

Y Tokura and N Nagaosa. Orbital physics in transition-metal oxides. *science*, 288(5465):462–468, 2000.

S. Toth, B. Lake, S. A. J. Kimber, O. Pieper, M. Reehuis, A. T. M. N. Islam, O. Zaharko, C. Ritter, A. H. Hill, H. Ryll, K. Kiefer, D. N. Argyriou, and A. J. Williams. 120° helical magnetic order in the distorted triangular antiferromagnet α-$cacr_2o_4$. *Phys. Rev. B*, 84: 054452, Aug 2011. DOI: 10.1103/PhysRevB.84.054452. URL http://link.aps.org/doi/10.1103/PhysRevB.84.054452.

William Witczak-Krempa, Gang Chen, Yong Baek Kim, and Leon Balents. Correlated quantum phenomena in the strong spin-orbit regime. *arXiv preprint arXiv:1305.2193*, 2013.

Frederick Wooten. *Optical properties of solids*. Academic press, 2013.

Q. Wu and X.-C. Zhang. Free-space electro-optics sampling of mid-infrared pulses. *Applied Physics Letters*, 71(10), 1997.

X Xin, H Altan, A Saint, D Matten, and RR Alfano. Terahertz absorption spectrum of para and ortho water vapors at different humidities at room temperature. *Journal of Applied Physics*, 100(9): 094905, 2006.

Daiki Yanagishima and Yoshiteru Maeno. Metal-nonmetal changeover in pyrochlore iridates. *Journal of the Physical Society of Japan*, 70(10):2880–2883, 2001.

Feng Ye, Songxue Chi, Huibo Cao, Bryan C Chakoumakos, Jaime A Fernandez-Baca, Radu Custelcean, TF Qi, OB Korneta, and Gang Cao. Direct evidence of a zigzag spin-chain structure in the honeycomb lattice: A neutron and x-ray diffraction investigation of single-crystal na 2 iro 3. *Physical Review B*, 85(18):180403, 2012.

Kenji Yonemitsu and Keiichiro Nasu. Theory of photoinduced phase transitions in itinerant electron systems. *Physics Reports*, 465(1):1 – 60, 2008. ISSN 0370-1573. DOI: http://dx.doi.org/10.1016/j.physrep.2008.04.008. URL http://www.sciencedirect.com/science/article/pii/S0370157308001476.

Marie Yoshikiyo, Asuka Namai, Makoto Nakajima, Keita Yamaguchi, Tohru Suemoto, and Shin-ichi Ohkoshi. High-frequency millimeter wave absorption of indium-substituted ε-fe203 spherical nanoparticles. *Journal of Applied Physics*, 115(17):172613, 2014.

Lee Yun-Shik. Principles of terahertz science and technology. *NY: Springer*, 2008.

List of Publications

S. Peli, N. Nembrini, F. Damin, S. Peli, M. Chiari, C. Giannetti, F. Banfi & G. Ferrini. Discrimination of molecular thin films by surface-sensitive time-resolved optical spectroscopy. *Applied Physics letters* **5**, (2015)

F. Cilento, S. Dal Conte, G. Coslovich, S. Peli, N. Nembrini, S. Mor, F. Banfi, G. Ferrini, H. Eisaki, M. K. Chan, C. J. Dorow, M. J. Veit, M. Greven, D. van der Marel, R. Comin, A. Damascelli, L. Rettig, U. Bovensiepen, M. Capone, C. Giannetti & F. Parmigiani. Photo-enhanced antinodal conductivity in the pseudogap state of high-T_C cuprates. *Nature Communications* **5**, (2014)

Acknowledgments

Innanzitutto voglio ringraziare il mio supervisore Claudio per essere sempre stato disponibile a offrirmi il suo prezioso contributo scientifico e metodologico, senza il quale questo lavoro non sarebbe stato possibile. Grazie per l'infinito tempo che mi hai dedicato in laboratorio e per le innumerevoli cose che mi hai insegnato in questi anni. Grazie per le prove delle presentazioni, per le discussioni di articoli scientifici, per l'entusiasmo e la passione che mi hai sempre trasmesso, per gli spiedi, le partite allo stadio, le grigliate e le birre che abbiamo condiviso. Ma, soprattutto, grazie di cuore per la tua infinita pazienza nei miei confronti. Ti sono grato.

La seconda persona che voglio ringraziare é il collega di laboratorio e mio grande amico, Koffy. Il tuo aiuto e il tuo sostegno in ogni occasione sono stati per me indispensabili; facendo un conto spannometrico, ti devo all'incirca 600 birre. Ti ringrazio per tutti i momenti esilaranti e indimenticabili che abbiamo passato davanti al banco ottico e dietro al banco del bar. Ne abbiamo fatte tante, ma ne faremo ancora!

Ringrazio di cuore Francesco e il Prof Gabriele Ferrini per il loro aiuto e i loro saggi consigli. Se ho fatto questa esperienza di dottorato lo devo soprattutto a loro, che sono stati i miei relatori durante la tesi magistrale. Grazie infinite

Ringrazio Adolfo per aver avere accettato il duro compito di essere il mio referee.

Un grazie di cuore a Maria Flora, comunicatrice eccezionale e persona fantastica, che non manca mai di sostenermi e di incoraggiarmi.

Ringrazio tutti i miei amici. In particolare Luca, grande amico fin dall'infanzia (che tra poco toccherá pure a lui cimentarsi con la tesi di dottorato) e Silvia, che con me ha condiviso ansie e gioie in questi 10 anni di universitá ; probabilmente ho ancora io il tuo quaderno degli appunti di stato solido.

Ringrazio, infine, la mia famiglia per non avermi mai fatto mancare il proprio sostegno morale e materiale, senza la quale nulla sarebbe stato possibile.